

ABSTRACT

BOGACKI, KEVIN JOSEPH. Design of a 50 GHz Bandwidth DPSK Compatible Monolithically Integrated Optical Receiver. (Under the direction of Dr. Leda Lunardi.)

The goal of this work is the design, analysis, and simulation of a monolithic optical receiver consisting of two balanced waveguide photodiodes integrated with a differential transimpedance amplifier, based on InP double heterojunction bipolar technology for 50 Gb/s differential phase shift keying (DPSK) applications.

For the InP / InGaAs double-heterojunction bipolar transistor (DHBT), a small signal equivalent model based upon the Gummel-Poon bipolar junction transistor model was used. This model was determined by fitting measured S-parameters from a published 180 nm collector base-metal-overlaid structure (BMOSA) with a 20 μm^2 hexagonal emitter area. In addition, a thermal model was incorporated to estimate the device operating temperatures. The maximum cut off frequency and maximum frequency of oscillation of the model were 289 and 210 GHz, respectively.

For the InGaAs PIN waveguide photodiode (PIN-WGPD), a small signal equivalent model was also developed based upon published data. The model parameters were found by fitting the photodiode gain profile to measured results for a 300 nm thick evanescently waveguide coupled PIN-PD with a 5x20 μm^2 total area. The bandwidth of the photodiode was 70 GHz with a corresponding responsivity value of 0.37 A/W.

With the transistor model, a fully differential 3-stage transimpedance amplifier was designed. The optimized amplifier yielded a gain of 18.8 dB, bandwidth of 50.3 GHz, transimpedance of 50.9 dB- Ω , and input and output reflection of better than -10 dB. Large signal simulations exhibited open eye diagrams at 50 Gb/s with a wide optical dynamic range

of 28.8 dB. DC simulations indicated that all devices operated at a temperature of less than 144°C, while total power dissipation was less than 305 mW.

Finally, the optimization of the fully integrated optical receiver was evaluated. Two integration schemes were investigated – hybrid and monolithically integrated – with the monolithic optical receiver outperforming the hybrid architecture in terms of wider bandwidth and faster performance. The monolithic receiver showed a gain of 14.3 dB and a bandwidth of 50.0 GHz with input and output reflections better than -10 dB, and exhibited open eye diagrams at 50 Gb/s in DPSK format with an optical dynamic range of 29.0 dB. Noise analysis on the monolithic optical receiver yielded an input referred current noise of less than $65 \text{ pA} / \sqrt{\text{Hz}}$ at the 50 GHz bandwidth.

**DESIGN OF A 50 GHZ BANDWIDTH DPSK COMPATIBLE MONOLITHICALLY
INTEGRATED OPTICAL RECEIVER**

by
KEVIN JOSEPH BOGACKI

A thesis submitted to the Graduate Faculty of
North Carolina State University
in partial fulfillment of the
requirements for the Degree of
Master of Science

ELECTRICAL ENGINEERING

Raleigh, North Carolina

2006

APPROVED BY:

Dr. D. W. Barlage

Dr. Kevin Gard

Dr. Leda Lunardi
Chair of Advisory Committee

BIOGRAPHY

Kevin Joseph Bogacki was born on February 24, 1982 in Rochester, NY. He graduated high school from Cathedral Prep in Erie, PA with a 4.0 GPA and the Excellence in English award. He entered Gannon University in 2000 and majored in electrical and computer engineering. During his tenure at Gannon University, he was the Eta Kappa Nu – Iota Nu chapter president, an active IEEE student member, and was recognized as the runner-up for the HKN Norman R. Carson Award for the Outstanding Junior Electrical Engineering Student in the United States of America. He interned fulltime at Verizon Communications with the Network Planning and Engineering group and his senior project was the design of a sensor network for a home security system. In 2004, he graduated *summa cum laude* and received the Academic Excellence Award for Electrical and Computer Engineering and the Archbishop John Mark Gannon Award for General Scholastic Excellence. Kevin then went on to begin research at North Carolina State University in optical communications under Dr. Leda Lunardi. Initially, he was sponsored by the NCSU Dean’s fellowship and the Nortel Networks fellowship, and he worked as an electrical engineering teaching assistant. He then became a research assistant under Dr. Lunardi and received the Lincoln Laboratory fellowship from MIT, where he interned for a summer in the Optical Communications Technology group establishing a 10 Gb/s differential phase shift keying optical communication link. He is currently a candidate for the degree of Masters in electrical engineering at North Carolina State University.

ACKNOWLEDGMENTS

This work would not have been possible if not for the guidance and dedication of the author's advisor, Dr. Leda Lunardi. Dr. Lunardi provided constant inspiration and encouragement throughout the author's master's work. Although Dr. Lunardi had responsibilities outside of North Carolina, her amazing commitment to her students at NCSU brought her back for weekly meetings and allowed her to be only an email or phone call away. The author would also like to thank Dr. Lunardi for believing in his abilities and always pushing him towards academic excellence.

The author also thanks Dr. Douglas Barlage and Dr. Kevin Gard for serving on the advisory committee. Dr. Barlage provided invaluable feedback throughout the author's work on device modeling and noise analysis, while Dr. Gard provided his expertise on circuit design. Furthermore, Dr. Gard's analog circuit design course and Dr. Barlage's microwave engineering course were most beneficial to the author.

Finally, the author would like to thank his family for always being there. Without their love and encouragement, none of this work would have been achievable. The author's parents provided stability and guidance, while his brother and sister provided friendship and support throughout the author's academic career and life journeys. For this, the author dedicates this work to them.

This work was supported by the National Science Foundation.

TABLE OF CONTENTS

	Page
LIST OF TABLES.....	vi
LIST OF FIGURES.....	viii
LIST OF ACRONYMS.....	xii
1. INTRODUCTION.....	1
2. THE OPTICAL COMMUNICATION LINK.....	5
2.1 Fiber Optic Communication Channel.....	5
2.1.1 Propagation in Optical Fiber.....	5
2.1.2 Optical Fiber Loss.....	10
2.1.3 Dispersion.....	12
2.1.4 Nonlinear Effects.....	17
2.1.5 Wave Division Multiplexing.....	17
2.2 A Basic Fiber Optic Communication Link.....	19
2.2.1 Lasers.....	20
2.2.2 External Optical Modulators.....	24
2.2.3 Erbium Doped Fiber Amplifiers.....	27
2.3 Modulation Formats.....	30
2.3.1 On-Off Keying.....	31
2.3.2 Differential Phase Shift Keying.....	32
2.4 The Optical Receiver.....	35
2.4.1 Introduction.....	35
2.4.2 Defining Receiver Performance Parameters.....	38
2.4.3 The Photo Detector.....	43
2.4.3.1 PIN Photodiode.....	43
2.4.3.2 Vertically Illuminated Photodiode.....	46
2.4.3.3 Waveguide Photodiode.....	50
2.4.3.4 Distributed Photodiode and Avalanche Photodiode.....	53
2.4.4 The Front-End Amplifier.....	54
2.4.5 Front-End Amplifier Examples.....	57
2.4.6 Differential Phase Shift Keying Receiver.....	62
3. TRANSIMPEDANCE CIRCUIT DESIGN.....	64
3.1 Design Overview.....	64
3.2 Double Heterojunction Bipolar Transistor Model.....	66
3.3 PIN Photodiode Model.....	75
3.4 Transimpedance Amplifier Topology.....	77
3.5 Differential Transimpedance Amplifier Design.....	80

3.5.1	Design Analysis of the TIA.....	80
3.5.1.1	Choosing Bias Conditions.....	80
3.5.1.2	TIA Design: Stage 1.....	82
3.5.1.3	TIA Design: Stage 2.....	88
3.5.1.4	TIA Design: Stage 3.....	90
3.5.1.5	Current Mirrors.....	90
3.5.1.6	Open Loop Gain.....	92
3.5.2	Optimization of the TIA Parameters.....	93
3.6	Photodiode Integration.....	98
3.6.1	Hybrid Optical Receiver.....	98
3.6.2	Monolithic Optical Receiver.....	101
4.	SIMULATION RESULTS AND ANALYSIS.....	104
4.1	Introduction.....	104
4.2	Transimpedance Amplifier Results.....	105
4.2.1	DC Simulations.....	105
4.2.2	Small Signal Simulations.....	108
4.2.3	Large Signal Simulations.....	110
4.3	Integrated Optical Receiver Results.....	117
4.3.1	DC Simulations.....	118
4.3.2	Small Signal Simulations.....	122
4.3.3	Large Signal Simulations.....	124
5.	NOISE RESULTS AND ANALYSIS.....	133
5.1	Noise Analysis.....	133
5.1.1	Photodiode Noise.....	133
5.1.2	Transistor Noise.....	135
5.1.3	Transimpedance Amplifier Noise.....	138
5.2	Noise Results.....	141
5.2.1	3-dB Noise versus Bandwidth.....	141
5.2.2	3-dB Noise versus bias.....	142
5.2.3	Noise Figure.....	147
6.	CONCLUSIONS AND FUTURE WORK.....	149
7.	LIST OF REFERENCES.....	152
8.	APPENDIX.....	162

LIST OF TABLES

		Page
Table 2.1	Capacities of current technology.....	19
Table 2.2	Experimental receiver sensitivity.....	37
Table 3.1	Optical receiver specification table.....	64
Table 3.2	DHBT layer materials [59].....	66
Table 3.3	DHBT model parameters.....	68
Table 3.4	Thermal conductivities of selected materials [29].....	69
Table 3.5	DHBT self-heating model parameters.....	69
Table 3.6	f_t and f_{max} comparison between simulated model and measured results [59].....	72
Table 3.7	DHBT model parameter listing for new 50 GHz bandwidth appropriate model (see text).....	73
Table 3.8	f_t and f_{max} listing for new 50 GHz bandwidth appropriate model (see text).....	74
Table 3.9	WGPD layer materials.....	75
Table 3.10	WGPD model parameters.....	76
Table 3.11	Optimum DHBT bias conditions.....	82
Table 3.12	TIA parameter variables.....	94
Table 3.13	TIA parameter variables.....	97
Table 3.14	Bond wire and pad parasitic values [54-55].....	100
Table 3.15	Discrete optical receiver parameter variables.....	101
Table 3.16	Monolithic optical receiver parameter variables.....	103
Table 4.1	Optical receiver specification and compliance table.....	104
Table 4.2	TIA Parameter Variables.....	105
Table 4.3	Bias conditions of differential TIA amplifier stages (with single 5V power supply).....	105
Table 4.4	Bias conditions of TIA bias circuit.....	106
Table 4.5	Dissipated power for TIA.....	106
Table 4.6	Dissipated power for TIA bias circuit.....	107
Table 4.7	Temperature operation of DHBTs in TIA.....	108
Table 4.8	Differential TIA high frequency comparison of simulated results to Weiner's measured results [91].....	110
Table 4.9	Large signal simulations for differential TIA as compared to measured TIA published by Weiner [91].....	117
Table 4.10	Optical receiver parameter values.....	117
Table 4.11	Bias conditions of discrete receiver amplifier stages.....	118
Table 4.12	Bias conditions of monolithic receiver amplifier stages.....	118
Table 4.13	Bias conditions of discrete receiver bias circuit.....	119
Table 4.14	Bias conditions of monolithic receiver bias circuit.....	119
Table 4.15	Dissipated power for discrete receiver.....	119
Table 4.16	Dissipated power for monolithic receiver.....	120
Table 4.17	Dissipated power for discrete receiver bias circuit.....	120
Table 4.18	Dissipated power for monolithic receiver bias circuit.....	120

Table 4.19	Temperature operation of DHBTs in discrete receiver.....	122
Table 4.20	Temperature operation of DHBTs in monolithic receiver.....	122
Table 4.21	High frequency comparison of monolithic receiver versus discrete receiver.....	124
Table 4.22	Large signal simulations for monolithically integrated receiver as compared to discrete receiver.....	132
Table 5.1	Monolithic optical receiver parameter values for minimum noise.....	141
Table 5.2	Bias current / Δ bias needed to stay within ± 1 pA / $\sqrt{\text{Hz}}$ of the noise minimum.....	146
Table 5.3	NF results of monolithic optical receiver optimized for different electrical BWs.....	148

LIST OF FIGURES

		Page
Figure 1.1	Optical SNR versus bit-error-rate for DPSK and OOK systems at 40 Gb/s [96].....	1
Figure 1.2	Advanced technologies available for high-speed optical communications [36].....	2
Figure 2.1	Index profile of step-index fiber with core radius r	6
Figure 2.2	Multimode fiber light propagation conditions.....	7
Figure 2.3	Single mode fiber absorption spectrum [33].....	11
Figure 2.4	Dispersion versus wavelength for a standard single mode fiber [40].....	14
Figure 2.5	Chirped optical pulse as a function of time [72].....	15
Figure 2.6	Basic wave division multiplexing (WDM) setup. This system multiplexes n optical channels, each of X Gb/s, to combine for a total rate of nX Gb/s.....	18
Figure 2.7	A basic modern fiber optic communication link consisting of an optical transmitter, amplifier, and receiver.....	19
Figure 2.8	(a) Simple Fabry-Perot laser diagram (b) Multimode spectral characteristics.....	21
Figure 2.9	(a) Distributed Feedback laser (b) Single-mode spectral characteristics.....	22
Figure 2.10	Basic Mach-Zehnder modulator schematic.....	25
Figure 2.11	Cross section, schematic top view, and package view of dual drive lithium niobate MZM [97].....	25
Figure 2.12	Monolithically integrated lumped electrode EAM and DFB laser [86].....	26
Figure 2.13	Three band energy diagram for EDFA.....	28
Figure 2.14	Gain of typical EDFA as function of wavelength and pump power [72].....	29
Figure 2.15	Optical spectra and intensity eye diagrams for various modulation formats [93].....	30
Figure 2.16	Simple RZ-OOK system diagram.....	32
Figure 2.17	Simple RZ-DPSK system diagram.....	34
Figure 2.18	Outline of the optical receiver.....	35
Figure 2.19	Experimental receiver sensitivity.....	38
Figure 2.20	Example eye diagram.....	42
Figure 2.21	Typical 1550 nm photodiode in photoconductive mode [25].....	43
Figure 2.22	Current-voltage characteristic of a p-n junction [32].....	45
Figure 2.23	Vertical illuminated photodiode [38].....	46
Figure 2.24	Plot illustrating tradeoff between thickness and bandwidth. (As the thickness decreases for a particular device, BW increases. However, once the thickness passes the point at which the time constant equals the transient time, BW begins to suffer) [6].....	47

Figure 2.25	Bandwidth versus quantum efficiency tradeoff [6].....	48
Figure 2.26	Double-pass vertical illuminated photodiode [38].....	50
Figure 2.27	Vertical illuminated photodiode (b) Waveguide photodiode [38].....	50
Figure 2.28	Mushroom-mesa waveguide photodiode [38].....	52
Figure 2.29	Bandwidth versus quantum efficiency for the vertically illuminated photodiode and waveguide photodiode [39].....	52
Figure 2.30	(a) Simple high-impedance front-end amplifier (b) Simple transimpedance front-end amplifier [72].....	54
Figure 2.31	Advanced technologies available for high optical communication bit rates [85].....	56
Figure 2.32	Amplifier #1.....	57
Figure 2.33	Amplifier #2.....	58
Figure 2.34	Amplifier #3 (a) SiGe implementation (b) InP Implementation.....	59
Figure 2.35	Amplifier #4 (a) HBT implementation (b) HFET implementation.....	60
Figure 2.36	Amplifier #5.....	60
Figure 2.37	Amplifier #6.....	61
Figure 2.38	Detailed block diagram of DPSK optical receiver.....	62
Figure 2.39	Discrete DPSK optical receiver and block outline [81].....	63
Figure 2.40	Monolithic DPSK optical receiver overview [37].....	63
Figure 3.1	DPSK receiver block diagram.....	65
Figure 3.2	DHBT device cross section [59].....	66
Figure 3.3	DHBT model topologies (a) large signal (b) small signal [109].....	67
Figure 3.4	DHBT self-heating model [109].....	68
Figure 3.5	DHBT device I-V curves with temperature profile.....	70
Figure 3.6	S-parameter comparison. Measured data taken from [59].....	71
Figure 3.7	S ₂₁ comparison. Measured results taken from [59].....	71
Figure 3.8	f_t and f_{max} of DHBT model. Measured results taken from ($V_{CE} = 1.2$ V) [59].....	72
Figure 3.9	S-parameter comparison for adjusted model. Measured results taken from [59].....	74
Figure 3.10	WGPD device cross section.....	75
Figure 3.11	WGPD small signal model topology [60].....	76
Figure 3.12	S-parameter comparison. Measured results taken from [88].....	77
Figure 3.13	Differential transimpedance amplifier topology.....	78
Figure 3.14	f_t / f_{max} curves illustrating proper bias points (note that these curves are the same curves presented Figure 3.8, meaning this is for the original model, not the adjusted model. Adjusted model Kirk effect values are given in above text. $V_{CE} = 1.2$ V).....	80
Figure 3.15	DHBT adjusted model I-V curves with temperature profile.....	81
Figure 3.16	Emitter-coupled differential input pair with adjusted DHBT model.....	83
Figure 3.17	Emitter-coupled differential input pair with adjusted DHBT model simulations.....	85
Figure 3.18	Emitter-coupled differential input pair with adjusted DHBT model simulations.....	86
Figure 3.19	Emitter follower with adjusted DHBT model.....	88
Figure 3.20	Current mirrors used to bias TIA.....	91

Figure 3.21	Open loop block diagram for 3 stage TIA with single power supply.....	93
Figure 3.22	Block diagram of three stage transimpedance design with single power supply.....	93
Figure 3.23	Gain versus bandwidth of the transimpedance amplifier.....	95
Figure 3.24	Gain / bandwidth versus feedback resistance.....	96
Figure 3.25	S21 for various feedback resistances (50, 75, 100, 125 Ω).....	97
Figure 3.26	Discrete optical receiver with balanced photodiodes and differential TIA.....	99
Figure 3.27	Parasitics model of bond wire and pad capacitance for the discrete receiver.....	100
Figure 3.28	Monolithic optical receiver with balanced photodiodes and differential TIA.....	102
Figure 4.1	Dissipated power breakdown for differential TIA.....	107
Figure 4.2	S-parameters from (a) simulated InP design and (b) measured InP results found in “SiGe Differential Transimpedance Amplifier with 50-GHz Bandwidth” by Weiner [91].....	109
Figure 4.3	Transient analysis input to differential TIA.....	111
Figure 4.4	TIA transient input current and output voltage.....	112
Figure 4.5	Differential output eye diagram driven with input current of 500 μA	113
Figure 4.6	Differential output eye diagram driven with various 50 GHz PRBS amplitudes.....	114
Figure 4.7	Differential output eye amplitude versus photocurrent.....	116
Figure 4.8	Measured InP TIA results [91].....	116
Figure 4.9	Dissipated power breakdown for optical receivers.....	121
Figure 4.10	S-Parameters from (a) discrete receiver design (b) monolithic receiver design: Supply voltage = 5V.....	123
Figure 4.11	Transient analysis input for discrete integrated receiver.....	125
Figure 4.12	Transient analysis input for monolithically integrated receiver.....	126
Figure 4.13	Discrete receiver transient input and output voltage at 50 GHz.....	127
Figure 4.14	Monolithic receiver transient input and output voltage at 50 GHz.....	127
Figure 4.15	Differential output eye diagrams driven with various 50 GHz PRBS amplitudes.....	129
Figure 4.16	Differential output eye amplitude versus photocurrent.....	131
Figure 4.17	Differential output eye diagram of monolithic receiver when driven with optical input voltage of 50 mV.....	131
Figure 5.1	Photodiode small signal model with included noise sources.....	134
Figure 5.2	HBT small signal model with included noise sources.....	136
Figure 5.3	Noise versus frequency for a single HBT. $V_{CE} = 1.2 \text{ V}$, $I_C = 13 \text{ mA}$	138
Figure 5.4	Input referred noise versus feedback resistance. $V_{bias} = 5\text{V}$	139
Figure 5.5	Minimum input referred noise versus electrical bandwidth for the monolithic optical receiver.....	142
Figure 5.6	Input referred noise versus bias current.....	143
Figure 5.7	Input referred noise versus frequency for 50 GHz monolithic optical receiver design (Schematic in Figure 3.27, Parameters in Table 3.16).....	146

Figure 5.8	Noise figure versus frequency for 50 GHz monolithic optical receiver design (Schematic in Figure 3.27, Parameters in Table 3.16).....	147
Figure 5.9	NF versus electrical bandwidth for the monolithic optical receiver.....	148
Figure A.1	Adjusted DHBT model.....	163

LIST OF ACRONYMS

Acronym	Expansion
ADS	Advanced Design System
AMI	Alternate-mark Inversion
ASE	Amplified Spontaneous Emission
APD	Avalanche Photodiode
BER	Bit-error-rate
BMOSA	Base-metal-overlaid Structure
BW	Bandwidth
C	Chirped
C-Band	Conventional Band
CCCS	Current Controlled Current Source
CMRR	Common Mode Rejection Ratio
CS	Carrier-suppressed
DB	Duobinary
DBR	Distributed Bragg Reflector Laser
DCF	Dispersion Compensated Fiber
DFB	Distributed Feedback Laser
DHBT	Double Heterojunction Bipolar Transistor
DI	Delay Interferometer
DPQSK	Differential Quadrature Phase Shift Keying
DPSK	Differential Phase Shift Keying
EAM	Electro-Absorption Modulator
EDFA	Erbium Doped Fiber Amplifier
ETDM	Electronic Time-Division Demultiplexing
FET	Field Effect Transistor
FWHM	Full Width at Half Maximum
FWM	Four-wave mixing
HBT	Heterojunction Bipolar Transistor
HEMT	High Electron Mobility Transistor
HFET	Heterojunction Field Effect Transistor
IR	Infrared
ISI	Inter-symbol Interference
L-Band	Long Band
MZM	Mach-Zehnder Modulator
NF	Noise Figure
NRZ	Nonretrun-to-zero
NZ-DSF	Non-zero Dispersion Shifted Fiber
OEIC	Optoelectronic Integrated Circuit
OOK	On-off-keying
PIN-PD	PIN Photodiode
PMD	Polarization Mode Dispersion
PMF	Polarization Maintaining Fiber
PRBS	Pseudo-random Bit Sequence

Q Factor	Quality Factor
RZ	Return-to-zero
SBS	Stimulated Brillouin Scattering
SG-DBR	Sampled-grating Distributed Bragg Reflector Laser
SHBT	Single Heterojunction Bipolar Transistor
SMF	Single-mode Fiber
SNR	Signal to Noise Ratio
SOA	Semiconductor Optical Amplifier
S-Parameters	Scattering Parameters
SPM	Self-phase Modulation
SRS	Stimulated Raman Scattering
TIR	Total Internal Reflection
TWA	Traveling Wave Amplifier
TZ	Transimpedance
UTC-PD	Unitravelling-carrier Photodiode
UV	Ultraviolet
VIPD	Vertically Illuminated Photodiode
VSB	Vestigial Sideband
WDM	Wave Division Multiplexing
WGPD	Waveguide Photodiode
XPM	Cross-phase Modulation

1. INTRODUCTION

Fiber optic communication systems became the preferred means for high-speed data transmission because of the achievable wide bandwidth and low loss in the optical fiber. It is estimated that 50 THz bandwidth is available in fiber with a corresponding loss of less than 0.16 dB/km [19, 72, 94]. Implementation of wave division multiplexing systems has increased transmission lengths and capacity limits but also requires alternative modulation formats other than the conventional on-off keying type to circumvent the fiber nonlinearity penalties. Differential phase shift keying (DPSK) modulation has recently been investigated as a viable alternative to increase sensitivity, offering a 3-dB sensitivity advantage over on-off keying and other modulation types. This translates into extended transmission distances and lower optical power requirements for legacy systems [4, 24, 96].

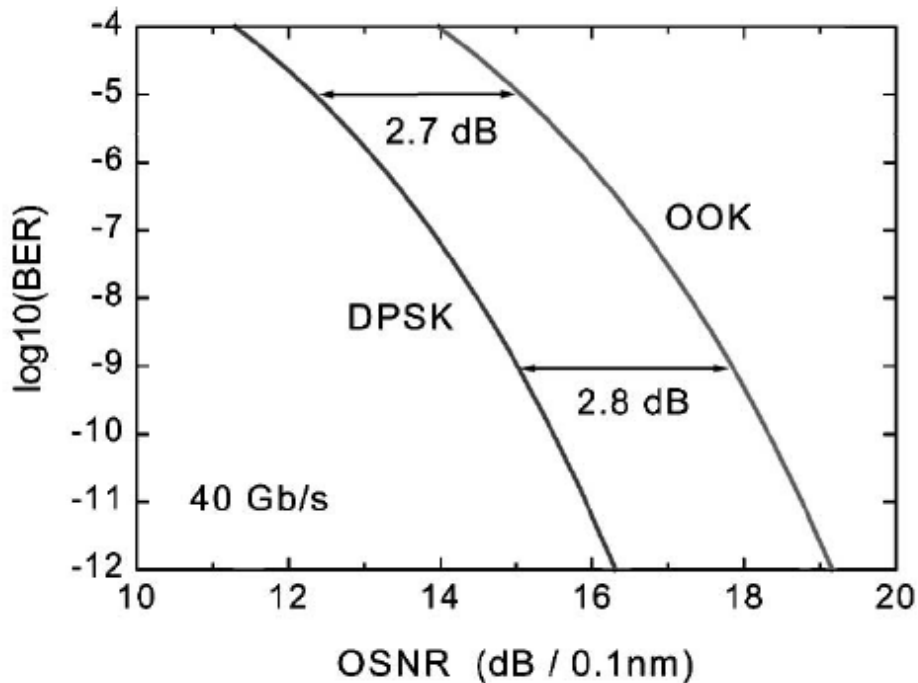


Figure 1.1: Optical SNR versus bit-error-rate for DPSK and OOK systems at 40 Gb/s [96]

However, the implementation of DPSK optical systems is not straightforward since the optical receiver has different requirements than the on-off keying detector. This work considers performance improvements for a high-speed DPSK optical communication link by the integration of the photo detector and a differential transimpedance amplifier. Specifically, the goal is to design, analyze, and simulate a 1.55 μm monolithic optical receiver consisting of two balanced waveguide photodiodes (WGPDs) integrated with a differential transimpedance amplifier to operate at 50 Gb/s in a DPSK system. InP / InGaAs double heterojunction bipolar transistors (DHBTs) were chosen as the technology for the design because they are compatible with the wavelength of operation and the material of the detectors. Furthermore, HBTs have proven to outperform field effect transistors in monolithically integrated photo receivers [52].

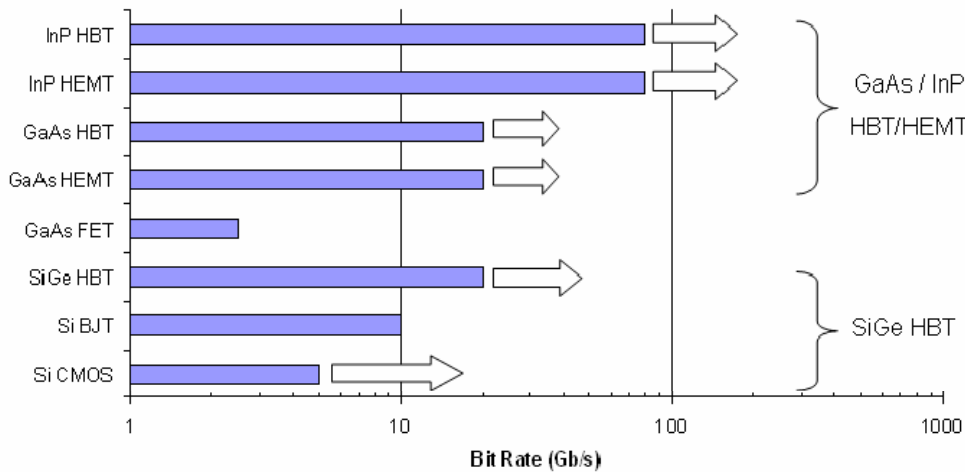


Figure 1.2: Advanced technologies available for high-speed optical communications [36]

The major motivating factor of this thesis is to determine the performance of a monolithic optical receiver in an optical system as compared to a hybrid receiver for DPSK applications. The elimination of the parasitic bond wires connecting the photo detector to the preamplifier in a hybrid detector may allow for increased performance in a monolithic

receiver [45, 76, 84, 96]. Furthermore, the implementation of a monolithic receiver could allow for decision logic circuitry to directly follow the receiver without the use of a post amplifier. In addition to the challenges of designing a high-speed, wide-bandwidth, low-noise monolithically integrated receiver, another goal is to directly compare the monolithic and the hybrid receivers.

Chapter 2 of this thesis provides an introduction to the optical communication link. The physics of a fiber channel is presented including propagation, loss, dispersion, and nonlinearities. The components of a basic fiber optic link are discussed in detail along with a comparison of different modulation techniques, specifically on-off keying and differential phase shift keying. Finally, the background necessary to study the optical receiver is provided including performance parameter definitions and an introduction into the operation of the photo detector and front-end amplifier.

Chapter 3 discusses the design of the integrated optical receiver and presents the receiver specifications used for this work. The initial sections establish the double heterojunction bipolar transistor (DHBT) and waveguide PIN photodiode models used in the simulations. Once the models are determined, a step by step approach is illustrated for the design of the transimpedance amplifier. The final section provides the optimization of the fully integrated optical receiver according to the specifications. Two integration schemes are investigated: the hybrid receiver and the monolithically integrated receiver.

Chapter 4 provides the simulation results for the designed transimpedance amplifier and integrated optical receivers. DC simulations were performed to determine bias conditions, power dissipation, and temperature operation, while small signal simulations were performed to determine gain and bandwidth. Large signal simulations were performed

to investigate transient responses and eye diagrams. Transimpedance amplifier simulations are compared to published results when available, while for the monolithic receiver, the results are analyzed against the hybrid ones.

Chapter 5 is reserved for the noise analysis and results of the monolithically integrated optical receiver. The noise analysis is divided into three sections: photodiode noise, transistor noise, and transimpedance amplifier noise. The noise tradeoffs are also discussed in terms of circuit analysis.

2. THE OPTICAL COMMUNICATION LINK

2.1 Fiber Optic Communication Channel

Optical communication systems are realistically limited by the fiber's refractive index dependence on wavelength and intensity of the transmitted light. For higher bit rates and longer distances, dispersion, or the broadening of the optical pulse, can cause inter-symbol interference (ISI) degrading the performance of the system [72]. In this chapter, an introduction into the fiber optical channel will be provided followed by a discussion on the components of a basic optical communication link and possible modulation formats for that link. Finally, this chapter investigates the details of an optical receiver.

2.1.1 Propagation in Optical Fiber

The optical fiber used in optical communications consists of a silica core surrounded by a silica cladding. The core is usually doped with germanium or phosphorus to increase its index of refraction, while the cladding is doped with boron or fluorine to decrease its index of refraction. This difference in index allows for light to propagate down the length of the fiber. The index change can be gradual (graded index fiber) or abrupt (step index fiber). Graded index fiber is used in multimode transmission to decrease modal dispersion, while the step index fiber is predominately used in single mode transmission [110]. A multimode fiber has a core radius larger than the wavelength of operation (tens of microns), while the single mode fiber has a core radius on the order of the wavelength (a few microns) [75]. To provide a general understand of light propagation in a fiber, the geometry of a multimode step-index fiber can be studied [41].

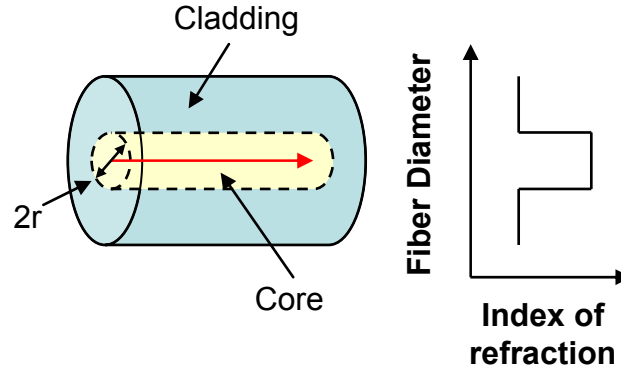


Figure 2.1: Index profile of step-index fiber with core radius r [110]

Light propagation can be understood by assuming the multimode configuration where the radius of the core, r , is more than ten times larger than the wavelength of operation. Here, the rays of light propagate along the length of the fiber by way of reflection at the core / cladding boundary. At any material boundary, Snell's law can be applied.

$$n_1 \sin \theta_1 = n_2 \sin \theta_2 \quad (2.1)$$

where n_1 and n_2 are the indices of the core and cladding respectively, and θ_1 and θ_2 are the angles of incidence and refraction respectively (as measured in reference to the normal). For angles larger than a critical angle, given by:

$$\theta_c = \sin^{-1} \frac{n_2}{n_1}, \quad (2.2)$$

there exists no refracted light and all the light is reflected. This condition is known as total internal reflection (TIR). Geometrically speaking, light will only propagate through the fiber if it meets the TIR condition at the core and cladding interface. If the angle of incidence is less than the critical angle, the light will not propagate through the fiber [72].

In addition to the TIR condition, a condition also exists for the coupling of light into the fiber. Light is only coupled into a fiber if the incident angle is less than θ_{0max} . θ_{0max} can be determined with the following equation.

$$\theta_{0\max} = \sin^{-1} \frac{\sqrt{n_1^2 - n_2^2}}{n_0} \quad (2.3)$$

where n_0 is the index of the air outside of the fiber. Light satisfying this condition will also meet the TIR condition inside the fiber, allowing propagating through the fiber [72].

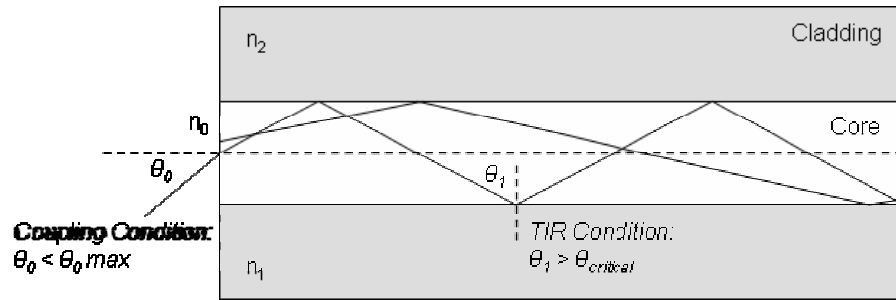


Figure 2.2: Multimode fiber light propagation conditions

As there are many possible angles that fulfill these propagation criteria in a multimode fiber, many modes can be transmitted through the fiber. This directly leads to modal dispersion. Because each mode travels through different reflection angles, the path lengths of each mode are unequal as illustrated in Figure 2.2. This causes the optical pulse to spread out as different modes reach the end of the fiber at different times. Pulse spreading, or dispersion, directly and negatively impacts the performance of an optical system [72].

One way to eliminate modal dispersion is to implement single-mode fiber (SMF), where the core radius is on the order of the operating wavelength allowing only one mode to propagate. Under this assumption, TIR can no longer describe the propagation of light in the fiber. The propagation of light in the SMF is best explained by way of Maxwell's equations because light propagates as if in a diffraction medium [72].

Maxwell's equations are listed below:

$$\nabla \cdot \mathbf{D} = \rho \quad (2.4)$$

$$\nabla \cdot \mathbf{B} = 0 \quad (2.5)$$

$$\nabla \times \mathbf{E} = -\frac{\partial \mathbf{B}}{\partial t} \quad (2.6)$$

$$\nabla \times \mathbf{H} = \mathbf{J} + \frac{\partial \mathbf{D}}{\partial t} \quad (2.7)$$

where \mathbf{D} is the electric density, \mathbf{B} is the magnetic flux density, \mathbf{E} is the electric field, \mathbf{H} is the magnetic field, ρ is the charge density, and \mathbf{J} is the current density. If there is no free charge and no loss, as is often assumed for silica, $\rho = \mathbf{J} = 0$. Also for the silica medium,

$$\mathbf{D} = \varepsilon_o \mathbf{E} + \mathbf{P} \quad (2.8)$$

$$\mathbf{B} = \mu_o \mathbf{H} \quad (2.9)$$

where \mathbf{P} is the electric polarization of light in the fiber. To find the wave equation for the electric field, the curl of equation 2.6 is taken.

$$\nabla \times (\nabla \times \mathbf{E}) = -\mu_o \varepsilon_o \frac{\partial^2 \mathbf{E}}{\partial t^2} - \mu_o \frac{\partial^2 \mathbf{P}}{\partial t^2} \quad (2.10)$$

If a linear-isotropic medium is assumed, the electric polarization is defined by the following with \mathbf{r} and t being the position and time of the vector, respectively.

$$\mathbf{P}(\mathbf{r}, t) = \varepsilon_o \int_{-\infty}^t \chi(\mathbf{r}, t - t') \mathbf{E}(\mathbf{r}, t') dt' \quad (2.11)$$

χ is the linear susceptibility which is a property of the silica fiber. Using the properties of the Fourier transform, \mathbf{E} is described as:

$$\mathbf{E}(\mathbf{r}, t) = \frac{1}{2\pi} \int_{-\infty}^{\infty} \mathbf{E}(\mathbf{r}, \omega) \exp(-i\omega t) d\omega \quad (2.12)$$

The Fourier transforms of $\frac{\partial \mathbf{E}}{\partial t}$ and $\frac{\partial^2 \mathbf{E}}{\partial t^2}$ can be found by taking partial derivatives of the

above equation with respect to time yielding:

$$\frac{\partial \mathbf{E}(\mathbf{r}, t)}{\partial t} = \frac{\partial}{\partial t} \left[\frac{1}{2\pi} \int_{-\infty}^{\infty} \tilde{\mathbf{E}}(\mathbf{r}, \omega) \exp(-i\omega t) d\omega \right] \quad (2.13)$$

The partial derivative leads to Fourier transforms of $\frac{\partial \mathbf{E}}{\partial t}$ and $\frac{\partial^2 \mathbf{E}}{\partial t^2}$ given as $-i\omega\tilde{\mathbf{E}}$ and $\omega^2\tilde{\mathbf{E}}$, respectively. This allows for the Fourier transform of $\nabla \times (\nabla \times \mathbf{E})$.

$$\nabla \times \nabla \times \tilde{\mathbf{E}} = \mu_o \epsilon_o \omega^2 \tilde{\mathbf{E}} + \mu_o \omega^2 \tilde{\mathbf{P}} \quad (2.14)$$

But, the Fourier transform of the electric polarization is given as:

$$\tilde{\mathbf{P}}(\mathbf{r}, \omega) = \epsilon_o \tilde{\chi}(\mathbf{r}, \omega) \tilde{\mathbf{E}}(\mathbf{r}, \omega) \quad (2.15)$$

Therefore,

$$\nabla \times \nabla \times \tilde{\mathbf{E}} = \mu_o \epsilon_o \omega^2 \tilde{\mathbf{E}} + \mu_o \epsilon_o \omega^2 \tilde{\chi} \tilde{\mathbf{E}} \quad (2.16)$$

It is also noted that neglecting losses, the index of refraction can be found by $n(\omega) = \sqrt{1 + \tilde{\chi}(\omega)}$. This further simplifies the $\nabla \times (\nabla \times \mathbf{E})$ equation to

$$\nabla \times \nabla \times \tilde{\mathbf{E}} = \frac{\omega^2 n^2}{c^2} \tilde{\mathbf{E}} \quad (2.17)$$

Using an identity for $\nabla \times (\nabla \times \mathbf{E})$, the equation is altered to the following form.

$$\nabla^2 \tilde{\mathbf{E}} + \frac{\omega^2 n^2}{c^2} \tilde{\mathbf{E}} = \nabla(\nabla \cdot \tilde{\mathbf{E}}) \quad (2.18)$$

Using $\nabla \cdot \mathbf{D} = 0$ and $\mathbf{D} = \epsilon_o \mathbf{E} + \mathbf{P}$, it can be shown that $\nabla(\nabla \cdot \tilde{\mathbf{E}}) = 0$. Therefore, this equation simplifies to the electric field wave equation. The wave equation for the magnetic field can be found in the same manner. Both wave equations are listed [72].

$$\nabla^2 \tilde{\mathbf{E}} + \frac{\omega^2 n^2}{c^2} \tilde{\mathbf{E}} = 0 \quad (2.19)$$

$$\nabla^2 \tilde{\mathbf{H}} + \frac{\omega^2 n^2}{c^2} \tilde{\mathbf{H}} = 0 \quad (2.20)$$

For a single propagation mode in a fiber, there exist two degenerate solutions to Maxwell's wave equations that meet core-cladding boundary conditions. This gives way

to the two transverse fields found within the single mode – the electric field and the magnetic field. The fields are degenerate in that they have the same propagation constant in SMF, meaning they have the same velocity in the fiber. How these two fields are oriented to each other defines the state of polarization of the light in the fiber. If the two fields are in phase, the mode is said to be linearly polarized. If the two fields have perpendicular phase, the mode is said to be orthogonally polarized. Other polarization types include circular and elliptical polarization [72].

If there are several solutions to Maxwell's equations, many modes can propagate along the length of the fiber. Different wavelengths have different velocities, and each mode will arrive at the end of the fiber at different times. This leads to pulse spreading, or dispersion at the end of the fiber. Therefore, Maxwell's equations again prove that single mode fiber is effective in eliminating modal dispersion [72].

2.1.2 Optical Fiber Loss

Fiber optic communication systems benefit significantly from the low loss value of silica fiber [72]. The main contributions of loss are Rayleigh scattering, infrared (IR) absorption, ultraviolet (UV) absorption, and waveguide imperfections. The first two, Rayleigh scattering and IR absorption, outweigh the others. In addition to these contributions, an absorption peak is created during the manufacturing process as water is incorporated into the fiber. All of these contributors are a function of the fiber materials (silica, dopants, etc.) and drawing conditions (temperature, tension, speed, etc) [65].

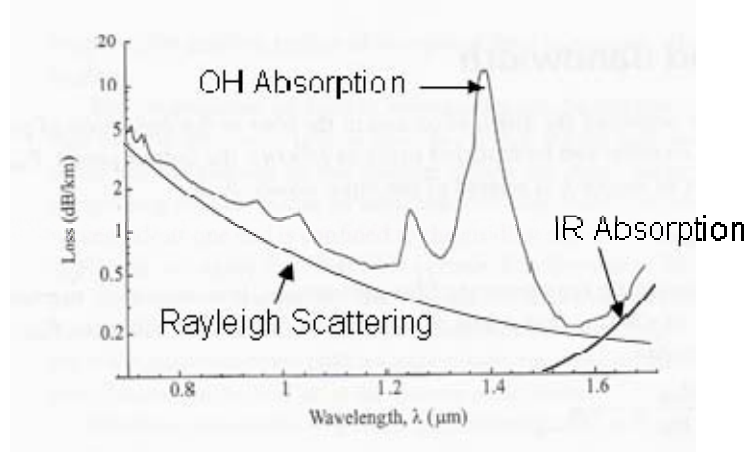


Figure 2.3: Single mode fiber absorption spectrum [33]

Figure 2.3 depicts the experimental loss spectrum including the limits due to Rayleigh scattering and IR absorption for a typical single mode fiber [33]. Shorter wavelength operation is limited by Rayleigh scattering, while longer wavelength operation is limited by IR absorption. The large peak on the experimental curve is due to OH absorption. Three operating wavelengths have been used in the past for fiber communication links – 0.8 μm , 1.3 μm , and 1.55 μm – as each exists at an attenuation minimum. As more light sources became available with the advancement of epitaxial technologies, 1.55 μm predominately became the wavelength of choice, as 1.55 μm exhibits the lowest loss. More recent technologies such as the erbium doped fiber amplifier (EDFA) also influence the need for 1.55 μm operation, as this wavelength is within the EDFA gain spectrum of 1525-1570 nm [72]. EDFAs will be further discussed in section 2.2.3.

The total attenuation in the fiber system can be modeled by:

$$P_{out} = P_{in} \exp(-\alpha_T L) \quad (2.21)$$

Here, P_{in} and P_{out} are the input and output powers of a fiber of length L and attenuation α_T [72]. The total attenuation, α_T , is given by the following:

$$\alpha_T = \alpha_R + \alpha_{IR} \quad (2.22)$$

where α_R and α_{IR} are the Rayleigh scattering and IR absorption losses respectively. Rayleigh scattering loss is proportional to the intensity of light propagating in the fiber while infrared loss is completely dependent upon the materials used to manufacture the fiber.

$$\alpha_R = \frac{1}{\lambda^4} \frac{\int A(r)P(r)rdr}{\int P(r)rdr} \quad (2.23)$$

$$\alpha_{IR} = C \exp\left(-\frac{D}{\lambda}\right) \quad (2.24)$$

where $P(r)$ is the light intensity, $A(r)$ is the Rayleigh scattering coefficient, r is the radial distance, and C and D are material dependent coefficients [65]. These two factors were approximated versus wavelength in Figure 2.3. Although these equations allow for the modeling of the loss parameters of silica, they do not account for the large peaks of water absorption found in the experimental results of SMF.

New advances in manufacturing have led to the development of a new low water peak SMF. This fiber is manufactured by a process that decreases the amount of OH contamination in the fiber, thus eliminating the OH absorption peaks on the attenuation curve. Amazingly, this can theoretically extend the bandwidth of fiber to over 70 THz [31].

2.1.3 Dispersion

In addition to loss, dispersion limits optical system performance at high bit rates. Dispersion can be simply defined as the broadening of an optical pulse in the time domain. It can be detrimental to system performance by inducing ISI, where adjacent bits begin to overlap [73]. Three types of dispersion include modal, chromatic, and polarization mode dispersion (PMD). In the standard single mode fiber, chromatic dispersion and PMD limit

system performance. However, various compensation techniques are available to ameliorate the effects of chromatic dispersion and PMD in the single mode fiber [72].

Chromatic dispersion can be broken up into two types – material dispersion and waveguide dispersion. Although material dispersion accounts for most chromatic dispersion, it is still important to recognize waveguide dispersion. Material dispersion stems from the fact that the index of refraction in the silica fiber depends on the wavelength of the propagating light. Because light sources or transmitters (lasers, see section 2.2.1) have a finite optical spectrum, the different wavelengths within this spectrum will travel at different speeds, resulting in a broadened pulse at the output of the optical fiber. In standard SMF, almost no dispersion exists at 1330 nm wavelength, while at 1550 nm larger dispersion occurs [72].

Waveguide dispersion is the second form of chromatic dispersion. In a typical fiber, some light propagates in the cladding while moving along the fiber. Depending on the particular wavelength of the laser's finite spectrum, either more or less light will enter the cladding. Light moving through the cladding travels at a different speed than the light in the core causing broadening of the pulse at the end of the fiber to occur.

The total chromatic dispersion in a fiber is the sum of the waveguide dispersion and the material dispersion [72]. Figure 2.4 is a plot of dispersion [ps / (nm km)] versus wavelength. For standard SMF, the total chromatic dispersion is low for the 1330 nm wavelength (≈ 0 ps / (nm km)) but high for the 1550 nm wavelength (≈ 17 ps / (nm km)) [40].

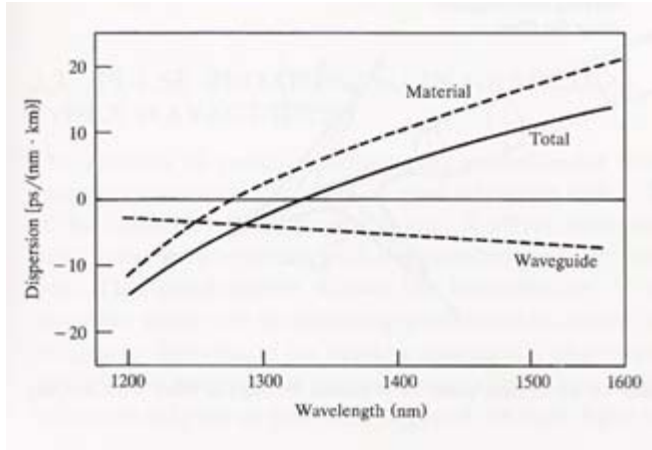


Figure 2.4: Dispersion versus wavelength for a standard single mode fiber [40]

An expression for dispersion can be mathematically determined by understanding the equation for an optical wave traveling in a fiber.

$$|\tilde{E}(z, t)| = J(x, y) \cos(\beta(\omega)z - \omega t - \phi) \quad (2.25)$$

Here z is in the direction of propagation, $J(x, y)$ is the electric field distribution along the x and y axis, and β , the propagation constant, is a function of ω given in the below Taylor series expansion.

$$\beta(\omega) = \beta_0 + \beta_1(\omega - \omega_0) + \frac{1}{2}\beta_2(\omega - \omega_0)^2 + \frac{1}{6}\beta_3(\omega - \omega_0)^3 + \dots \quad (2.26)$$

ω_0 is the center frequency, $\frac{\omega_0}{\beta_0}$ is the phase velocity, and $\frac{1}{\beta_1}$ is the envelope or group velocity. β_2 is the group velocity dispersion parameter (measured in ps^2/km) and is dependent on the wavelength of light. It is responsible for the optical pulse broadening. One can obtain an expression for the dispersion, D , from the group velocity.

$$D = -\frac{2\pi}{\lambda^2} \beta_2 \quad (2.27)$$

The above dispersion equation accounts for both material and waveguide dispersion and has units of ps / (nm km) [41].

The group velocity can also induce chirp in an optical pulse. Chirp, defined as a frequency change across an optical pulse, is depicted below in Figure 2.5. Optical chirp induced by a length of optical fiber is an unwanted effect since broadening any pulse can cause ISI in a system.

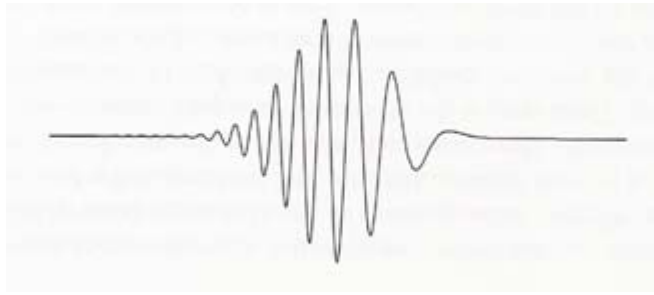


Figure 2.5: Chirped optical pulse as a function of time [72]

Equation 2.28 relates the chirp parameter to the width of the optical pulse. Here, T_z is the output width of the pulse as compared to the input width, T_0 , after traveling a length of z in fiber. κ is the chirp factor of a pulse and is proportional to the rate of change of the frequency with time [72]. As this equation shows, the faster the frequency of the pulse changes with time, the wider the output pulse becomes.

$$\frac{T_z}{T_0} = \sqrt{\left(1 + \frac{\kappa\beta_2 z}{T_0^2}\right)^2 + \left(\frac{\beta_2 z}{T_0^2}\right)^2} \quad (2.28)$$

It should be noted that sometimes adding chirp can improve the performance of a system. Prechirped optical pulses can be used to compensate for chirping induced on a length of optical fiber [69].

Although chromatic dispersion and optical chirp can dramatically limit the performance of an optical system, in the recent years several compensation techniques have

been explored. Electrical dispersion compensation can be implemented at either at the transmitter or receiver side of the link but is limited by the phase control at the transmitter and phase detection at the receiver. Optical dispersion compensation can be implemented anywhere in the link and has the added benefit of feedback control. Common optical dispersion compensation techniques include the use of non-zero dispersion shifted fibers (NZ-DSF) [102], dispersion compensated fiber (DCF) [102], chirped fiber Bragg gratings [68-69], virtually imaged phased arrays [48], etalons [62], ring resonators [53], Mach-Zehnder-interferometers [90], and waveguide grating router-based compensation [57].

The third and final type of dispersion is polarization mode dispersion. Because of the elliptical shape of the optical fiber, different polarizations of light travel at different speeds, which causes broadening of the optical pulse. First order PMD is known as birefringence. In the case of a birefringent fiber, light polarized on one axis is delayed compared to the light polarized on its perpendicular axis. Birefringence randomly changes with the light's position and wavelength, as well as the temperature and stress of the fiber itself. PMD can be measured in terms of $\text{ps}/\sqrt{\text{km}}$ and is on the order of $0.1 \text{ ps}/\sqrt{\text{km}}$ in standard SMF [8].

Because chromatic dispersion compensation is part of the design for any optical system, PMD became the limiting factor in legacy optical systems [72]. However, PMD compensation also exists. PMD compensation depends on the modulation format, the transmitter, and the receiver of the system and can be accomplished electrically or optically. Electrical compensation includes feed-forward and decision feedback equalizers, while optical compensation includes methods using polarization controllers and polarization maintaining fiber (PMF) [8].

2.1.4 Nonlinear Effects

The final limiting factor of the high-speed optical communication system is the nonlinear effect of the optical fiber. Nonlinearities occur when light at one or more wavelengths mix to create light at one or more new wavelengths. The major types of nonlinearities include the χ^3 nonlinearities – self-phase modulation (SPM), cross-phase modulation (XPM), and four-wave mixing (FWM) – and the scattering nonlinearities – stimulated Raman scattering (SRS) and stimulated Brillouin scattering (SBS). This subject has been intensively explored [1, 7], and is above the scope of the present thesis.

2.1.5 Wave Division Multiplexing

Wave division multiplexing (WDM) was envisioned to increase bandwidth (BW) on existing fiber infrastructure by transmitting multiple signals on one fiber allowing for faster transmission than transmitting single signals on multiple fibers. When using WDM to increase bandwidth, the fiber is transformed into multiple ‘virtual fibers’ by transmitting data on different wavelengths of light down a path of SMF. Commercial WDM systems operate with 50 GHz channel spacing at 40 Gb/s per channel [106]. The wavelength spectrum of operation (or number of channels) is usually limited by the spectrum of the optical amplifier as will be discussed in section 2.2.3. The basic operation of WDM is illustrated in Figure 2.6.

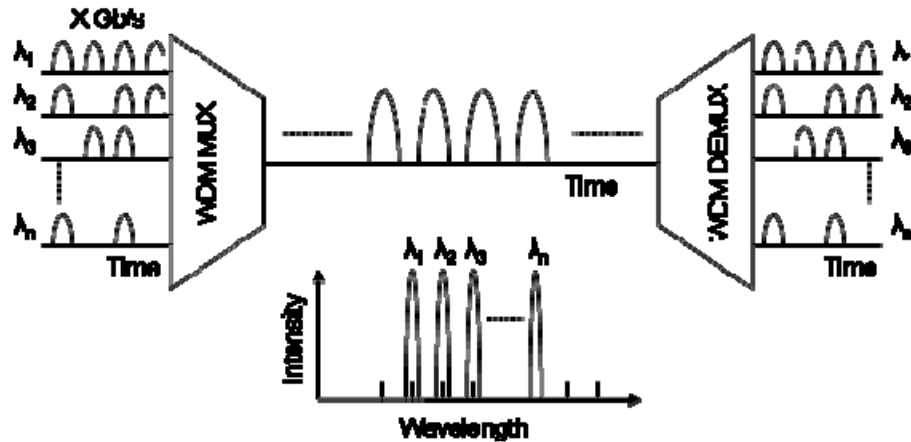


Figure 2.6: Basic wave division multiplexing (WDM) setup. This system multiplexes n optical channels, each of $X \text{ Gb/s}$, to combine for a total rate of $nX \text{ Gb/s}$

From Figure 2.6, WDM takes multiple optical input signals, multiplexes these signals together on different wavelengths by way of diffraction gratings, and sends all this information through a fiber as one WDM signal. Therefore, transmission of light on one fiber can send multiple signals, each containing large amounts of data at a time. This drastically increases the overall bandwidth of a single fiber. The major limitations of the WDM system are fiber nonlinearities and crosstalk. Both of these limitations cause multiple wavelengths to interfere with each other, thus degrading the performance of the system [72].

Commercial manufacturers have already released systems with 80 wavelengths operating at 40 Gb/s on each wavelength for a total of 3.2 Tb/s operation. Many different companies are competing to increase the bandwidth of the WDM system. Table 2.1 illustrates current capacities reported by companies that manufacture and distribute WDM systems.

Table 2.1: Capacities of current technology

Company	Number of Wavelengths	Transmission Speed per Channel (Gbps)	Total Transmission Speed (Tbps)	Distance km
Lucent Technology [104]	128	10	1.28	4000
Lucent Technology [104]	64	40	2.56	1000
Siemens [105]	80	40	3.2	2,000
Nortel [106]	32	10	320	n/a

2.2 A Basic Fiber Optic Communication Link

The basic fiber optic communication link consists of a transmitter and receiver operating at a wavelength of 1550 nm as shown in Figure 2.7. 1550 nm is chosen because it is the absorption or loss minimum in silica SMF and is within the EDFA spectrum of 1525-1570 nm [72]. The transmitter consists of a light source (laser) and data modulator. A distributed feedback laser (DFB) is most commonly used because of its wavelength tunability and stability, and its high output power [19]. The data modulator is either internal to the laser as in the case of direct modulation, or it is found external to the laser. External lithium niobate modulators have proven to be the modulators of choice for high speed, long distance links because of their high bandwidth and high extinction ratios. Furthermore, these modulators have also been used because they can be designed for zero chirp or adjustable chirp operation, thus minimizing fiber dispersion [94].

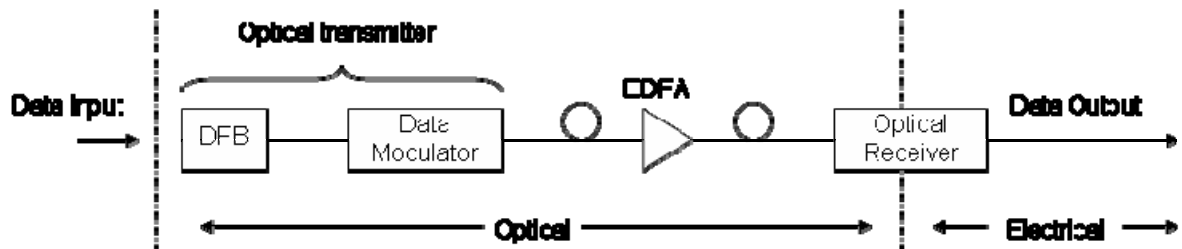


Figure 2.7: A basic modern fiber optic communication link consisting of an optical transmitter, amplifier, and receiver

As shown in Figure 2.7, a length of SMF connects the transmitter and receiver in the optical communication link. Because loss is an inherent property of the connecting optical fiber and other components of the link, optical amplifiers are implemented. Erbium doped fiber amplifiers (EDFAs) are most commonly used because they provide optical amplification at the same wavelength where silica fibers provide for the lowest loss [36]. These amplifiers are typically placed along the fiber channel as needed, but can also be placed at the output of the transmitter or at the input of the receiver.

The optical receiver is placed at the end of the optical communication link. Although many types of receivers are available, the main function of each particular receiver is to demodulate and detect the transmitted light, and to convert this light into an electrical signal. The receiver type and complexity depends on many factors including modulation format, bandwidth, gain, and dynamic range.

Although not displayed in Figure 2.7, other components used in the communication link such as fiber couplers, isolators, circulators, multiplexers, and filters can improve system performance or lead to more advanced forms of optical communication such as WDM. Most of these additional components are passive devices in that they achieve no gain but can induce loss and non-linearities. The following sections detail lasers, MZMs, and EDFAs. Section 2.4 is devoted entirely to a literature review of the optical receiver.

2.2.1 Lasers

The main light source for an optical communication link is the laser. The word laser stands for light amplification by stimulated emission of radiation. For communication links, lasers are designed for single-mode, high speed, and high power performance at 1550 nm. A well defined single-mode wavelength is needed to limit chromatic dispersion in long haul

communication links and to limit cross channel interference in WDM systems. This directly leads to a desire for narrow spectral width of the laser [36].

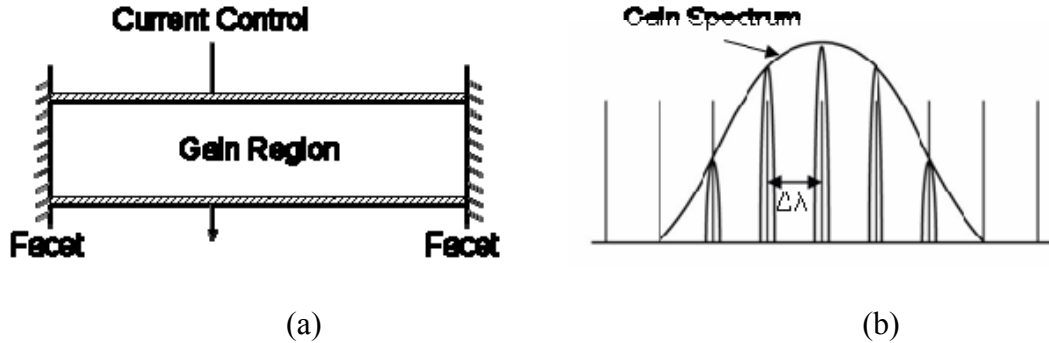


Figure 2.8: (a) Simple Fabry-Perot laser diagram (b) Multimode spectral characteristics

The simplest type of laser is the Fabry-Perot laser as pictured in Figure 2.8a. In the case of the Fabry-Perot laser, a length of active semiconductor gain medium is placed between two reflective dielectric mirrors or crystal facets. As light is created, a certain number of half wavelengths resonate within the cavity. The number of resonating wavelengths or modes, m , is given as:

$$m = \frac{2nL}{\lambda} \quad (2.29)$$

where n is the index of refraction of the gain medium, L is the distance between the two mirrors, and λ is the wavelength of interest [44]. The spacing between these modes, $\Delta\lambda$, is found by taking the derivative $d/d\lambda$ and given as:

$$\Delta\lambda = \frac{\lambda^2}{2L \left(n - \lambda \frac{dn}{d\lambda} \right)} \quad (2.30)$$

The width of each of the m number modes separated by $\Delta\lambda$ is determined by the quality factor, or Q factor, of the laser [32]. The Q factor can be determined by:

$$Q = \frac{f_o}{\Delta f_{1/2}} \quad (2.31)$$

where f_o is the center frequency and $\Delta f_{1/2}$ is the full width at half maximum (FWHM) given in equation 2.32.

$$\Delta f_{1/2} = \frac{c}{2nL} \frac{1 - (R_1 R_2)^{1/2}}{\pi (R_1 R_2)^{1/4}} \quad (2.32)$$

The multimode spectrum of the Fabry-Perot cavity is depicted in Figure 2.8b. The gain spectrum shown is associated with the medium within the cavity. For the InGaAsP semiconductor medium, the gain spectrum is centered on 1550 nm [67].

When the gain of the cavity is high and the reflectivity of the crystal facets is sufficiently large, the laser oscillates and light is produced at the output. This condition is known as the lasing threshold. For a simple Fabry-Perot laser, the output spectrum is multimode and consists of only resonant modes within the gain spectrum of the medium.

Although Fabry-Perot lasers exhibit high speed and high power operation, the chromatic dispersion of the multimode spectrum drastically limits performance in long-haul communications and the laser cannot meet the requirements for a high performance link. Furthermore, the line width is not suitable for WDM applications. Distributed feedback lasers (DFB) lasers, invented in 1970 [111] with narrow line widths, direct modulation, and high output power, have since replaced the Fabry-Perot lasers [36].

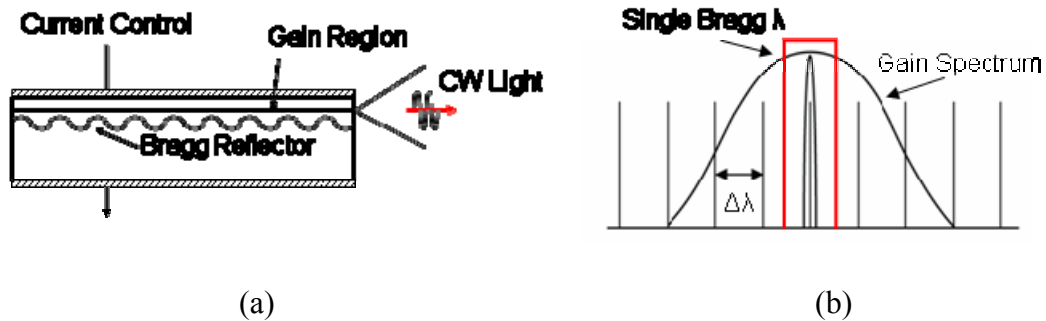


Figure 2.9: (a) Distributed feedback laser (b) Single-mode spectral characteristics

The distributed feedback laser (DFB), as depicted in Figure 2.9a, provides optical feedback that is highly wavelength selective. This allows the realization of a single longitudinal mode with a narrow spectral line width on the order of less than 1 MHz [36]. The DFB is similar to the Fabry-Perot laser in that it consists of a gain medium between two facets. However, light in the DFB is reflected by a distributed periodic grating, or change of index of refraction, within the gain region of the waveguide. Light is reflected, amplified, and output only if it satisfies the Bragg condition of reflection.

$$n_{eff} \Lambda = \frac{\lambda_o}{2} \quad (2.33)$$

where n_{eff} is the effective index of refraction of the gain medium, Λ is the period of the grating, and λ_o is the Bragg wavelength. If the DFB is designed correctly, a single longitudinal mode is passed at the Bragg wavelength [72].

The periodic grating within the DFB can be slightly altered by adjusting the temperature of the device. This effectively tunes the output wavelength of the DFB. Actual devices allow for a 3 nm-10 nm wavelength adjustment or about 0.1nm/°C change for the 1550 nm semiconductor laser [3, 46].

DFBs are used in most high speed optic systems; however, the increasing density of WDM systems is increasing the demand for more widely tunable lasers. In fact, the tunability of the transmission laser is desired to span the entire EDFA spectrum of approximately 35 nm. Such lasers have been demonstrated in research with tunabilities up to 42 nm [14, 20, 66]. Widely tunable 1550 nm lasers prove to increase functionality, performance, and flexibility of the WDM system.

2.2.2 External Optical Modulators

In addition to the laser, the transmitter includes either a direct or external optical modulator. In the direct case, the laser drive current is encoded with the data which effectively consists of turning the laser on and off to create a modulated optical output. In the external modulation scheme, the modulation occurs after the output of the laser. Presently, for bit rates larger than 10Gb/s, external modulation is used because direct modulation induces large amounts of chirp [93].

The two most common external modulators are the Mach-Zehnder modulator (MZM) and the electro-absorption modulator (EAM). The MZM is typically made of lithium niobate material and is external to the DFB, while the EAM can be fabricated in the same semiconductor (In-P based) as the DFB leading to the monolithic integration of the DFB and the EAM. One of the major advantages of the MZM over the EAM is that the MZM is capable of operating chirp-free [97].

The MZM is a lithium niobate device that relies on interferometer techniques for modulation as is illustrated in Figure 2.10. Lithium niobate is used because of its high electro-optic coefficient and low optical loss [94]. In this case, continuous wave (CW) light is sent into the modulator from a light source (e.g. DFB). The light is equally split into two paths of lithium niobate and recombined at the output. Because lithium niobate is an electro-optic material, the index of refraction of one path can be altered by applying voltage to it. A change in index of refraction causes an alteration in the light's phase. When the light from the two paths is recombined, variable interference occurs. If the two paths of light are completely in phase, constructive interference occurs and peak intensity is output. If the light is out of phase by π radians, destructive interference occurs, causing light to be dispersed

throughout the substrate; therefore, no intensity is output. If an electrical sinusoidal input of the correct drive strength is applied, the MZM creates pulses out of the CW light at a specified bit rate [94].

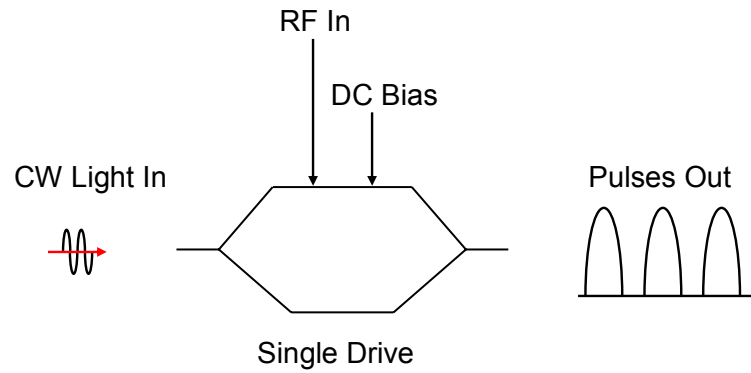


Figure 2.10: Basic Mach-Zehnder Modulator Schematic

Although Figure 2.10 illustrates the basic single drive MZM, a dual drive MZM can be implemented to work in a push-pull type configuration. The push-pull dual drive MZMs are most prevalently used for high speed, long distance fiber links because they can be designed for zero chirp or negative chirp operation, thus, minimizing fiber dispersion. The dual drive configuration also lowers the drive voltage and power consumption of the modulator. NTT Photonics reports a 4.5 x 0.8 mm dual drive lithium niobate MZM operating in a 40 Gb/s system. Figure 2.11 details the cross-section, schematic, and packaging of this device [97].

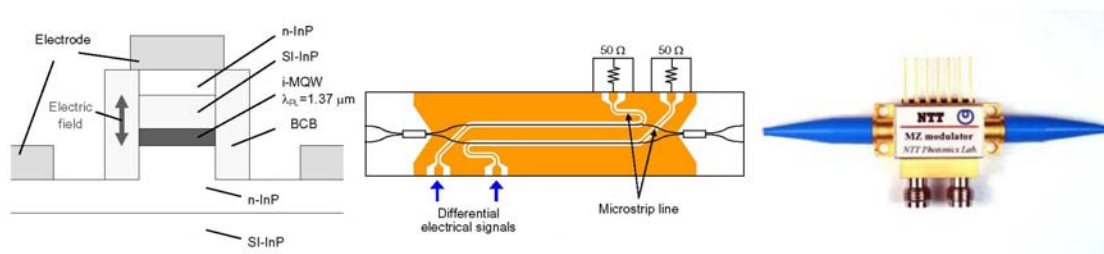


Figure 2.11: Cross section, schematic top view, and package view of dual drive lithium niobate MZM [97]

As previously mentioned, another common type of modulator is the electro-absorption modulator (EAM). The EAM is semiconductor based and can be monolithically integrated with the DFB. EAMs offer lower drive voltages and smaller chip size, which can, in turn, lower the overall size of the complete transmitter. While MZMs are usually used for high-speed, long-distance links, the EAM can be used in situations where short links are needed [97]. Furthermore, operation speeds of 40 Gb/s have also been reported for the integrated DFB and EAM making the EAM a possible alternative to the MZM when chirp is not a limitation [86].

The basic structure of an EAM consists of several InGaAsP quantum wells [86]. The bandgap of these quantum wells is higher than the incoming photons under normal conditions, allowing light to propagate through the material. When an electric field is applied, the semiconductor bandgap is lowered, causing full absorption of incoming light. This effect, known as the Franz-Keldysh effect, allows for the modulation of light in the EAM [64]. Figure 2.12 details the schematic of the lumped electrode EAM and DFB. The $90 \times 2 \mu\text{m}^2$ EAM integrated with a $450 \mu\text{m}$ long DFB has been reported to operate at 40 Gb/s. Another structure includes a traveling-wave electrode EAM designed to overcome the lumped electrode's speed limitations. This device, when integrated with a DFB laser, exhibited a bandwidth greater than 50 GHz [86].

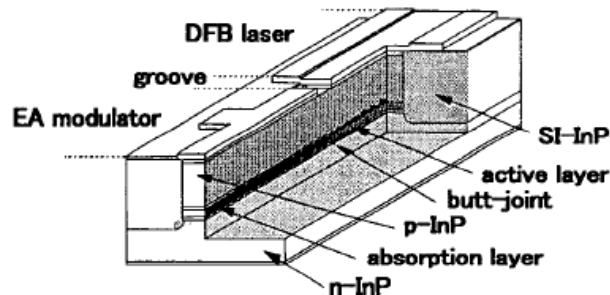


Figure 2.12: Monolithically integrated lumped electrode EAM and DFB laser [86]

2.2.3 Erbium Doped Fiber Amplifiers

Before optical amplifiers were available, multiple opto-electric regenerators were used in long-haul fiber systems to compensate for loss in the fiber. In addition to being very expensive, these regenerators are not robust to bit rate or modulation type. Therefore, any upgrades in transmission required a multitude of regeneration terminals to be upgraded. Furthermore, WDM was unfathomable using only opto-electric regenerators due to the sheer cost of implementing such a large number of terminals. After the invention of the EDFAs in 1987 [111], opto-electric regenerators could be placed further apart as EDFAs were used to increase the length of the fiber between regeneration spans. This sparked the WDM revolution where many opto-electric generators could be eliminated due to increased span length, making WDM a cost efficient solution [41].

The most common optical amplifiers are comprised of a length of optical fiber doped with rare earth elements such as erbium, ytterbium, neodymium, or praseodymium. Optical amplifiers of different rare earth elements in coordination with different types of fiber exhibit different amplifier properties. The single most common optical amplifier is the EDFA, which consists of a silica fiber doped with erbium ions (Er^{+3}) [41]. The EDFA has a gain spectrum of 1525-1570 nm, which is conveniently centered on the low loss spectrum of silica fiber [72]. The EDFA can be used to amplify optical signals, within its gain spectrum, of any bit rate or modulation format. Most importantly, the EDFA can be used to amplify multiple channels or wavelengths at the same time in coordination with WDM [41]. The amplifiers are typically placed along the fiber channel as needed, but can also be placed at the output of the transmitter or at the input of the receiver.

The principle of operation of the EDFA is to create population inversion which, in turn, leads to gain. The pump laser usually has a 980 nm wavelength; however, 1480 nm pumps are also used in EDFAs. 980 nm pumps are known for higher population inversion and lower noise figure, while 1480 nm pumps have higher quantum efficiency, when comparing pump power to signal power, and higher output power [36]. To understand the operation of the EDFA, a three band energy diagram is presented in Figure 2.13. Here, $E_1 < E_2 < E_3$. Each band of energies consists of closely spaced energy levels of erbium ions in silica. The spreading of individual energy levels into a continuous energy band is known as Stark splitting [41]. Any photon of energy $h\nu = E_2 - E_1$ can be amplified. Because many energy levels exist for each band, a broad range of energies can be amplified. This leads to the EDFA gain spectrum of 1525-1570 nm [72]. The continuous bands have been labeled ground, metastable, and pump for E_1 , E_2 , and E_3 respectively.

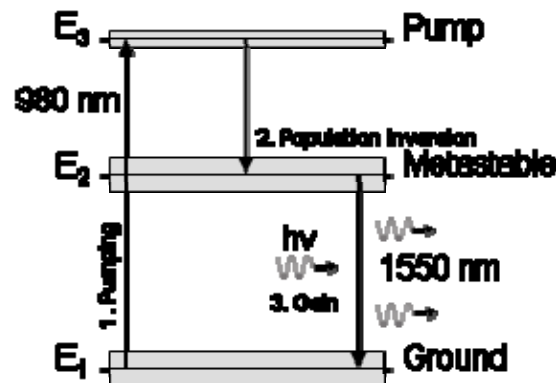


Figure 2.13: Three band energy diagram for EDFA

The amplification process can be split up into three stages – pumping, population inversion, and stimulated emission or gain. During the pumping stage, a pump laser excites erbium ions from the ground state to the pump band. The excited ions then quickly decay to the metastable band by way of spontaneous emission. Because the lifetime of this decay is very short (1 μs) as compared to the lifetime of decay between the metastable band and

ground band (10 ms), population inversion occurs between E_1 and E_2 . This population inversion directly leads to gain. As photons pass into the device, stimulated emission occurs causing a single photon to emit multiple new photons of the same energy, direction, and polarization [41].

Two important characteristics of the EDFA are gain flatness and gain spectrum. Gain flatness is critical in WDM systems, so that all channels or wavelengths have the same level of gain independent of wavelength. Although this is not the case in the typical EDFA as seen in Figure 2.14, many techniques are available to increase the overall gain flatness. Filters can be placed inside the amplifier to reduce peak gains or different types of fibers can be used such as fluoride glass to improve natural flatness [13]. Commercial optical amplifiers rely on multiple stages and feedback mechanisms and can achieve 0.1 db gain flatness over the entire C-band [30, 74, 87]. For single stage amplifiers, broad spectrum pump sources have been investigated as a possibility to increase gain flatness [5].

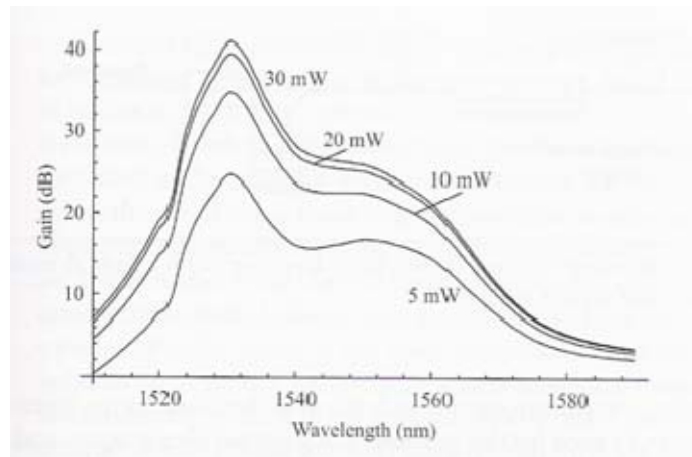


Figure 2.14: Gain of typical EDFA as function of wavelength and pump power [72]

Gain spectrum is also of importance for WDM applications. If the spectrum of the EDFA increases, more channels can be implemented, thus increasing the overall bandwidth and capacity of the system. Typical EDFAs operate in the C-band (1525-1570 nm) of optical

fiber. Investigations on L-band (1570-1620 nm) EDFAs [11, 70, 99] and very wide band EDFAs covering both the C and L-bands (1525-1620 nm) for WDM channels have been reported using either different dopant elements or novel design [35, 60, 103].

2.3 Modulation Formats

Figure 2.15 provides a detailed summary of the advanced optical modulation formats available in fiber communication systems with optical spectra and intensity eye diagrams. The figure includes return-to-zero and nonreturn-to-zero on-off-keying (RZ, NRZ-OOK), carrier-suppressed (CS)RZ-OOK, chirped (C)RZ-OOK, duobinary (DB), RZ-alternate-mark inversion (RZ-AMI), vestigial sideband (VSB)-NRZ-OOK, VSB-CSRZ-OOK, NRZ and RZ differential phase shift keying (NRZ / RZ-DPSK), and NRZ and RZ differential quadrature phase shift keying (NRZ / RZ-DQPSK).

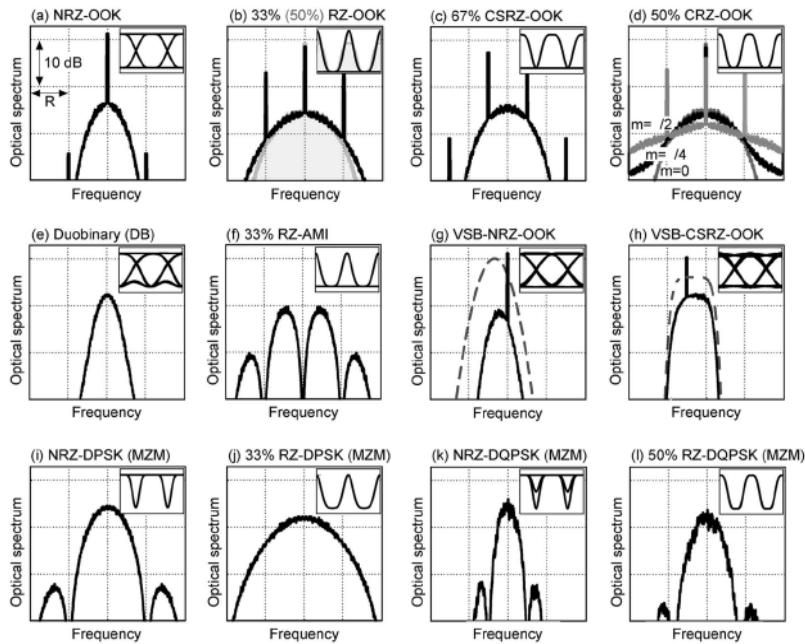


Figure 2.15: Optical spectra and intensity eye diagrams for various modulation formats [93]

From those presented, each format can be classified as either intensity modulation or phase modulation depending on how the data is encoded. In intensity modulation, the power

is switched between a maximum and a minimum to carry data. Examples of intensity modulation include OOK, DB, and AMI. In phase modulation, data is encoded as phase changes between adjacent optical bits. An example of phase modulation is differential phase shift keying DPSK or differential quadrature phase shift keying DQPSK [93]. Since most optical receivers use photodiodes which are inherently phase insensitive for optical detection, they can only directly detect intensity modulated signals. If phase modulation is implemented at the transmitter, the optical signal must first be demodulated into intensity modulation before detection at the receiver [24].

The present work focuses on differential phase shift keying as it offers a 3-dB sensitivity advantage over OOK modulation when using balanced detection, allowing for the extension of transmission distances or reduction of optical power requirements in fiber communication systems. Furthermore, it is limited to NRZ-DPSK, as NRZ-DPSK links have already proved to be a quality choice for data rates from 10 to 42.7 Gb/s, achieving record transmission distances in long-haul communication links [9, 24, 101].

2.3.1 On-Off Keying

In NRZ-OOK systems, the data is intensity modulated which is equivalent to optical energy in the '1' bit slot and no energy in the '0' bit slot. Since the data is intensity modulated (no information on the phase), photodiodes can directly translate the optical signal to an electrical current at the receiver.

This concept also applies to the RZ-OOK case. Here, optical pulses are present for '1's and nonexistent for '0's. A simple RZ-OOK system is shown in Figure 2.16.

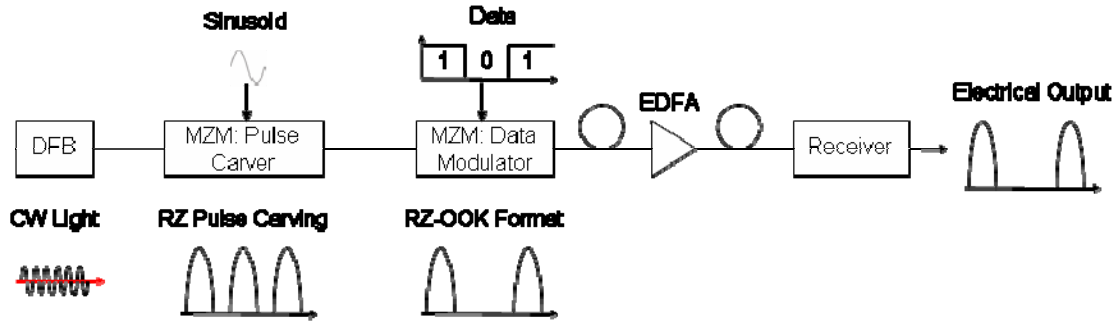


Figure 2.16: Simple RZ-OOK system diagram

In this schematic, CW light is carved into pulses of a specified bit rate by a MZM driven with an electrical sinusoid. This MZM is sometimes referred to as the ‘pulse carver’. Pulses of different duty cycle (33, 50, 67%) can be carved by changing the bias and drive voltages of the pulse carver. Data is then encoded over these pulses with a second MZM creating the RZ-OOK signal. The optical signal is sent through a length of SMF to the receiver, where it is detected and amplified [93].

2.3.2 Differential Phase Shift Keying

DPSK offers a 3-dB sensitivity advantage over OOK modulation when using balanced detection. This advantage comes from the fact that for the same average optical power, there is $\sqrt{2}$ increase in symbol distance over OOK that can extend transmission distances or reduce optical power requirements in a communication system [24]. DPSK can also be more robust to fiber nonlinearities, as the DPSK peak intensity is lower for the same average optical power as OOK. However, unwanted intensity modulation converted into phase modulation still limits the DPSK system. This is known as the Gordon-Mollenauer effect and is detailed in [42-43]. Both NRZ and RZ formats are available in DPSK; however, RZ-DPSK is more robust to ISI, fiber nonlinearities, and PMD [9, 93].

In DPSK systems, data is encoded by the phase change between adjacent bits. If no phase change exists between adjacent bits, a logical '1' is detected. If there is an exact π phase change between adjacent bits, a '0' is detected. Because most standard photo detectors are phase insensitive, the phase modulated signal must first be demodulated into an intensity modulated signal before detection. This demodulation is done by way of a 1-bit delay interferometer (DI). In the DI, the DPSK signal is split into two equal signals. One of these signals is then delayed by exactly 1 bit as compared to the other. The two signals are interfered and either constructive or destructive interference occurs. If there is no phase change between adjacent bits, a pulse will be output on the constructive interference port. If there is an exact π phase change between adjacent bits, a pulse is output on the destructive interference port. This effectively converts the phase modulated signal into two logically-inverted intensity modulated signals. These two signals can then be detected by using a balanced receiver – the basis of this thesis research.

A simple RZ-DPSK system is shown in Figure 2.17.

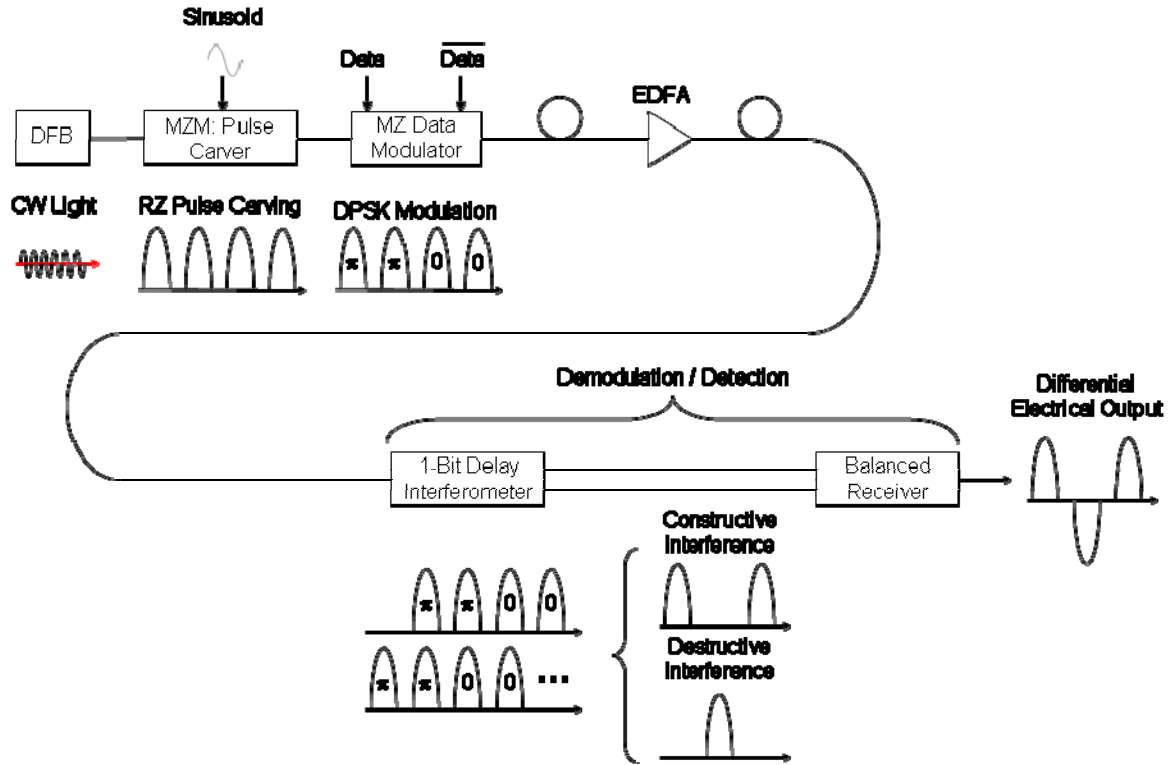


Figure 2.17: Simple RZ-DPSK system diagram

In this schematic, CW light is carved into pulses at the desired bit rate by a MZM driven with an electrical sinusoid. Data is then encoded onto the pulses by changing the phase between adjacent pulses by way of a second MZM. A dual drive MZM is used for data modulation to ensure an exact π phase change when needed. This MZM is driven such that it allows for zero-chirp operation [24]. After encoding the data, the DPSK modulated signal is sent through a length of fiber to the receiver. As previously mentioned, the signal is demodulated at the receiver by way of a 1-bit DI. The most common DI is the integrated MZM delay interferometer [24], but other forms include a free space Michelson interferometer approach [49], and an innovative solution using a length of polarization maintaining fiber and polarizing beam splitter [12]. After the light is demodulated into two logically-inverted intensity modulated signals, it can be detected and amplified by a balanced receiver.

2.4 The Optical Receiver

2.4.1 Introduction

The main function of the optical receiver is to demodulate and detect the transmitted light, and to convert it into an electrical signal. The different components used in receiver depend on many factors including the modulation format and bit rate of the system.

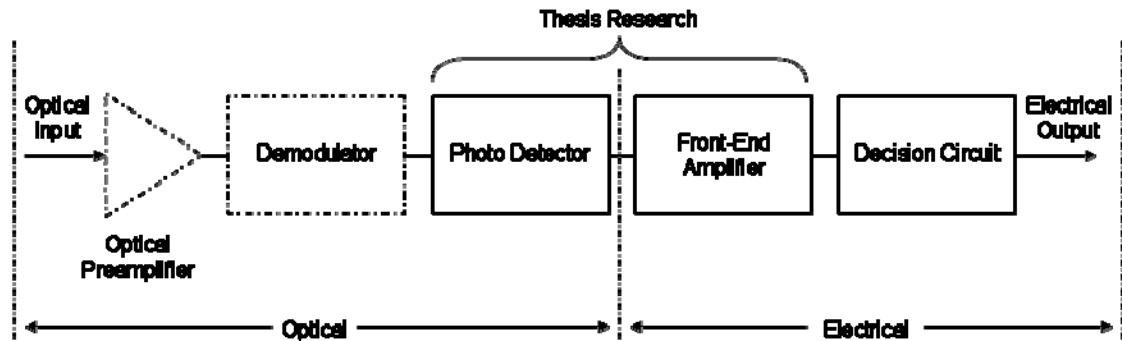


Figure 2.18: Outline of the optical receiver

Figure 2.18 provides the general outline of the optical receiver with five major components. The first is an optional optical preamplifier. Optical preamplifiers are often used in long-haul communication systems to improve the sensitivity of the receiver. However, in addition to increasing sensitivity, optical preamplifiers induce unwanted output noise caused by spontaneous emission within the amplifier that can increase the ISI in the receiver [36]. The next component listed is the demodulator. The modulation format of the system dictates the need for a demodulator at the receiver. Any phase modulated signal must first be converted into an intensity modulated signal before detection by the photodiodes. As discussed in section 2.3.2, a 1-bit delay interferometer is used to demodulate DPSK data [24].

Rather than using a preamplified receiver, this thesis will consider sensitivity improvement by integrating the next two major components – the photo detector and the front-end amplifier. The photo detector is responsible for converting the optical signal into an

electrical signal, while the front-end amplifier amplifies the output of the photo detector to an acceptable level for the post amplifier and decision circuit. Among the more popular photo detector choices are PIN photodiodes (PIN-PD), vertically illuminated photodiodes (VIPD), waveguide photodiodes (WGPD), distributed photodiodes, and avalanche photodiodes (APD). Each will be discussed in detail in section 2.4.3. Two major types of front-end amplifiers exist – the high impedance amplifier and the transimpedance amplifier. Most commonly, the front-end amplifiers incorporate heterojunction bipolar transistor (HBT) or high-electron-mobility transistor (HEMT) technology. Front-end amplifiers will be discussed in Section 2.4.4. The final component of the receiver is the decision circuit which is used for post electronic processing. Decision circuitry depends on the modulation format and is used to evaluate the data seen at the output of the front-end receiver.

Different receiver configurations can be used in an optical communication link depending on the applications (modulation format, data rate, distance, cost, etc.). Figure 2.19 and Table 2.2 illustrate some reported experimental receivers and their corresponding sensitivities, where sensitivity is defined as the average optical power required to achieve a bit-error-rate (BER) of 10^{-9} at a given bit rate. It should be noted that unless otherwise stated, results are presented for a 1550 nm OOK optical link. Also, each receiver is classified as either a monolithic optoelectronic integrated circuit (OEIC) or hybrid.

Table 2.2: Experimental receiver sensitivity

Bitrate (Gb/s)	Sensitivity (dBm)	OEIC / Hybrid	Receiver Topology	Receiver Technology	DPSK?	Ref
10	-16.1	OEIC	WGPD + TIA	InAlAs-InGaAs HEMT	NO	[84]
10	-17.3	OEIC	PIN + TIA	InAlAs / InGaAs HEMT	NO	[2]
10	-19.0	Hybrid	PIN + TIA	GaInP:GaAs HBT	NO	[79]
10	-19.2	OEIC	PIN + TIA	InAlAs / InGaAs HEMT	NO	[47]
10	-20.4	OEIC	PIN + TIA	InP-InGaAs HBT	NO	[51]
10	-23.5	Hybrid	PIN + 3 Stage CS amplifier *	HEMT	NO	[100]
10	-26.0	Hybrid	APD + TIA	GaAs HEMT / SiGe HBT	NO	[34]
10	-28.1	Hybrid	APD + TIA	InGaP/GaAs HBT	NO	[98]
10	-30.0	Hybrid	APD	APD	NO	[63]
10	-29.5	Hybrid	APD + TIA	SiGe HBT	NO	[58]
10	-43.7	Hybrid	EDFA + PIN + Front End Amp	Balanced PIN	YES	[4]
40	-8.0	Hybrid	WGPD + TIA + Limiting Amp	InP / InGaAs HBT	NO	[6]
40	-8.4	OEIC	WGPD + Diff Distributed Amp	InP HEMT	YES	[76]
40	-9.4	OEIC	PIN + TIA	InP HBT	NO	[45]
40	-11.2	OEIC	WGPD + TWA	GaAs pHEMT	NO	[89]
40	-25.0	OEIC	Optical Preamp (SOA) + PIN **	SOA + PIN	NO	[78]
40	-27.5	OEIC	Optical Preamp + UTC-PD + HEMT IC ***	InP HEMT	NO	[77]
40	-35.7	Hybrid	EDFA WGPD + Diff TWA	SiGe HBT	YES	[80]
42.7	-36.2	Hybrid	Optical Preamp + Diff TIA	TIA	YES	[23]
42.7	-37.0	Hybrid	Optical Preamp + Diff Linear Amp	SiGe Linear Amp	YES	[81]
50	-7.6	Hybrid	UTC-PD + TIA	InP HEMT	NO	[22]
50	-22.7	OEIC	WGPD + Distributed Baseband Amp	InAlAs-InGaAs-HEMT	NO	[85]

* CS: Common Source

** SOA: Semiconductor Optical Amplifier

*** UTC: Unitraveling-carrier Photodiode

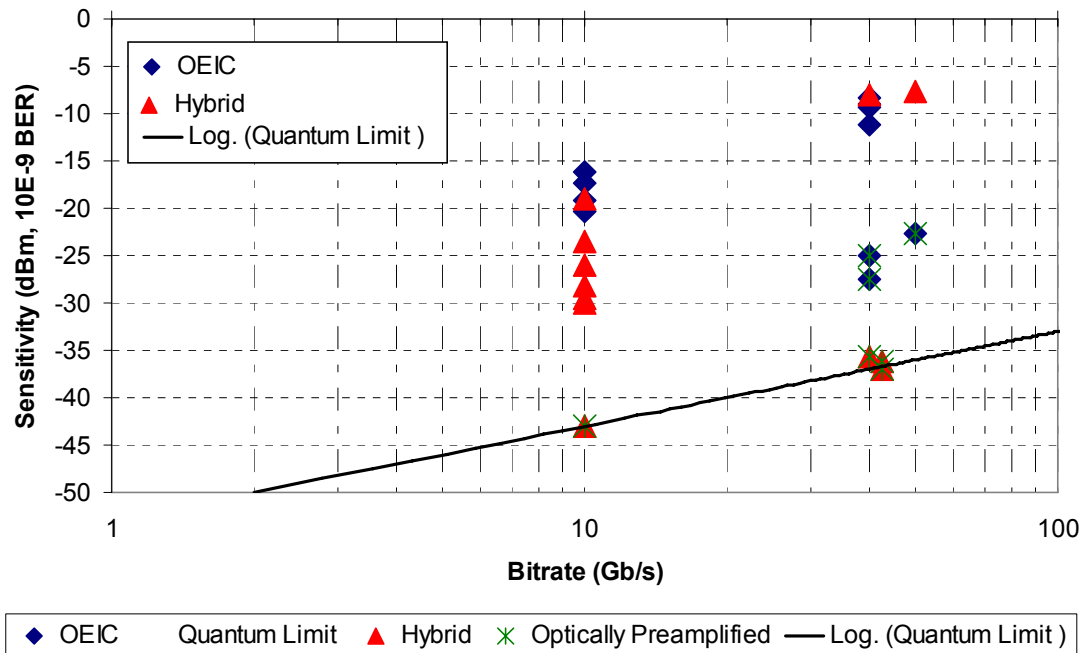


Figure 2.19: Experimental receiver sensitivity

As Figure 2.19 displays, receivers with low sensitivity have already been implemented. The focus of this thesis is the design, analysis, and simulation of an innovative receiver for a high-speed DPSK optical communications link – specifically a receiver consisting of two balanced WCPDs integrated with a differential TIA HBT front-end amplifier for a 40 Gb/s DPSK long-haul communication link.

2.4.2 Defining Receiver Performance Parameters

Before the receiver can be designed and analyzed, it is best to define certain parameters that provide a measure of how well a receiver performs. Performance of the receiver can be split up into three categories: photo detector performance, front-end amplifier performance, and entire receiver performance.

The photo detector performance depends on parameters defined by quantum efficiency, responsivity, and the gain-bandwidth product. The quantum efficiency, η , is defined as the number of carriers generated per incident photon proportional to the ratio of

absorbed optical power, P_{abs} , to incident optical power, P_{in} . It varies between zero and one, with one being ideal, and is a function of the photo detector material's absorption coefficient, α . The absorption coefficient is a measure of how well a material absorbs light and is highly wavelength dependent. Therefore, quantum efficiency is also a function of wavelength.

$$\eta = \frac{P_{abs}}{P_{in}} \quad (2.34)$$

The second major performance parameter of the photo detector is the responsivity of the detector. Responsivity, $R_{A/W}$, is the ratio of average output current, I_p , to incident optical power, P_{in} .

$$R_{A/W} = \frac{I_p}{P_{in}} \quad (2.35)$$

Responsivity can also be expressed in terms of wavelength by realizing that only a percent of incident light is converted into electrical current, as dictated by the quantum efficiency.

Therefore, $R_{A/W}$, in terms of A/W, can be expressed as:

$$R_{A/W} = \frac{e\eta\lambda}{hc} = \frac{\eta\lambda}{1.24} \quad (2.36)$$

where e is the charge of an electron, h is plank's constant, and λ is the wavelength of operation in μm . If the efficiency is close to 1, responsivities of 1.25 can be achieved for 1550 nm detectors.

For the gain-bandwidth product, the bandwidth is defined as the amount of spectrum that photo detector can detect before its gain profile falls off by 3-dB. The gain, G , of the photo detector is simply the ratio of converted input optical power to output electrical power. Most PIN or Schottky-barrier type photodiodes have a gain of almost unity; however, avalanche photodiodes have the distinct property of very high or even infinite gain. The gain-

bandwidth product is the multiplication of the gain and bandwidth of a photo detector. It is useful because there usually exists an inherent tradeoff between gain and bandwidth in the photo detector. It can be noted here that some photodiodes also have tradeoffs between bandwidth and efficiency. Therefore, some sources site a bandwidth-efficiency product as a means for measuring performance of the photo detector.

Now that the photo detector has been discussed, performance parameters for the front-end amplifier will be determined. These parameters include dynamic range, low frequency gain, bandwidth, unity gain frequency, and the scattering parameters.

Optical dynamic range is defined as the difference between the smallest and largest current values that can be successfully amplified by the front-end amplifier. This becomes important when the input power to the photo detector is not a constant value. The low frequency gain is the gain of the amplifier when operating just above 0 Hz. The bandwidth of the front-end amplifier is again defined by the 3-dB frequency (frequency at which gain rolls off by 3-dB). The unity gain frequency is the frequency at which the gain is 1 or 0-dB.

Determining the scattering parameters (S-parameters) is an effective means for understanding front-end amplifier performance. They provide a complete description of an amplifier with a total number, N , of input and output ports. To accomplish this task, the scattering parameters relate the voltage waves incident on the ports to those reflected from the ports. The scattering matrix which defines these reflections is given as:

$$\begin{bmatrix} V_1^- \\ V_1^- \\ \vdots \\ V_N^- \end{bmatrix} = \begin{bmatrix} S_{11} & S_{12} & \cdots & S_{1N} \\ S_{21} & & & \vdots \\ \vdots & & & \\ S_{N1} & \cdots & & S_{NN} \end{bmatrix} \begin{bmatrix} V_1^+ \\ V_2^+ \\ \vdots \\ V_N^+ \end{bmatrix} \quad (2.37)$$

where V_x^+ is the amplitude of the voltage wave incident on port x, and V_x^- is the amplitude of the voltage wave reflected from port x [71]. Any element in this matrix can be found by:

$$S_{ij} = \left. \frac{V_i^-}{V_j^+} \right|_{V_k^+ = 0 \text{ for } k \neq j} \quad (2.38)$$

For a simple two port amplifier, the four S-parameters correspond to four important characteristics of the amplifier [71]. These are listed below.

S_{11} = Input reflection (A well matched amplifier is defined as an amplifier with $S_{11} < -10\text{-dB}$)

S_{22} = Output reflection (A well matched amplifier is defined as an amplifier with $S_{22} < -10\text{-dB}$)

S_{21} = Gain of the amplifier

S_{12} = Reflection from output to input

The transimpedance, TZ, of an amplifier can also be determined from the S-parameter as shown in equation 2.39.

$$TZ = \frac{Z_0 S_{21}}{(1 - S_{11})} \quad (2.39)$$

Here, Z_0 is the characteristic impedance of the system. Normally, Z_0 is set to 50 Ohms.

Now that the performance parameters for the individual photo detector and front-end amplifier have been discussed, parameters of the entire receiver can be defined. These parameters include sensitivity, bit-error-rate (BER), and the ‘openness’ of the eye diagram. Sensitivity has already been used to compare multiple receivers in Figure 2.19 and Table 2.2. It was defined as the average optical power required for achieving a certain bit-error-rate (BER) at a desired bit rate. BER is simply defined as:

$$BER = \frac{\# Errors}{Bit} \quad (2.40)$$

Most communication link standards require a BER of 10^{-12} while transmitting a pseudo-random bit sequence (PRBS) of length $2^{31}-1$ [36].

Eye diagrams provide a visual identification for the quality of the received signal. In an eye diagram, received bit periods are superimposed on top of each other and aligned to a common timing reference. The vertical eye opening is the margin for voltage errors, while the horizontal opening is the margin for timing errors. The size of the opening indicates the amount of voltage and timing margin available to sample the signal. The eye is considered ‘open’ if these voltage and timing margins are within specifications set for the receiver. The tradeoff between the voltage and timing margins that can be exploited to ensure the eye is open in both directions. An example eye diagram is given in Figure 2.20 [16].

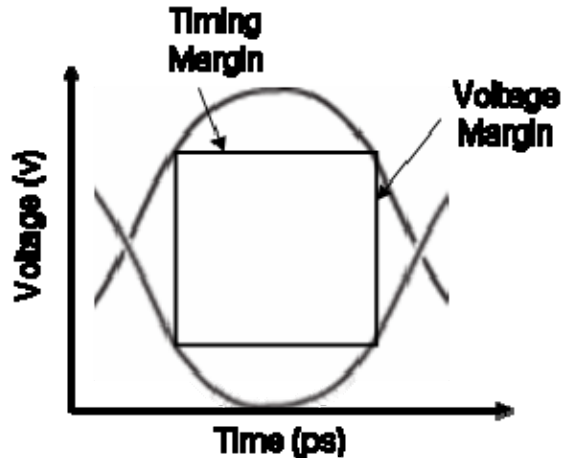


Figure 2.20: Example eye diagram

One additional highly important performance parameter is noise. Noise will not be defined in this chapter; however it will be discussed in chapter 5 of this thesis. At this point, enough is known about the receiver performance to discuss possible receiver configurations.

This discussion will follow in the next three sections followed by section 2.4.6 which gives the general outline for the DPSK receiver analyzed in this thesis.

2.4.3 The Photo Detector

As previously mentioned, popular choices for the photo detector include vertically illuminated photodiodes (VIPD), waveguide photodiodes (WGPD), distributed photodiodes, and avalanche photodiodes (APD). Each of these diodes is a more complex version of the simple the PIN photodiodes (PIN-PD). This section details the operation of each detector.

2.4.3.1 PIN Photodiode

High speed, high responsivity, low cost, and small size and weight make the PIN-PD an attractive choice when dealing with optical detecting applications. Furthermore, the bandgap of the materials used to make these detectors can be matched to wavelengths used in many high speed optical applications, such as in the case of InGaAs and InGaAsP material allowing detection of 1550 nm light [44]. Before more advanced types of PIN photodiodes can be introduced, the basic operation of the PIN photodiode should be discovered.

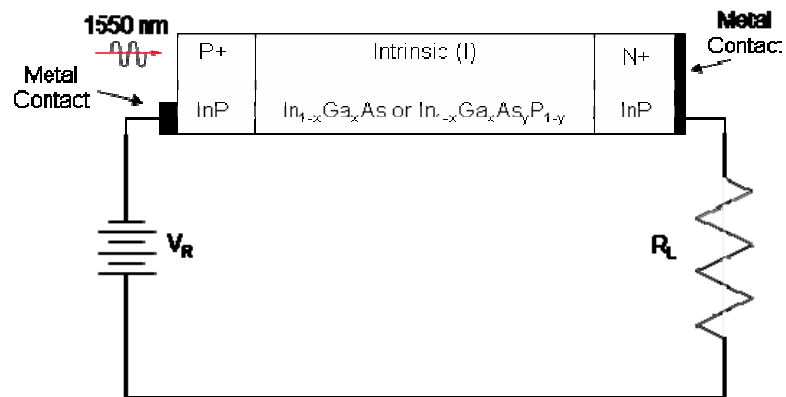


Figure 2.21: Typical 1550 nm photodiode in photoconductive mode [25]

As seen in Figure 2.21, the PIN-PD is composed of three layers – the P layer, the I layer, and the N layer. Most commonly a double heterojunction, or two junctions of completely different semiconductors, is implemented. This ensures that light is only absorbed

in the I layer of the device. The P layer is heavily doped with acceptors, while the N layer is heavily doped with donors. Both can be composed of InP in the case of 1550 nm detection. The I layer is an intrinsic region that is theoretically undoped. It is composed of InGaAs or InGaAsP in the case of 1550 nm detection. When a voltage, V_R , is applied to the device, the device is operated in reverse bias with a typical load impedance, R_L , of 50Ω [39]. This reverse bias operation produces an electric field in the intrinsic region which creates a region where no free carriers exist [25]. This region is known as the depletion region, W , and is given in equation 2.41.

$$W = \sqrt{\frac{2\epsilon(V_{bi} + V_{applied})}{q} \left(\frac{1}{N_a} + \frac{1}{N_d} \right)} \quad (2.41)$$

where V_{bi} is the electric potential, $V_{applied}$ is the applied voltage, and N_a and N_d are the acceptor and donor concentrations respectively [44]. As V_R is increased, the depletion width increases until it equals that of the intrinsic width [25].

When light shines into the I region of the device, photons are absorbed. Light is not absorbed by the P or N regions because their material is transparent to the wavelength of interest, i.e. the band gap energy of the P and N region is purposely too large. The absorption process provides enough energy so that an electron moves from the valence band to the conduction band; thus, causing the creation of an electron-hole pair. Current is produced when the electron-hole pair is separated by the electric field, causing the electron to diffuse to the P region and the hole to diffuse to the N region [25]. As incident light increases, the produced photocurrent also increases. Figure 2.22 depicts the operation of the photodiode with increasing light. The current can be given as:

$$i_s = \frac{\eta e}{h\nu} P \quad (2.42)$$

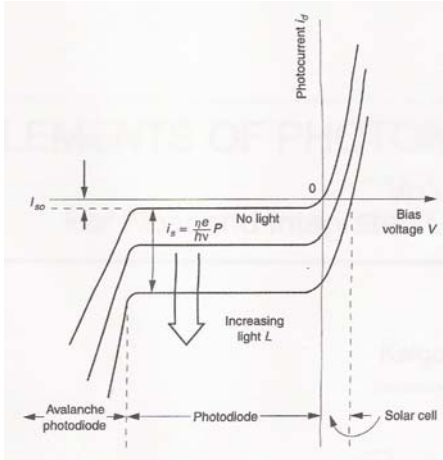


Figure 2.22: Current-voltage characteristic of a p-n junction [32]

The two major performance affecters are the RC time constant and the drift transient time. Each contributes to the overall response time or bandwidth of the photodiode. First, as in the case of any diode, the PIN-PD has an intrinsic resistance, R_S , and capacitance, C . The intrinsic resistance is due to the bulk and spreading resistance of the device. However, in most cases, this resistance is negligible when compared to the resistance of the load. The parallel plate capacitance is given in the below equation with A being the area of the detector [44].

$$C = \frac{\epsilon A}{W} \quad (2.43)$$

Knowing the resistance and capacitance of the diode allows for the calculation of the RC time constant, $t_{RC} = 2.2 R_L C$. If this RC time constant is small, the response time of the device decreases, causing bandwidth to increase [25].

The second major performance affecter is the drift transient time. As electron-hole pairs are created in the depletion region, the electrons drift to the P layer, while the holes drift to the N layer. The time it takes for this drift to complete is the drift transient time. If this time is short, the response time of the device decreases, causing bandwidth to increase [44].

The transient time is given as $t_{drift} = 0.79 W / V_s$, where V_s is the saturation velocity of the electrons [25].

As one can conclude, there is an intrinsic tradeoff between the time constant and the drift transient time. If W is increased, the capacitance of the devices decreases allowing for shorter response times. At the same time, as W is increased, the transient drift time is increasing creating longer response times. Therefore, to allow for the optimal condition, the time constant must be set equal to the drift transient time. This is seen in the below equation where t_{total} is the total response time [44].

$$t_{total}^2 = t_{RC}^2 + t_{drift}^2 \quad (2.44)$$

$$t_{RC} = t_{drift} \quad (2.45)$$

If the time constant and the drift transient time are set equal to one another, the shortest response time allowed is found, $t = 1.11 W / V_s$. This allows for the maximum bandwidth of the PIN-PD [25].

2.4.3.2 Vertically Illuminated Photodiode

Now that the general operation of a simple PIN photodiode along with its major design tradeoff has been realized, more complex photodiodes can be introduced that are capable of receiving signals of 10-Gb/s and above [38].

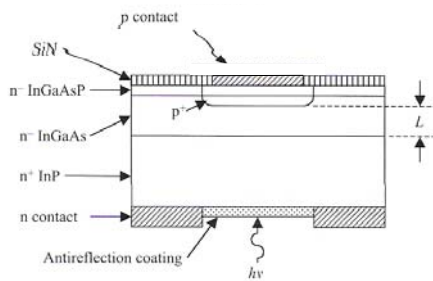


Figure 2.23: Vertical illuminated photodiode [38]

The vertically illuminated photodiode is provided in Figure 2.23. Here, the photon is sent vertically into the bottom of the device. The photon then passes through the N layer and into intrinsic layer (below the P layer), where it is absorbed. Upon absorption, current is produced in the same manner as previously explained. Based on Bower's analysis, the frequency response can be given by the following equation for an arbitrary αL [6].

$$\frac{i(\omega)}{i(0)} = \frac{1}{(1 - e^{-\alpha L})} \left[\frac{1 - e^{-j\omega\tau_n - \alpha L}}{j\omega\tau_n + \alpha L} + e^{-\alpha L} \frac{e^{-j\omega\tau_n} - 1}{j\omega\tau_n} + \frac{1 - e^{j\omega\tau_p}}{j\omega\tau_p} + e^{-\alpha L} \frac{1 - e^{-\alpha L - j\omega\tau_p}}{\alpha L - j\omega\tau_p} \right] \quad (2.46)$$

“where i is the detected current, ω is the angular modulation frequency, $t_n(=L/v_n)$ and $t_p(=L/v_p)$ are the electron and hole transit times, respectively, and v_n , and v_p are the electron and hole velocities, respectively” [6].

The above frequency response is directly related to the electron and hole transit times. It shows that the best frequency response can be achieved with small transit times. These transit times can be decreased by decreasing the thickness of the I layer. However, as previously determined, decreasing the thickness of the I layer increases the capacitance or RC time constant of the circuit. Therefore, the tradeoff is again exhibited in this particular case of the vertically illuminated photodiode [6].

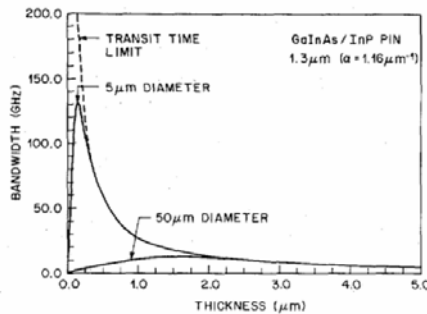


Fig. 4. GaInAs p-i-n detector bandwidth dependence on depletion-layer thickness for 5 and 50 μm diameters. ($\alpha = 1.16 \mu\text{m}^{-1}$ (1.3- μm wavelength) $v_n = 6.5 \times 10^6 \text{ cm/s}$, $v_p = 4.8 \times 10^6 \text{ cm/s}$.)

Figure 2.24: Plot illustrating tradeoff between thickness and bandwidth. (As the thickness decreases for a particular device, BW increases. However, once the thickness passes the point at which the time constant equals the transient time, BW begins to suffer) [6]

Another problem can be discovered for the vertically illuminated photodiodes. As the I layer is decreased, the quantum efficiency of the photodiode is also severely decreased. This creates an additional intrinsic tradeoff. As bandwidth increases for the vertically illuminated photodiode, the quantum efficiency diminishes [6]. This particular tradeoff is illustrated below in Figure 2.25.

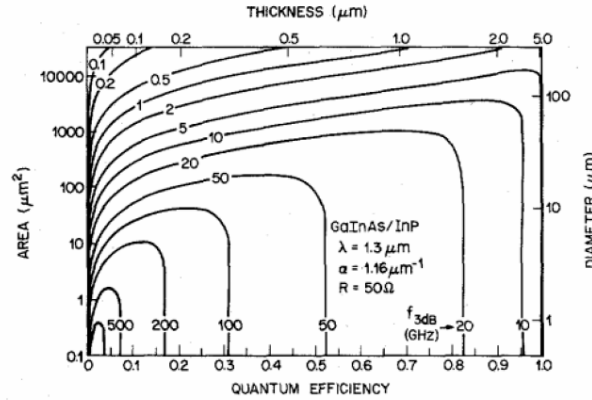


Fig. 5. Contours of constant 3-dB bandwidth in the detector-area, depletion-layer-thickness plane. ($\alpha = 1.16 \mu\text{m}^{-1}$, (1.3- μm wavelength), $v_n = 6.5 \times 10^6 \text{ cm/s}$, $v_p = 4.8 \times 10^6 \text{ cm/s}$, $\epsilon = 14.1$.)

Figure 2.25: Bandwidth versus quantum efficiency tradeoff [6]

The tradeoff between bandwidth and quantum efficiency can be quantitatively analyzed by way of the bandwidth-efficiency product. The below equations illustrate this concept for a single pass vertically illuminated photodiode working at very high speeds with a thin absorbing layer.

$$\eta = (1 - R)(1 - e^{-\alpha L}) \approx (1 - R)\alpha L \quad (2.47)$$

where the internal quantum efficiency of the detector is found with R as the Fresnel reflectivity [6]. The bandwidth is given as:

$$BW = f_t \approx \frac{0.45v}{L} \quad (2.48)$$

where v is the carrier saturation velocity and L is the carrier transit distance [44]. Finally, the bandwidth-efficiency product can be given as follows.

$$f_i \eta = 0.45 \alpha v (1 - R) \quad (2.49)$$

Since the saturation velocity and Fresnel reflectivity do not change, a large absorption coefficient must be chosen to achieve high bandwidth-efficiency products.

In addition to using high absorption materials, there is another way to further increase bandwidth in vertically illuminated photodiodes. This method is known as the “double-pass scheme” and is illustrated in Figure 2.26 [39]. When fabricating the detector, a highly reflective P contact is used. As light passes through the detector, some is absorbed in the intrinsic region as previously discussed. Light that is not absorbed moves to the P contact, where it is reflected back towards the intrinsic layer allowing for additional absorption. This double pass scheme can further increase the efficiency of the detector and the bandwidth-efficiency product. The effect is shown mathematically below where r is the reflection coefficient of the P contact [39].

$$\eta = (1 + r e^{-\alpha L})(1 - e^{-\alpha L}) \approx (1 + r) \alpha L \quad (2.50)$$

The bandwidth-efficiency condition becomes:

$$f_i \eta = 0.45 \alpha v (1 + r) \quad (2.51)$$

Therefore, using the double-pass scheme (Figure 2.26) allows for the bandwidth-efficiency product to be increased by a $(1+r)$ factor. In real life applications, an obtainable bandwidth-efficiency product is somewhere in the range of 20-35 GHz [39]. Although this provides for higher bandwidths at higher efficiency's, it does not solve for the problem of the tradeoff between the two. Thus, both factors still limit each other. Another type of detector must be realized if the bandwidth and efficiency are to be taken independent of one another, allowing for high speed detection.

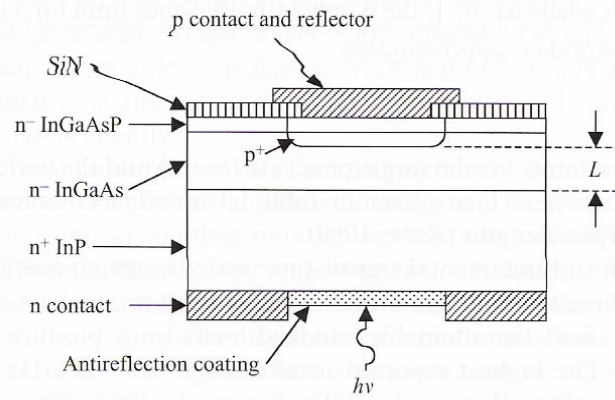


Figure 2.26: Double-pass vertical illuminated photodiode [38]

2.4.3.3 Waveguide Photodiode

The next photodiode under study is known as the edge illuminated or waveguide photodiode (WGPD). This detector is displayed in Figure 2.27.

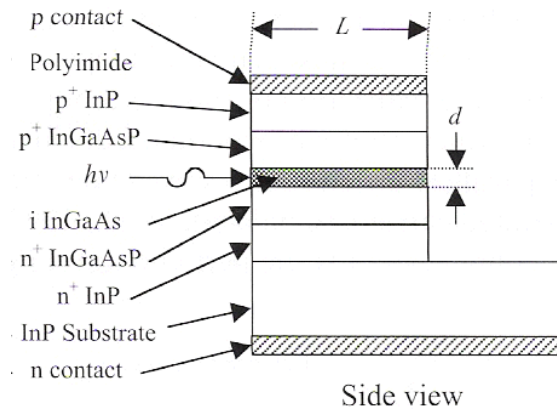


Figure 2.27: Vertical illuminated photodiode (b) Waveguide photodiode [38]

In this case, the photons are sent through the edge of the device. The photons then move into a waveguide region where an active layer is sandwiched between two transparently doped intermediate bandgap layers, creating a double-core multimode waveguide. The active layer is a thin layer of material (thickness of d) that is very long in structure (length of L). Absorption occurs as the light moves down the waveguide. Because the electrical signal

created by absorption still moves vertically through the thin active layer, drift transit times are very low allowing for high bandwidths [39]. Furthermore, because light can be absorbed through the length of the waveguide, quantum efficiency increases. In fact, this causes the two main parameters, bandwidth and quantum efficiency, to be strictly independent of each other. Efficiency is determined by the length of the waveguide (αL), while bandwidth is determined by the depth. Neither is interrelated, as was the problem with vertically illuminated photodiodes [6].

Although the WGPD solved the major problem of the vertically illuminated photodiodes, it still has limitations. Bandwidth of the WGPD is again limited by the RC time constant. This is shown below in the equation below.

$$f_{3dB} = \frac{f_t}{\sqrt{1 + \left(\frac{f_t}{f_{CR}}\right)^2}} = \frac{f_{CR}}{\sqrt{1 + \left(\frac{f_{CR}}{f_t}\right)^2}} \quad (2.52)$$

$$f_{CR} = \frac{1}{2\pi C(R_S + R_L)} \quad (2.53)$$

Mathematically, it is shown that the bandwidth is controlled by f_{CR} , when this value is smaller than f_t . Thus, the goal here is to decrease C to its lowest value to get the highest overall bandwidth. However, this creates a tradeoff for the WGPD. As C decreases, R_S tends to increase, offsetting any improvement the decrease in capacitance brought about [39].

To solve the problem of this tradeoff between the device resistance and capacitance, a new structure was used in fabricating the WGPD. This structure is known as the mushroom-mesa structure (Figure 2.28) [38]. Here, the sandwiched layers above and below the active layer are made wider than the active region. This allows for both a small capacitance and a small device resistance. Therefore, this new design maximizes the bandwidth of the WGPD.

In real life applications, an obtainable bandwidth-efficiency product is somewhere in the range of 70-90 GHz [39].

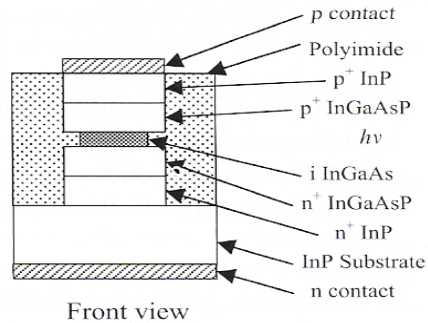


Figure 2.28: Mushroom-mesa waveguide photodiode [38].

The bandwidth-efficiency product of the double-core multimode mushroom-mesa waveguide photodiode can now be compared to that of the double-pass vertically illuminated photodiode. This comparison was done graphically by Kato and is reproduced below.

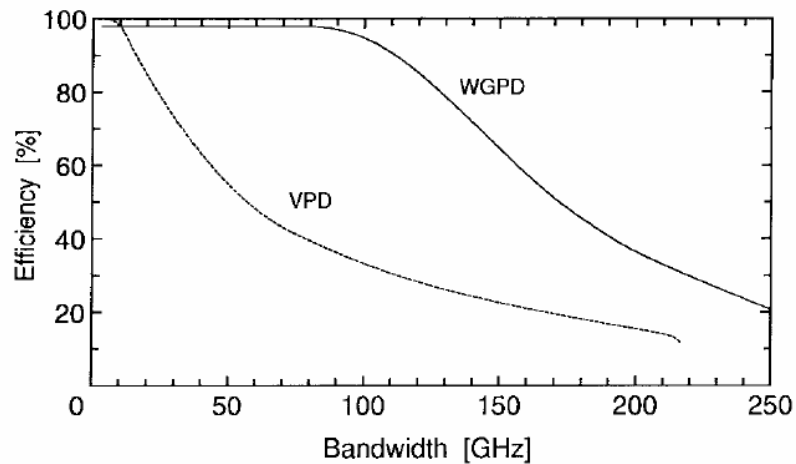


Figure 2.29: Bandwidth versus quantum efficiency for the vertically illuminated photodiode and waveguide photodiode [39].

As this plot shows, for low bandwidths, both the vertically illuminated photodiode and the WGPD have similar high efficiencies. However, as bandwidth increases, the efficiency of the vertically illuminated photodiode drops off dramatically. This is due to the

bandwidth-efficiency tradeoff as previously discussed. The WGPD has a constant high efficiency for bandwidths up to approximately 90 GHz. At larger than 90 GHz bandwidths, the efficiency of the device begins to drop off due to the tradeoff between capacitance and quantum efficiency.

2.4.3.4 Distributed Photodiode and Avalanche Photodiode

Although suitable photodiodes have been discussed, two other photo detector options are worth mentioning – the distributed photodiode and the avalanche photodiode. The distributed photodiode aims to reduce the RC limitation found in the WGPD by distributing the capacitance through an electrical transmission line. The transmission line is terminated with matching impedances effectively allowing bandwidth to be independent of capacitance. Two types of distributed photodiodes have been researched – the traveling-wave photodiode (TWPD) and the periodic TWPD (P-TWPD) structure. In the TWPD case absorption of light occurs down the length of an optical waveguide which is parallel to an electrical transmission line. In the P-TWPD, light is absorbed by a periodic set of photodiodes intermediately distributed within an optical waveguide, which is parallel to an electrical transmission line. In both distributed photodiodes, the bandwidth is limited by the mismatch between the phases of the optical and electrical waves. Matching these phases can dramatically increase the bandwidth of the photodiode. This is seen in equation 2.54.

$$f_{3dB} = \frac{f_t}{\sqrt{1 + \left(\frac{f_t}{f_{PM}}\right)^2}} \quad (2.54)$$

where f_{PM} is the bandwidth limit due to optical-electrical phase mismatch [39]. Distributed photodiodes have been reported with a bandwidth of 78 GHz with an internal efficiency of 0.55 [21].

The final photodiode mentioned is the avalanche photodiode. This photodiode generates a multitude of electrons for the absorption of one photon. This process is known as avalanche multiplication. The gain of the APD can be quite high and even reach infinity during avalanche breakdown. However, bandwidth is limited in the APD by the multiple transit times of carriers generated during the gain process [36].

2.4.4 The Front-End Amplifier

The main function of the front-end amplifier is to amplify the electrical signal output from the photodiode to a usable level. This amplifier should be designed for low noise, good transient behavior, high bandwidth, high gain, and a flat gain response. Front-end amplifiers can be split up into two major types – the high impedance amplifier and the transimpedance amplifier. Both types can be designed in a variety of technologies including, but not limited to field effect transistors (FETs), high electron mobility transistors (HEMTs), heterojunction bipolar transistors (HBTs), and double heterojunction bipolar transistors (DHBTs). Furthermore, both types of amplifiers are available in a multitude of circuit topologies (single ended, cascade, common emitter, fully differential, bootstrapped, etc.). Finally, front-end amplifiers can be discrete to the photodiode, meaning they are not fabricated on the same chip, or monolithically integrated with the photodiode.

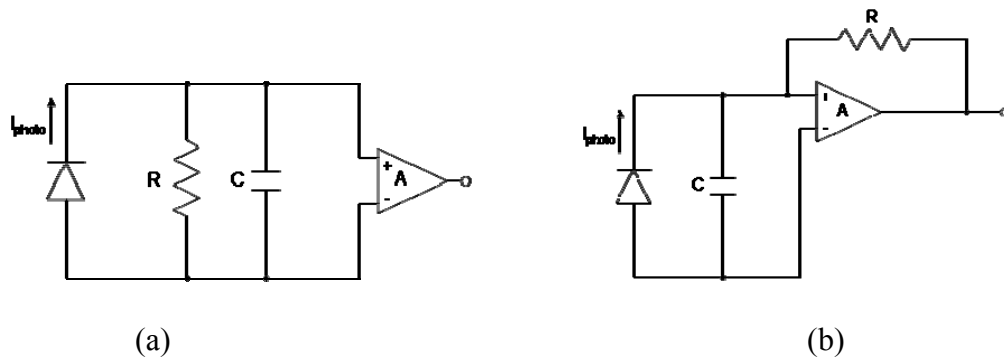


Figure 2.30: (a) Simple high-impedance front-end amplifier (b) Simple transimpedance front-end amplifier [72].

Figure 2.30 illustrates the two most basic front-end amplifier types – the high-impedance and transimpedance amplifiers. In these figures, C and R are defined as follows.

$$C = C_{PD} + C_{IN,amp} + C_{parasitics} \quad (2.55)$$

$$R = R_{IN,amp} \quad (2.56)$$

where C_{PD} , $C_{IN,amp}$, and $C_{parasitics}$ are the photodiode, amplifier input, and parasitic capacitances, respectively. $R_{IN,amp}$ is the amplifier input resistances. One more term can be introduced as $R_{photo,out}$. This term is the load resistance seen by the photodiode. R_{photo} is different for the transimpedance and high impedance cases.

$$R_{photo} = R \quad : \text{high impedance amplifier} \quad (2.57)$$

$$R_{photo} = \frac{R}{A+1} \quad : \text{transimpedance amplifier} \quad (2.58)$$

It will be shown in chapter 3 that the bandwidth of the photodiode is inversely proportional to the photodiode output resistance, R_{photo} , and capacitance, C. Therefore, using Figure 2.30 and the equations for R_{photo} , it is easy to see why the transimpedance amplifier is a better choice for a high speed front-end amplifier design. For the same amplifier impedance, R and C, the transimpedance amplifier has a (A+1) improvement in photodiode bandwidth over the high impedance amplifier.

This same bandwidth relation (bandwidth inversely proportional to R, C) can be used to justify the use of monolithically integrated receivers over discrete receivers. Monolithically integrated receivers eliminate the need for long bond wires and pad capacitances between the photodiode and front-end amplifier. This reduces the overall capacitance of the receiver, C, by reducing the parasitic capacitance, $C_{parasitics}$, found in wire

bonding and contact pads [10]. The reduction of these parasitics is a major focus of results presented in chapter 4 between the discrete and monolithically integrated final designs.

In addition to choosing between transimpedance or high impedance and discrete or monolithic, a choice exists between amplifier topologies and the technology used to implement the topology. Amplifier topology examples are given in Section 2.4.5. When dealing with technologies (HEMT, HBT, DHBT, FET, etc.), two figures of merit exist – f_t and f_{max} . f_t is defined as the transition frequency or frequency at which the current gain equals one. f_{max} is the maximum oscillation frequency. Because it is generally preferred that f_t and f_{max} are four times larger than the bit rate of the optical communication system, not all technologies are compatible with high bit rates [36]. Figure 2.31 plots device transition frequency versus amplifier bandwidth. For a 50 GHz transimpedance amplifier with a gain of 8-dB, a minimum 160 GHz device is needed [85]. For higher gain amplifiers, transition frequencies needed would be higher than 300 GHz [36].

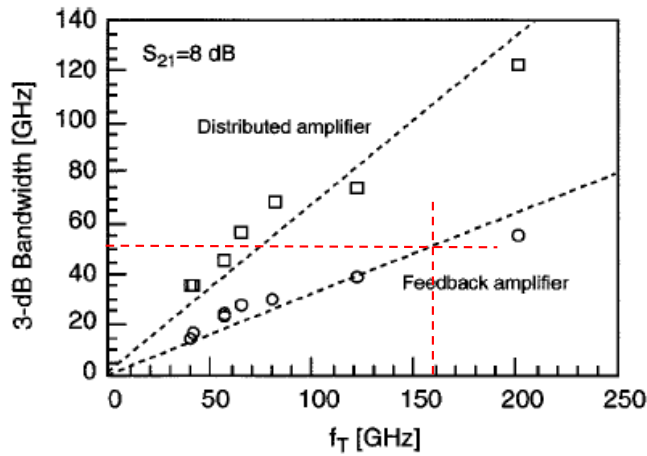


Figure 2.31: Advanced technologies available for high optical communication bit rates [85]

Now that front-end amplifier types and the implementation technologies have been discussed, the next step is to present some examples of quality front-end amplifiers. Section 2.4.5 provides a brief view of some amplifiers using the technologies described above.

2.4.5 Front-End Amplifier Examples

This section gives a very brief overview of some front-end amplifier topologies used for optical communications. It is by no means complete, as an infinite number of topologies exist. Along with each topology, there is a description of amplifier type, modulation format capability, bandwidth, gain, technology, and integration capability. It is very important to note that most of these topologies cannot be directly compared to each other because they use different technologies with a different f_t and f_{max} . The purpose here is just to illustrate the many innovative designs used for the front-end amplifier. The amplifiers are split up into three sections – single ended discrete TIAs, differential discrete TIAs, and monolithically integrated TIAs.

Single ended discrete TIAs

Amplifier #1: Y. Suzuki, et al [83]

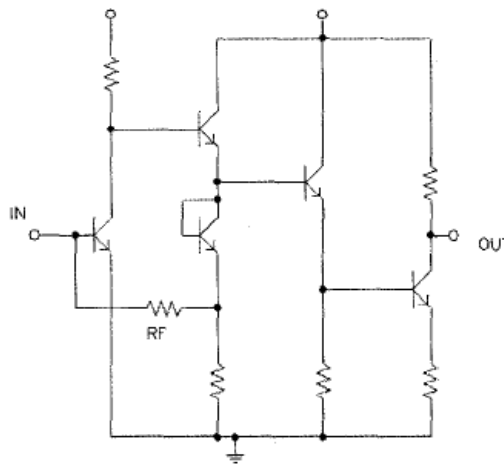


Figure 2.32: Amplifier #1

Type: Single ended TIA
Modulation Format: OOK
Bandwidth / Gain: 34.6 GHz / 41.6 dB Ω
Technology: AlGaAs/InGaAs HBT ($f_t = 96$ GHz, $f_{max} = 240$ GHz)
Integration: Discrete

Amplifier #2: C.Q. Wu, et al [95]

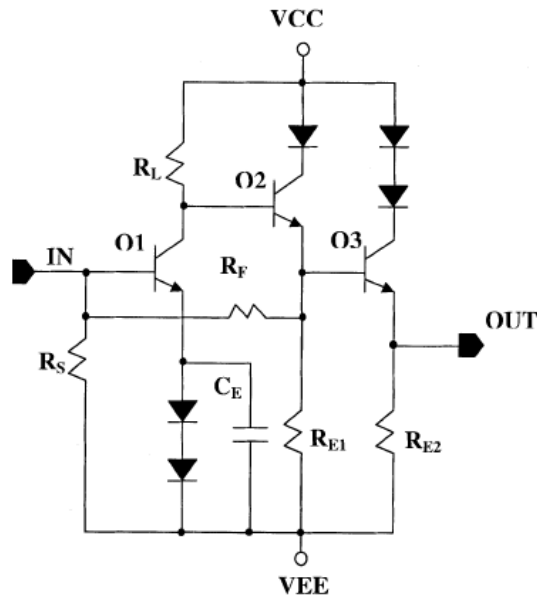
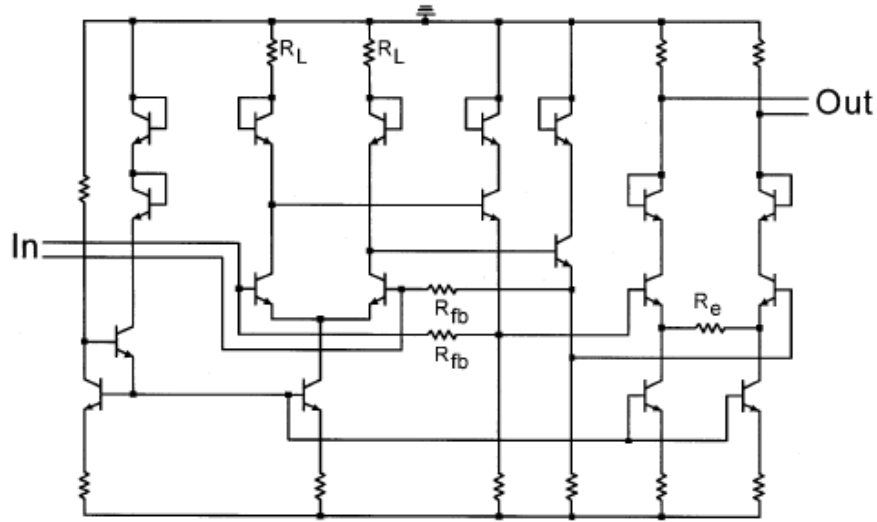


Figure 2.33: Amplifier #2

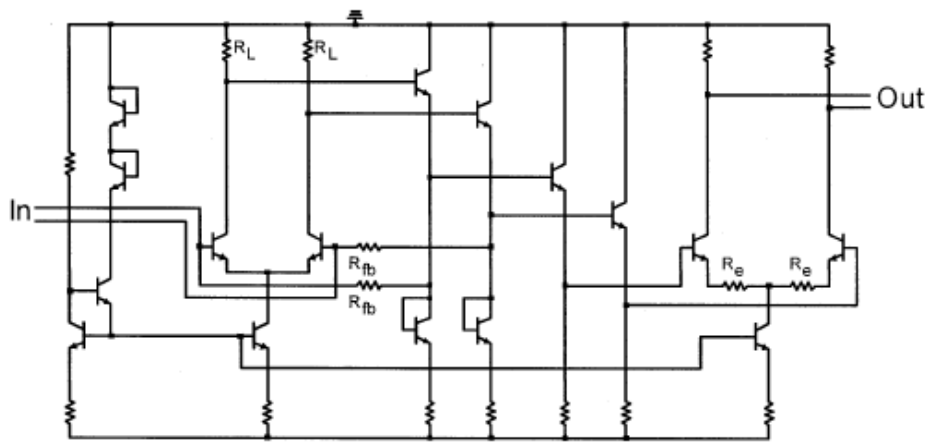
Type: Single ended TIA
Modulation Format: OOK
Bandwidth / Gain: 40 GHz
Technology: InP-InGaAs Single HBT (SHBT) ($f_t = 150$ GHz, $f_{max} = 150$ GHz)
Integration: Discrete

Differential discrete TIAs

Amplifier #3: J. Weiner, et al [91]



(a)



(b)

Figure 2.34: Amplifier #3 (a) SiGe implementation (b) InP Implementation

Type: Differential TIA

Modulation Format: DPSK

Bandwidth / Gain: 50 GHz / 12 dB

Technology: SiGe HBT ($f_t > 200$ GHz)

InP DHBT ($f_t = 170$ GHz, $f_{max} = 140$ GHz)

Integration: Discrete

Monolithically integrated TIAs

Amplifier #4: B. Das, et al [17]

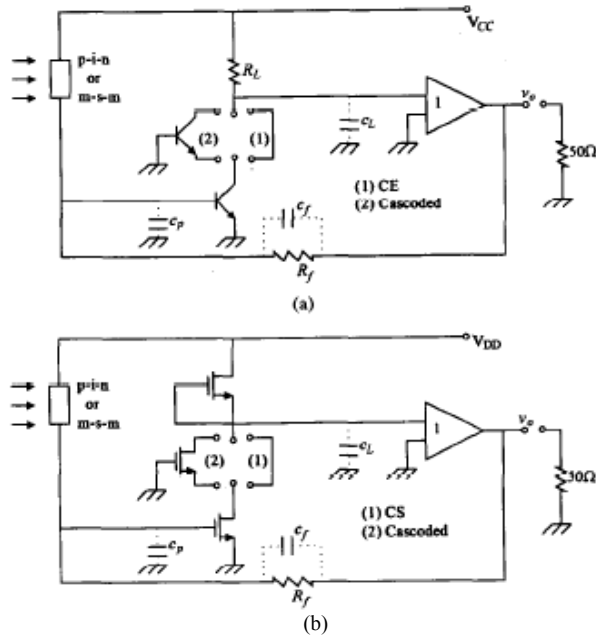


Figure 2.35: Amplifier #4 (a) HBT implementation (b) HFET implementation

Type: Single ended TIA
 Modulation Format: OOK
 Bandwidth / Gain: 20 GHz / 75 dB Ω
 Technology: InGaAs HBT and HFET ($f_t = 160$ GHz)
 Integration: Monolithically integrated

Amplifier #5: L. Lunardi, et al [52]

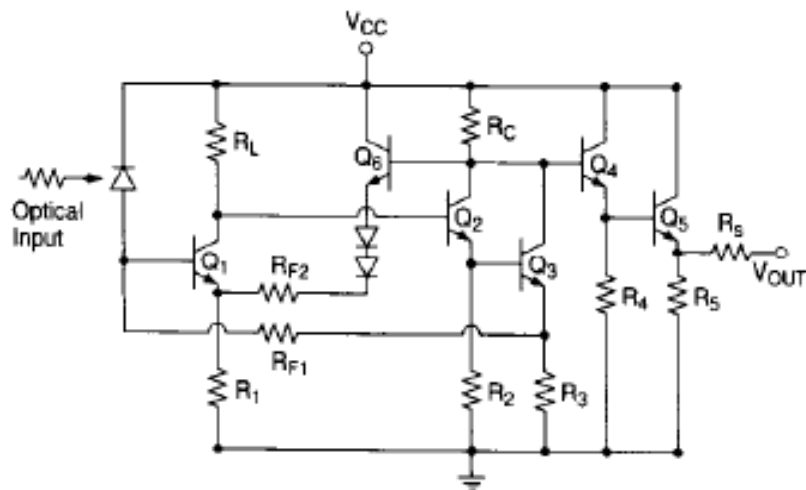


Figure 2.36: Amplifier #5

Type: Single ended TIA
 Modulation Format: OOK
 Bandwidth / Gain: 10 GHz / 5 dB
 Technology: InGaAs HBT ($f_t = 140$ GHz, $f_{max} = 70$ GHz)
 Integration: Monolithically integrated

Amplifier #6: D. Caruth, et al [10]

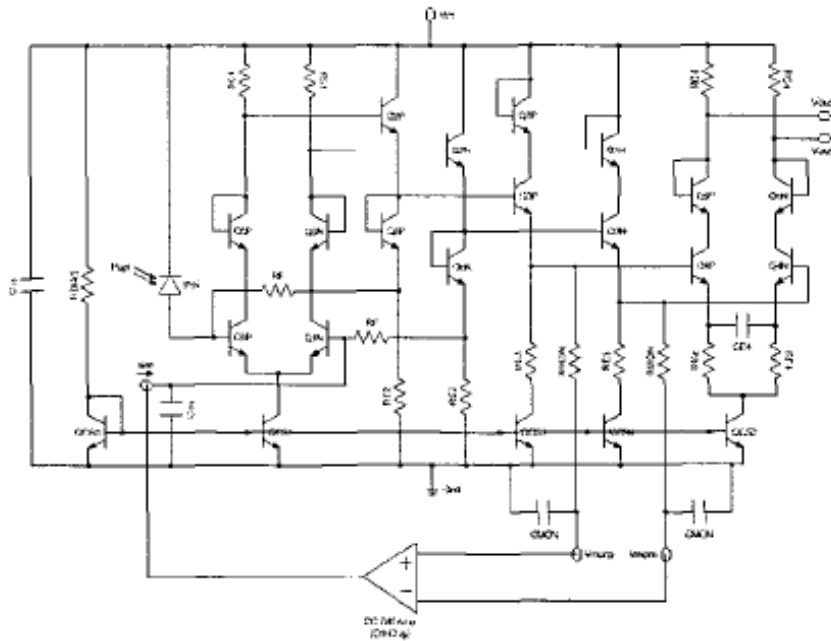


Figure 2.37: Amplifier #6

Type: Single input, differential output TIA
 Modulation Format: OOK
 Bandwidth / Gain: 38 GHz / 145 dB Ω
 Technology: InGaAs SHBT
 Integration: Monolithically integrated

As one can see, there are a variety of possibilities for the implementation of a front-end amplifier. Choices are made on type, integration, technology, and topology. The implementation used depends directly on the application. Main design considerations of the present work are low noise, good transient behavior, high bandwidth, high gain, and a flat gain response.

2.4.6 Differential Phase Shift Keying Receiver

To conclude the overview on the optical receiver, the differential phase shift keying (DPSK) receiver is discussed. As mentioned in section 2.3.2, in DPSK systems, data is encoded by the phase change between adjacent bits. Because standard photo detectors are phase insensitive, the phase modulated signal must first be demodulated into an intensity modulated signal before detection. The 1-bit delay interferometer demodulates the signal and outputs two logically inverted intensity modulated signals. These two signals can then be detected by using a balanced receiver consisting of dual balanced photodiodes and a fully differential TIA. The detailed block diagram of the DPSK receiver is given in Figure 2.38.

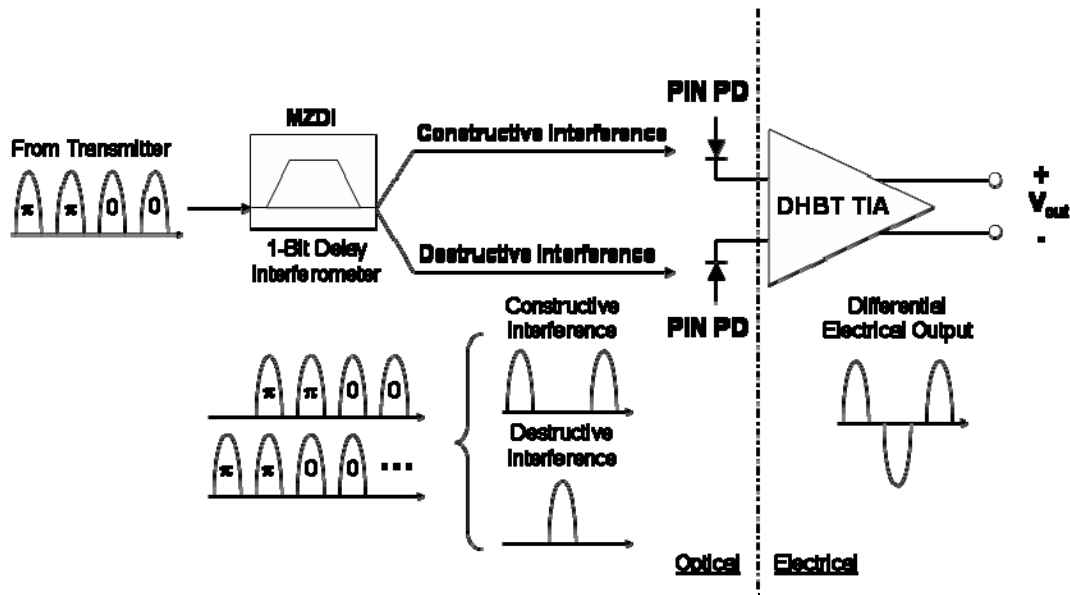


Figure 2.38: Detailed block diagram of DPSK optical receiver

This work focuses on the integrated receiver consisting of photodiodes and the differential TIA. Two possibilities of integration are discrete integration and monolithic integration. In discrete integration, the photodiodes are located off chip from the TIA and are connected by way of electrical bond wires. Figure 2.39 is an illustration of the discrete receiver [81].

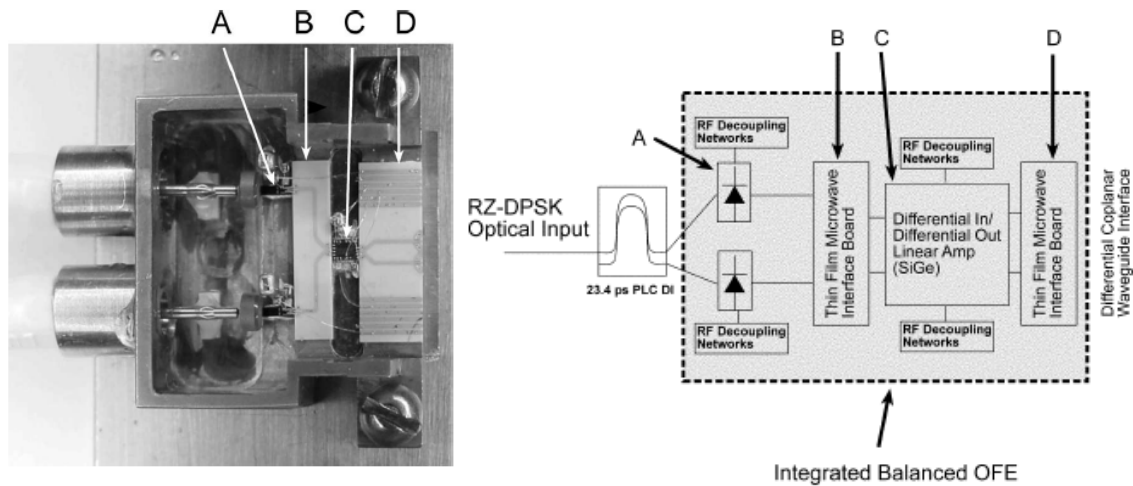


Figure 2.39: Discrete DPSK optical receiver and block outline [81]

In the monolithic integrated design, the photodiodes are located on the same chip as the differential TIA. One such application is illustrated in Figure 2.40 [37].

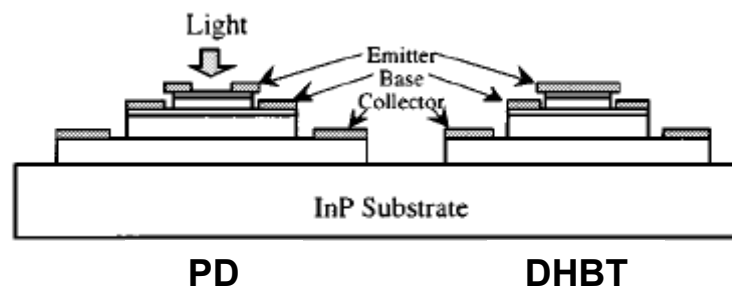


Figure 2.40: Monolithic DPSK optical receiver overview [37]

The monolithic optical receiver can allow for improved receiver performance as the bond wire parasitics are eliminated [37]. Chapter 3 describes in detail the design of both types of receivers, while chapter 4 compares the monolithic optical receiver results to that of the discrete receiver.

3. TRANSIMPEDANCE CIRCUIT DESIGN

3.1 Design Overview

The intent of this thesis is to analyze, design, and simulate a monolithically-integrated InP optical receiver using double balanced PIN-WGPDs and a differential DHBT transimpedance amplifier for DPSK applications over 50 Gb/s. The goals include high amplifier gain with a wide bandwidth, 50Ω impedance matching, smooth transient response, open eye diagrams, a large dynamic range, low power dissipation, low device operating temperature, and low noise operation. The specifications of this project are listed below in Table 3.1.

Table 3.1: Optical receiver specification table

Parameter	Units	Specification
Low Frequency Gain (S21)	dB	10
3-dB Frequency	GHz	50
Unity Gain Frequency	GHz	80
Input Reflection (S11)	dB	-10
Output Reflection (S22)	dB	-10
Differential Transimpedance	dB- Ω	50
Clipped output eye amplitude	V	0.40
Input for clipped output eye	μ A	500
Dynamic Range	dB	20
Power Consumption	mW	600
Supply Voltage	V	5
Device Temperature	$^{\circ}$ C	175
3-dB Noise	pA/ \sqrt{Hz}	100
Technology		InP DHBT / InGaAs PIN WGPD
HBT f_t	GHz	230
HBT f_{max}	GHz	147
Photodiode 3 dB Frequency	GHz	70

In this particular chapter, the design of the integrated receiver is discussed. There are five major sections: double heterojunction bipolar transistor (DHBT) modeling, PIN modeling, TIA topology, differential TIA design, and monolithically-integrated optical

receiver design. Figure 3.1 illustrates the block diagram of the receiver: two balanced WGPDS, a fully differential three-stage DHBT transimpedance amplifier, and a single power supply of 5 V.

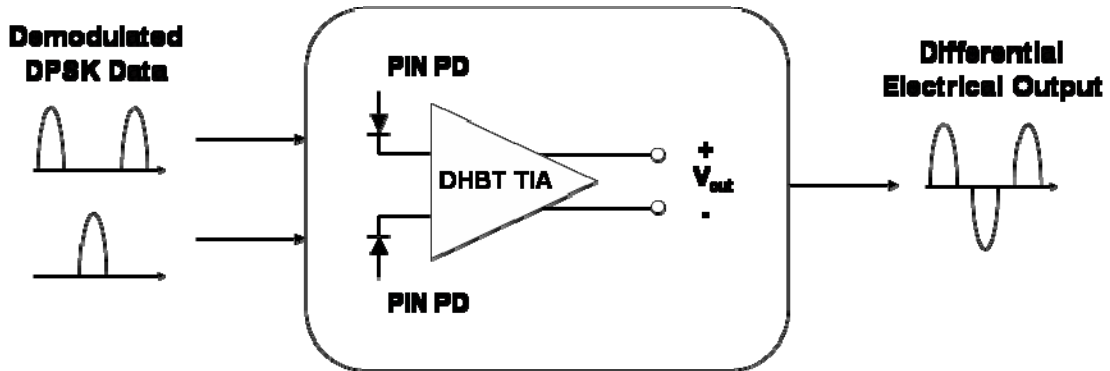


Figure 3.1: DPSK receiver block diagram

The first stage of the transimpedance amplifier was chosen to be a fully differential emitter-coupled amplifier with shunt feedback resistance and a resistive load. This stage converts the input current into an output voltage. The second stage is a buffer stage. Two emitter followers provide isolation between the input and output of the amplifier. Finally, the third stage is a fully differential output stage comprised of another set of emitter-coupled amplifiers which provide gain, high common mode rejection, and matching for a 50 Ω load output.

The InP / InGaAs double heterojunction bipolar transistor (DHBT) has unity current gain cutoff frequency, f_T , of 289 GHz, while the maximum oscillation frequency, f_{max} , is 210 GHz [59]. The InGaAs balanced waveguide photodiodes (WGPDS) have a 3 dB frequency of 70 GHz [88]. Before the transimpedance amplifier can be designed, the DHBT and WGPD models must be defined. This is the goal of sections 3.2-3.3.

3.2 Double Heterojunction Bipolar Transistor Model

This section describes the InP / InGaAs double-heterojunction bipolar transistor (DHBT) model used in the simulation of the optical receiver. The model is a representation of a published DHBT reported in [59]. The published device, based upon a base-metal-overlaid structure (BMOSA) with hexagonal emitter, has an epilayer structure defined in Table 3.2 [59].

Table 3.2: DHBT layer materials [59]

Layer	Material
Emitter Cap	n+ InGaAs / N+ InP
Emitter	N InP
Base	p+ InGaAs
Collector	n+ InGaAs / N InP
Subcollector	N+ InP / n+ InGaAs
Buffer	Undoped InP

Besides the high-speed low-power operation and compatibility for monolithic integration of the photodiodes and front-end amplifier, the InP / InGaAs BMOSA DHBT was chosen because of the over 5 V high breakdown voltage. The hexagonal shape emitter was used to increase separation between the base and emitter in the mesa without the excess side etching commonly found in rectangular shape emitters. A simplified cross section of the device is provided in Figure 3.2. Although [59] presents structures of four different sizes, this thesis models the 180 nm collector, 20 μm^2 hexagonal emitter device.

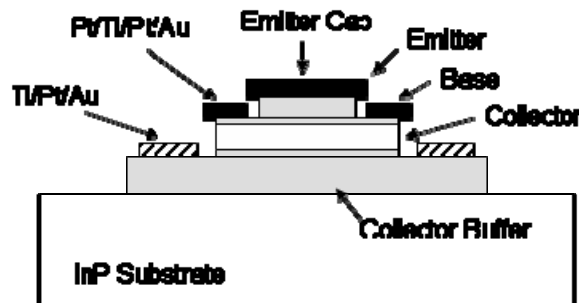


Figure 3.2: DHBT device cross section [59]

The large signal and small signal topologies used to model this DHBT are provided below in Figure 3.3. These models come directly from the Agilent Advanced Design System (ADS) manual, used for all simulations in this thesis. They are based on the Gummel-Poon BJT model, or more specifically the UCSD HBT model [108-109].

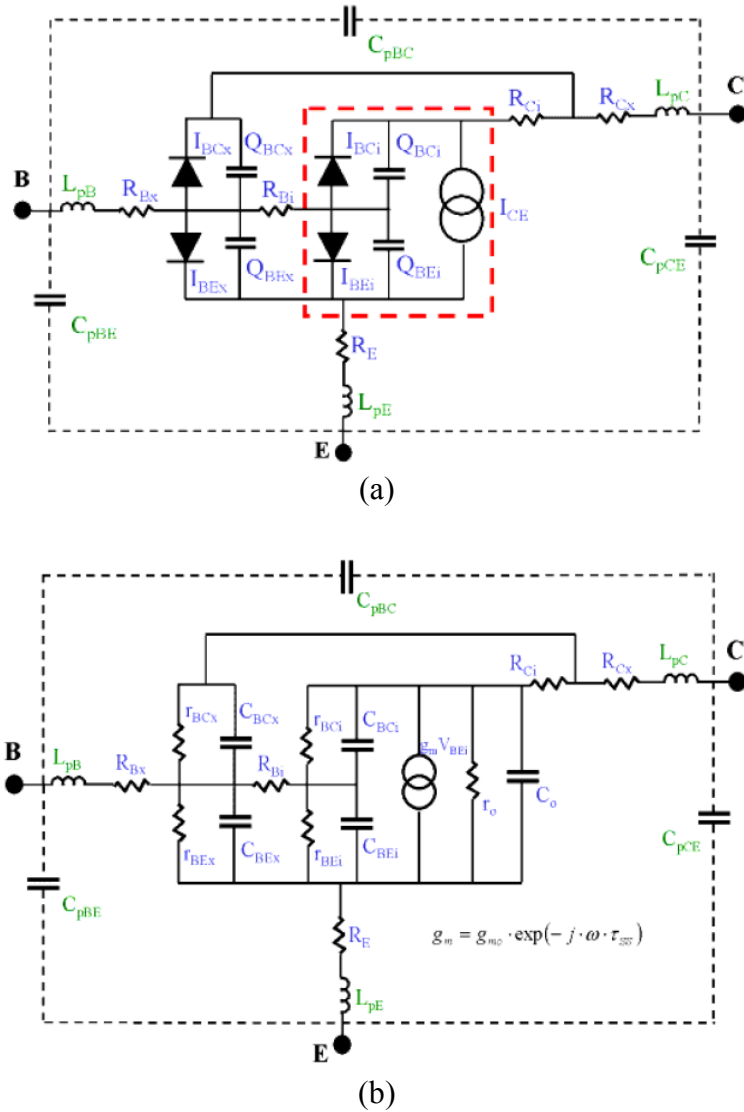


Figure 3.3: DHBT model topologies (a) large signal (b) small signal [109]

Table 3.3 provides a list of the major parameters used for DHBT model simulations in ADS. Initially, the parameters were taken from the extracted small signal model published in [59]. However, because the model in [59] was based on a hybrid pi configuration, the

parameter values had to be modified to fit the Gummel-Poon one. To do this, all parameter values were individually tuned until the model S-parameters fit the measured S-parameters in [59]. For a complete list of the device parameters, refer to Appendix A.

Table 3.3: DHBT model parameters

Name	Description	Units	Value
Re	Emitter resistance	Ω	1.48
Rci	Intrinsic collector resistance	Ω	0.5
Rcx	Extrinsic collector resistance	Ω	0.5
Rbi	Intrinsic base resistance	Ω	19.2
Rbx	Extrinsic base resistance	Ω	8.25
Cje	Base-emitter capacitance (zero bias)	fF	5
Cemax	Base-emitter capacitance (max value in forward bias)	fF	23.7
Cjc	Base-collector capacitance (zero bias)	fF	35
Ccmax	Base-collector capacitance (max value in forward bias)	fF	100
Tfb	Base transit time: delay through the base	psec	0.335
Tfc0	Collector transit time (low current)	psec	0.330
Tcmin	Collector transit time (high current)	psec	0.330
Ege	Effective emitter bandgap parameter	eV	1.34
Egc	Effective collector bandgap parameter	eV	0.8
Ikrk	Kirk effect current value	A	0.04

In addition to the large and small signal models, a self-heating thermal model was implemented in ADS. In real devices, temperature changes with time as electrical energy is converted into heat. Temperature is also altered by diffusion heat transfer and thermal coupling to other devices. These changes in temperature affect the electrical behavior of the device, which in turn, affects the generation of heat. The following self-heating model was used to model these effects.

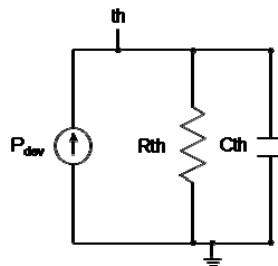


Figure 3.4: DHBT self-heating model [109]

In Figure 3.4, R_{th} is the thermal resistance of the device and C_{th} is the thermal capacitance of the device. These two parameters cause the time-dependent temperature rise previously mentioned. The current source, P_{dev} , is equal to the total dissipated power in the device. Node ‘th’ represents the change in temperature. For the detailed temperature scaling equations that dictate the temperature and electrical behavior relation, please refer to [109]. R_{th} is a function of the material used and the temperature of the device. Table 3.4 displays values of room temperature thermal conductivity for selected materials.

Table 3.4: Thermal conductivities of selected materials [29]

Material	Thermal Conductivity ($Wcm^{-1}K^{-1}$)
InP	0.68
InGaAs	0.048
GaAs	0.54
Si	1.5

The values for R_{th} and C_{th} used in Figure 3.4 were estimated by finding thermal resistances and capacitances of similar structures and similar sizes [15, 29]. Values used for C_{th} and R_{th} are presented below in Table 3.5.

Table 3.5: DHBT self-heating model parameters

Name	Description	Units	Value
R_{th}	Thermal resistance	K/W	2600
C_{th}	Thermal capacitance	nsec-A/V	0.5

Now that the complete model including temperature coefficients has been described, the IV device curves are presented (Figure 3.5). In addition to the IV curves, a temperature profile has also been plotted. Here, the temperature curves were found by using equation 3.1.

$$\Delta T = R_{th}(I_C V_{CE}) \quad (3.1)$$

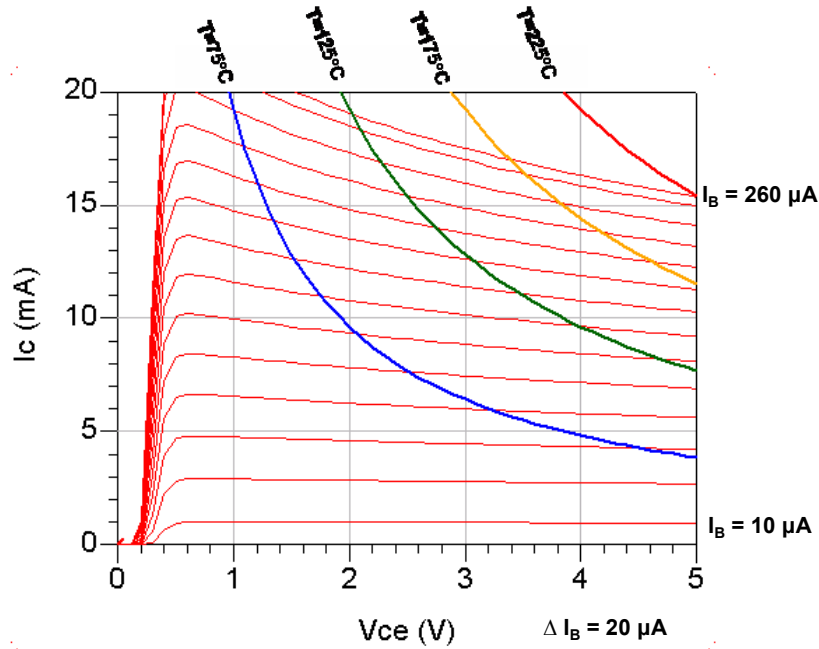


Figure 3.5: DHBT device I-V curves with temperature profile

As previously mentioned, the ADS model parameters were determined by optimizing the model S-parameters to fit the published data [59]. The results of this optimization are provided below in the polar plot of Figure 3.6. As this figure shows, the simulated S-parameters of the DHBT agree well with the measured ones for bias conditions of $V_{CE} = 1.2$ V and $I_C = 20$ mA (same as in [59]). Because [59] did not publish large signal measurements, large signal parameters could not be extracted, and the DHBT model was solely based on the small-signal data. This, in effect, limits the large signal accuracy of the model.

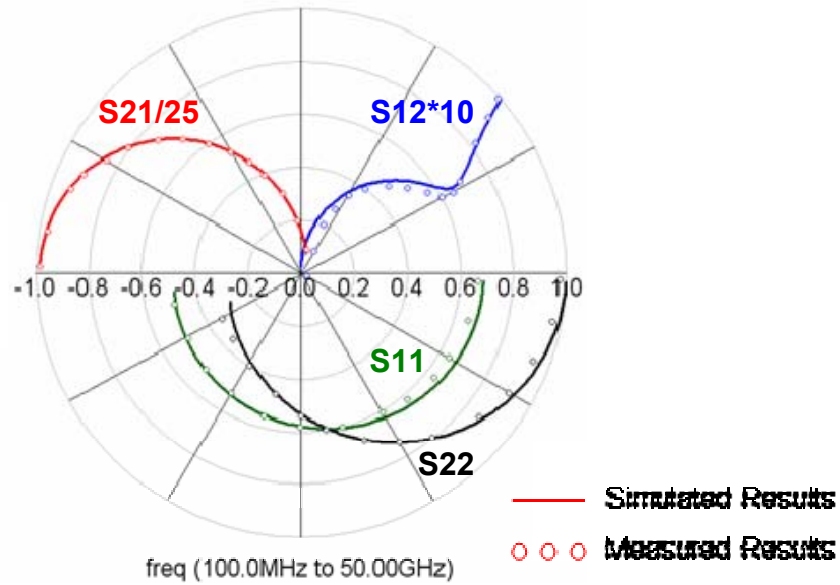


Figure 3.6: S-parameter comparison. Measured data taken from [59]

Figure 3.7 depicts the plot for S21 (here in dB). Again, the simulated results from the DHBT model fit the measured ones over a wide frequency range. The bias conditions were again set to $V_{CE} = 1.2$ V and $I_C = 20$ mA.

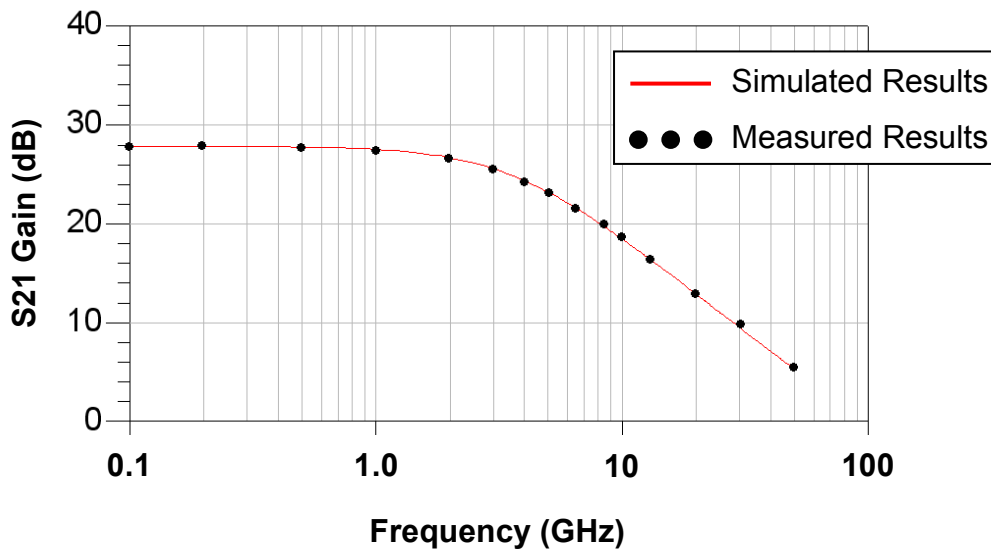


Figure 3.7: S21 comparison. Measured results taken from [59]

After the model for the DHBT was determined, the unity current gain cutoff frequency, f_t , and maximum oscillation frequency, f_{max} , could be found. These two figures of

merit were plotted against collector current below. Again, the simulated results are compared against the measured results. V_{CE} was set to 1.2 V for simulations.

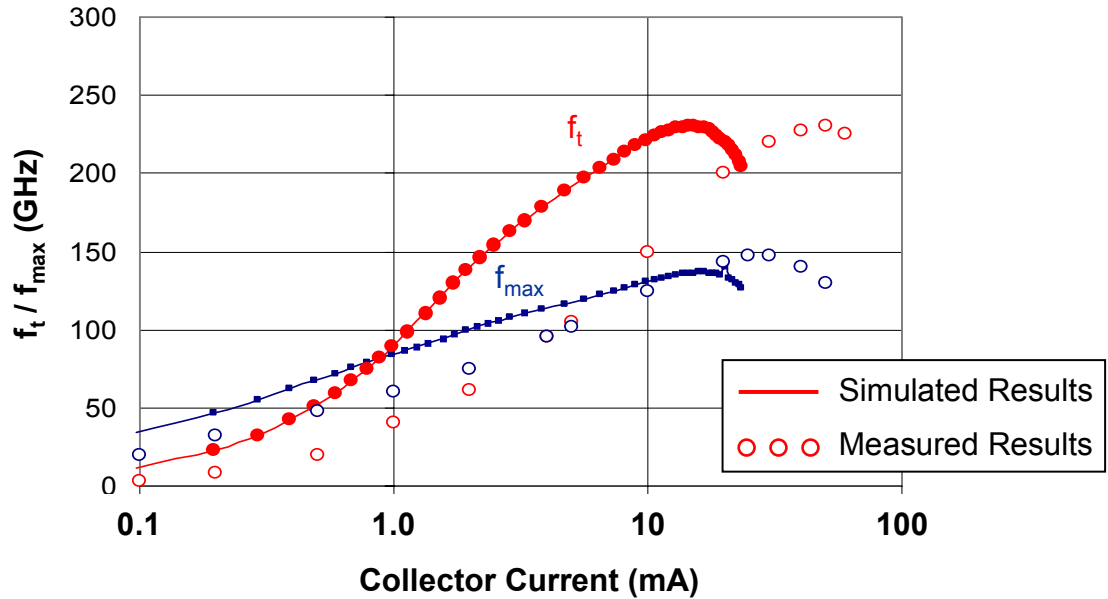


Figure 3.8: f_t and f_{max} of DHBT model. Measured results taken from ($V_{CE} = 1.2$ V) [59]

As Figure 3.8 illustrates, the maximum values of f_t and f_{max} agree with the measured ones but the curves do not align over large signal variations. Again, this is due to the fact that [59] did not publish large signal data from which large signal parameters could be extracted. Overall the quality of the fit of the S-parameter data is considered adequate for circuit design purposes, as long as the difference in the above curves is noted. Table 3.6 compares the simulated data to measured results for f_t and f_{max} .

Table 3.6: f_t and f_{max} comparison between simulated model and measured results [59]

Parameter	Units	Measured Value [59]	Simulated Value	% Difference*
Max f_t	GHz	230.0	230.3	0.13 %
Max f_{max}	GHz	147.0	139.9	4.8 %
Max f_t current	mA	40.0	15.2	62.0 %
Max f_{max} current	mA	22.0	20.1	8.6 %

* % Diff = |(Measured – Simulated)| / Measured * 100%

Preliminary simulations for the receiver indicate that the transistor is not fast enough to achieve the desired gain and bandwidth for the front-end amplifier. As estimated in chapter 2, transition frequencies of approximately 300 GHz are needed for high gain transimpedance amplifiers. Therefore, the model parameters were slightly adjusted to increase f_t and f_{max} of the transistor to accommodate for the 50 GHz amplifier bandwidth. This, in effect, equates to using a faster device. New model parameters are presented in Table 3.7. Those that have been altered are highlighted. Also, new values for f_t and f_{max} are presented in Table 3.8.

Table 3.7: DHBT model parameter listing for new 50 GHz bandwidth appropriate model (see text)

Name	Description	Units	Original Model	Adjusted Model
Re	Emitter resistance	Ω	1.48	1.48
Rci	Intrinsic collector resistance	Ω	0.5	0.5
Rcx	Extrinsic collector resistance	Ω	0.5	0.5
Rbi	Intrinsic base resistance	Ω	19.2	17.2
Rbx	Extrinsic base resistance	Ω	8.25	8.25
Cje	Base-emitter capacitance (zero bias)	fF	5	5
Cemax	Base-emitter capacitance (max value in forward bias)	fF	23.7	23.7
Cjc	Base-collector capacitance (zero bias)	fF	35	22
Ccmax	Base-collector capacitance (max value in forward bias)	fF	100	100
Tfb	Base transit time: delay through the base	psec	0.335	0.235
Tfc0	Collector transit time (low current)	psec	0.330	0.230
Tcmin	Collector transit time (high current)	psec	0.330	0.230
Ege	Effective emitter bandgap parameter	eV	1.34	1.34
Egc	Effective collector bandgap parameter	eV	0.8	0.8
Ikrk	Kirk effect current value	A	0.04	0.04

Table 3.8: f_t and f_{max} listing for new 50 GHz bandwidth appropriate model (see text)

Parameter	Units	Measured Value [59]	Original Model	Adjusted Model
Max f_t	GHz	230.0	230.3	288.6
Max f_{max}	GHz	147.0	139.9	210.0
Max f_t current	mA	40.0	15.2	14.1
Max f_{max} current	mA	22.0	20.1	15.2

Finally, the S-parameters of the newly adjusted model should be compared to the measured results [59]. This will ensure there are no major inconsistencies with the model. The results of the adjusted model are presented in Figure 3.9. To produce the results, V_{CE} was set to 1.2 V and I_C was 20 mA (same as is [59]).

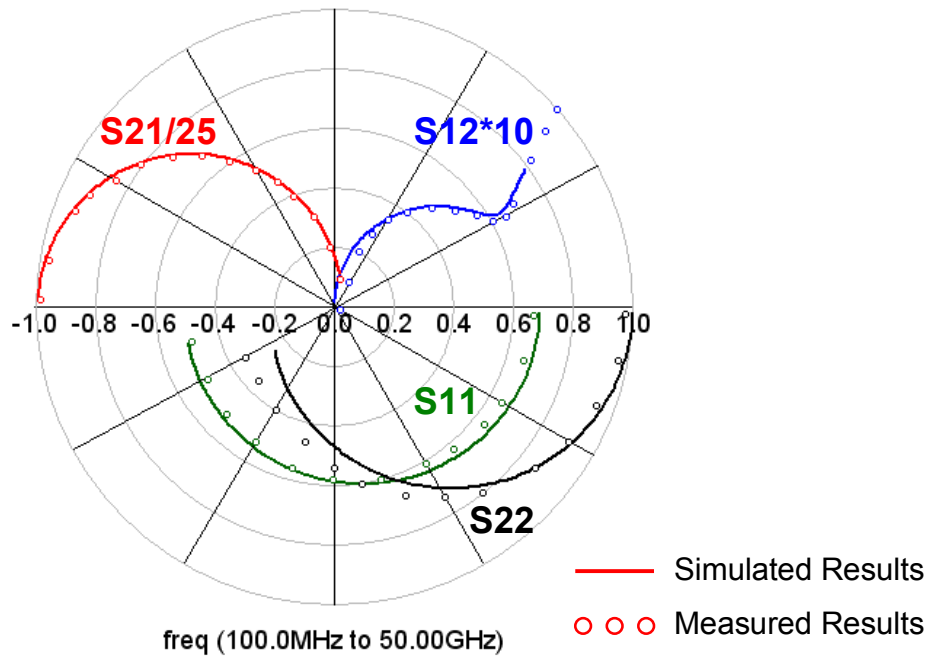


Figure 3.9: S-parameter comparison for adjusted model. Measured results taken from [59]

As this figure shows, the simulated S-parameters of the DHBT match well enough with the measured S-parameters. This agreement again proves that the model used in the receiver simulations represents a realistic device.

3.3 PIN Photodiode Model

This section discusses the InGaAs PIN-WGPD model used in the simulation of the optical receiver. The model is a representation of a published WGPD reported in [88]. The published device consists of an optical waveguide, an evanescently coupled PIN-PD, and a biasing network [88]. The layers of the WGPD are presented in Table 3.9.

Table 3.9: WGPD layer materials

Layer	Material
Waveguide layers	Fe doped InGaAsP ($\lambda = 1.05$ and $1.3 \mu\text{m}$)
N Contact layer	n+ InGaAsP
Intrinsic layer	Undoped InGaAs
P Contact layer	p+ InGaAs

This InGaAs WGPD has a responsivity of 0.37 A/W and bandwidth of 70 GHz, with a 300 nm absorption layer thickness and total area of $5 \times 20 \mu\text{m}^2$. The cross section of the device is shown in Figure 3.10 [88].

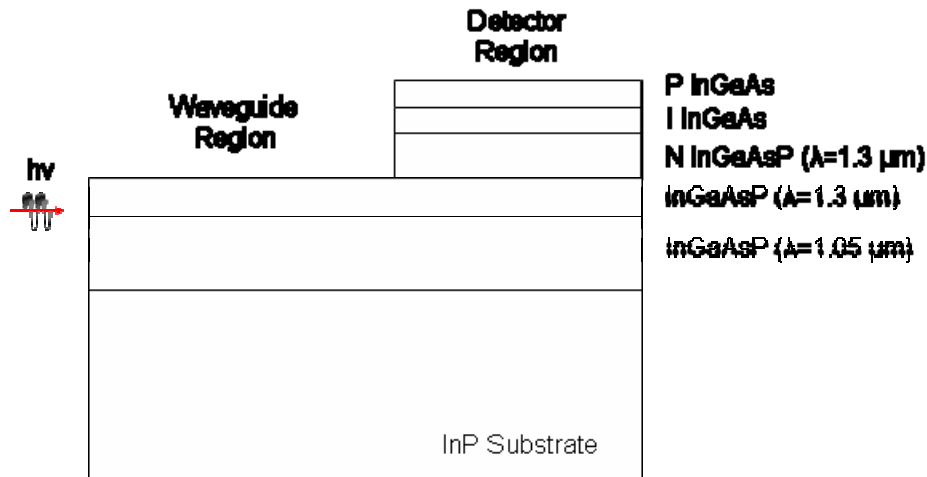


Figure 3.10: WGPD device cross section

The small signal topology used to model the published WGPD is provided below in Figure 3.11, and is a derivation of the model originally found in [88]. Initially, the small

signal parameters were taken from the extracted small signal model published in [88]. To ensure accuracy, all parameter values were individually tuned until the model S-parameters (specifically S21) fit the published ones.

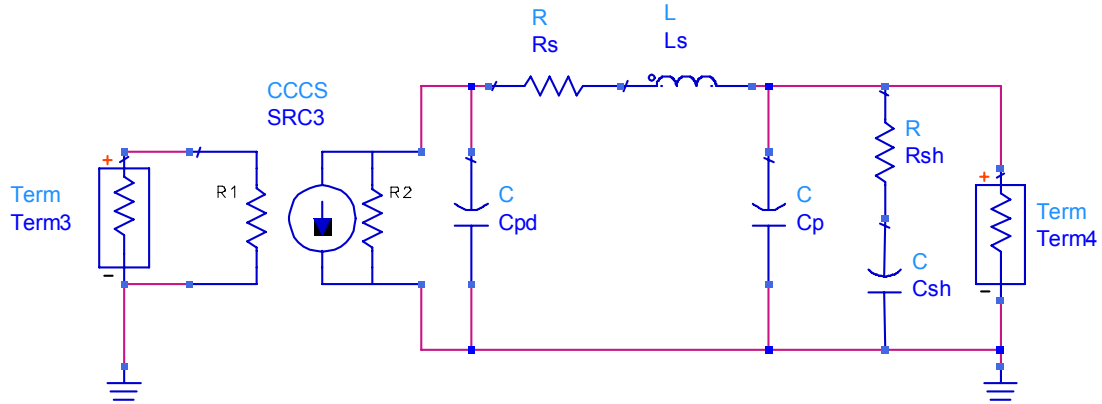


Figure 3.11: WGPD small signal model topology [50]

Table 3.10 lists the parameters used for simulations in ADS for the PIN-WGPD model [88].

Table 3.10: WGPD model parameters

Name	Description	Units	Value
R1	Input matching resistance	Ω	35.5
R2	Internal photodiode parallel resistance	$k\Omega$	2.0
Cpd	Junction capacitance	fF	38.5
Rs	Internal photodiode series resistance	Ω	3
Ls	Internal photodiode inductance	pH	10
Cp	Parasitic capacitance	fF	17
Rsh	Shunt resistance (caused by substrate impurities)	Ω	350
Csh	Shunt capacitance (caused by substrate impurities)	fF	300
Term R	Termination resistors for S-parameter simulation	Ω	50

Figure 3.12 shows the simulated S21 curve of the WGPD plotted with the published results indicating agreement between the two with corresponding 3-dB bandwidths of 70 GHz [88].

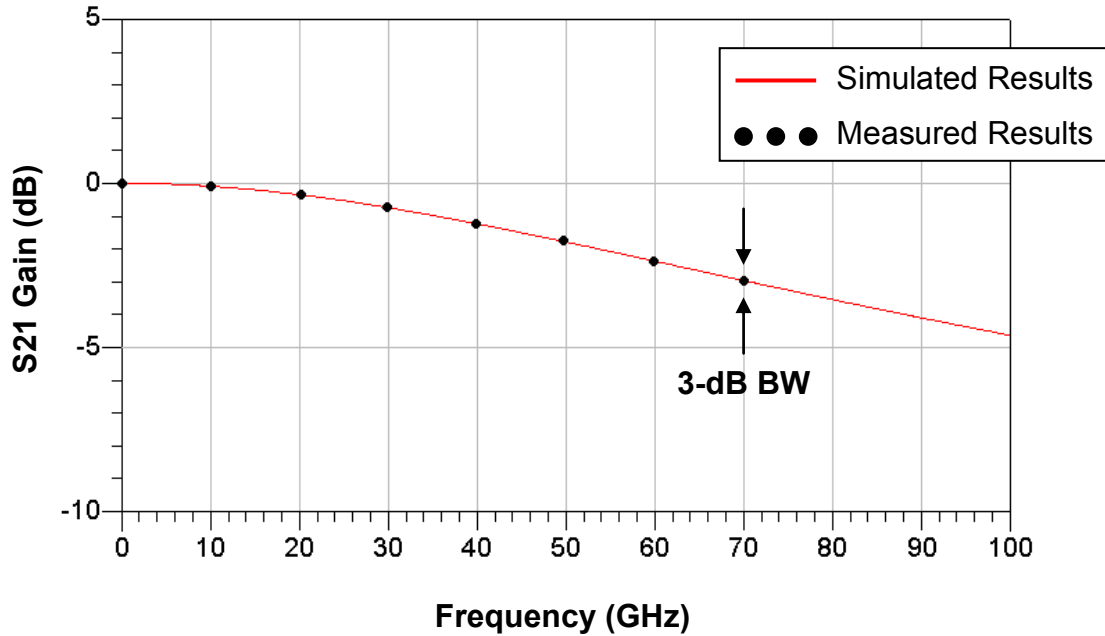


Figure 3.12: S-parameter comparison. Measured results taken from [88]

3.4 Transimpedance Amplifier Topology

With the DHBT and WGPD model parameters determined, the first step for the design of the optical receiver consisted of designing the differential transimpedance amplifier. Once this amplifier was analyzed and simulated, the dual balanced photodiodes were integrated into the simulations. This particular section provides a brief overview of the TIA topology and the complete schematic of the TIA. The optimization process to determine the best design topology is by trial and error. Many topologies were investigated before coming to the best topology for this application.

The schematic of the differential TIA is illustrated in Figure 3.13.

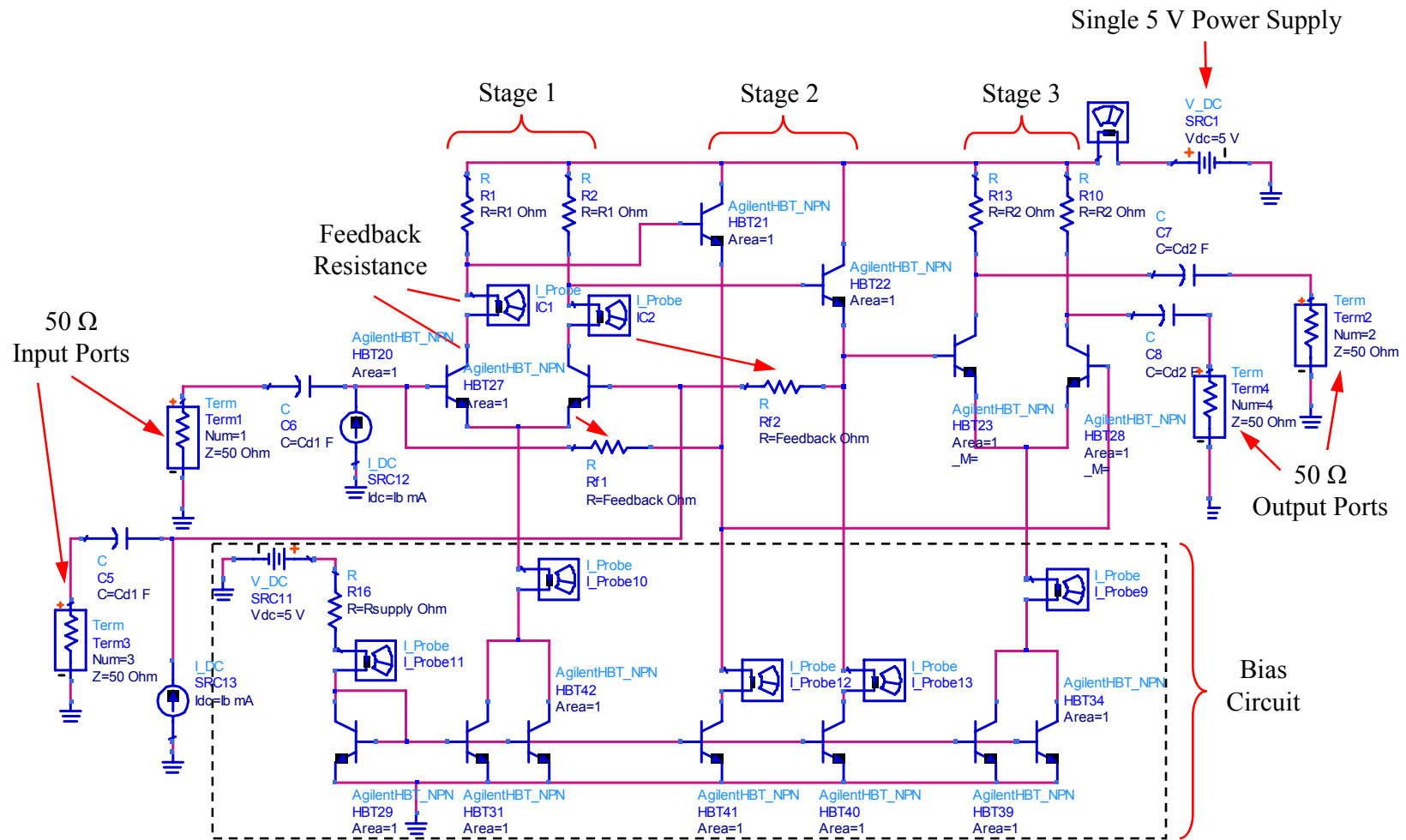


Figure 3.13: Differential transimpedance amplifier topology

The first stage of the transimpedance amplifier was chosen to be a fully differential emitter-coupled amplifier with shunt feedback resistance and a resistive load. Its basic function is to convert the input current into an output voltage. A differential amplifier was chosen for the first stage because it has finite gain with a large output swing. This stage also operates at low noise (due to the inherent low noise characteristics of the DHBTs) if designed properly. The feedback resistance senses the output voltage and returns a proportional current to the input.

The second stage is a buffer stage with two emitter followers providing isolation between the input and output of the amplifier at the cost of higher current. Another tradeoff in using multiple stage amplifiers is that as the number of stages increases, the bandwidth decreases with the extra capacitances and resistances. Thus, it is important that the first stage is designed for wide bandwidth, as the loading of a second and third stage will decrease the overall bandwidth.

The third stage is a fully differential output stage comprised of another set of emitter-coupled amplifiers. This stage further increases the gain of the amplifier and provides for high common mode rejection. It is also considered the matching stage, as the output is matched to a 50Ω load.

Finally, a supply dependent bias scheme based on a single voltage supply of 5 V was implemented to bias all three stages of the amplifier. This scheme could be replaced by a supply independent scheme with start up circuit to further increase the PSRR of the design. From the schematic, the variables have been assigned for critical component values, facilitating the circuit optimization. The following sections in this chapter provide a detailed design for the circuit in Figure 3.13 and investigate the optimized variables.

3.5 Differential Transimpedance Amplifier Design

3.5.1 Design Analysis of the TIA

This section of the thesis details the design analysis of the transimpedance amplifier.

3.5.1.1 Choosing Bias Conditions

The first step in designing the differential TIA is choosing bias conditions for the DHBTs. For this, temperature, transition frequency, and maximum oscillation frequency of the DHBT are taken into account. As one can recall from section 3.2, the maximum f_t of 289 GHz occurred at approximately 14.1 mA and the maximum f_{max} of 210 GHz occurred at 15.2 mA for the adjusted DHBT model. Beyond these collector current densities, the Kirk effect limits the transistor operation [59]. Therefore, to avoid stress, the bias conditions for the DHBTs are chosen to be the lowest as possible as illustrated in Figure 3.14. V_{CE} was set to 1.2 V for simulations.

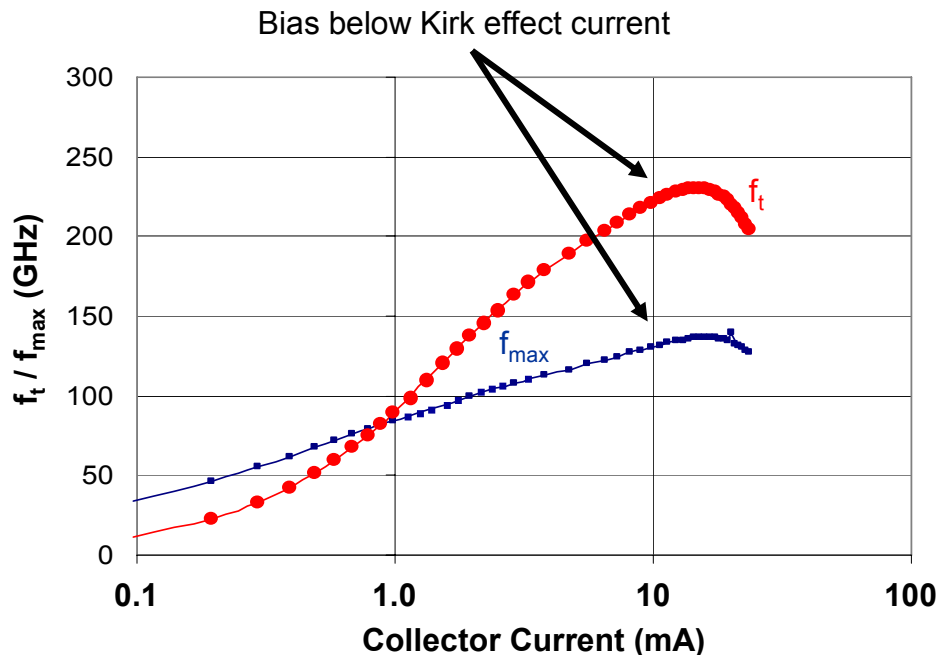


Figure 3.14: f_t / f_{max} curves illustrating proper bias points (note that these curves are the same curves presented Figure 3.8, meaning this is for the original model, not the adjusted model. Adjusted model Kirk effect values are given in above text. $V_{CE} = 1.2$ V)

The devices should also be biased as to limit the device operation temperature. The device temperature can be calculated:

$$T_F = T_I + R_{th}(I_C V_{CE}) \quad (3.2)$$

where T_I and T_F are the initial and final temperatures and R_{th} is the thermal resistance. R_{th} was set to 2600 K/W as described in section 3.2. The temperature goal, as listed in Table 3.1, is less than 175°C. Figure 3.15 illustrates the I-V curves for the adjusted model, indicating bias conditions to the left of the 175°C curve are options for amplifier design.

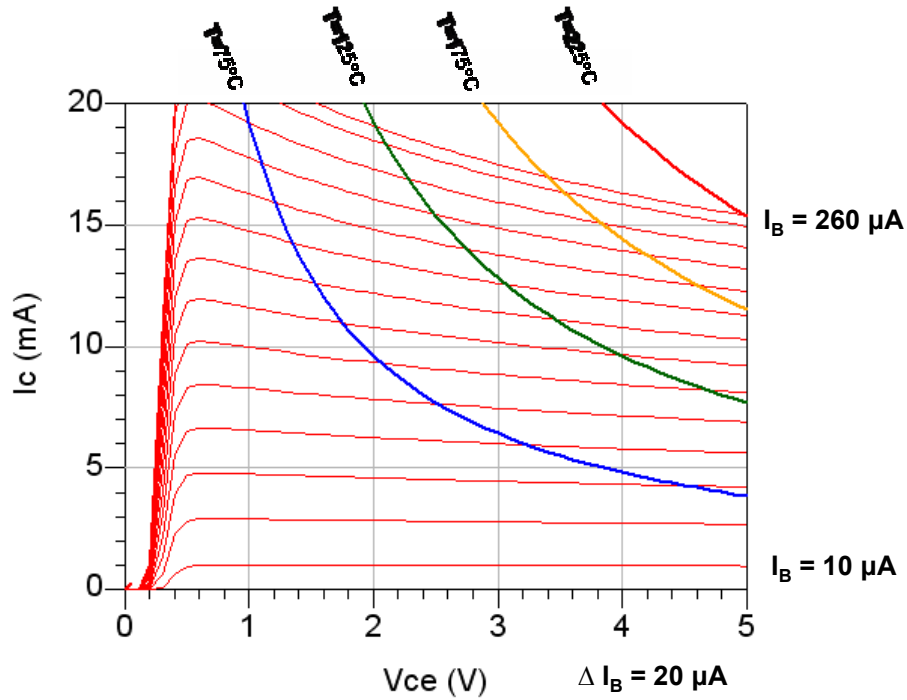


Figure 3.15: DHBT adjusted model I-V curves with temperature profile

From the f_t / f_{max} results and the I-V temperature profiles, the following bias conditions were chosen for optimum amplifier performance, allowing for maximum speed and minimum temperature operation. For simplicity of design, the collector current is the same for all transistors in a single stage, while the collector-emitter voltage varies depending

on the DHBT position in the stack. Therefore, a single I_C value is listed with a range of V_{CE} values for the optimum bias conditions.

Table 3.11: Optimum DHBT bias conditions

Bias Parameter	Units	Value
DHBT Bias Current I_C	mA	13
DHBT Bias Voltage V_{CE}	V	2.0-4.0

The next step of the TIA design is building up the amplifier one stage at a time, as it is important to understand the key aspects of each stage before the whole amplifier is optimized. Each stage will be discussed independently with certain design considerations.

3.5.1.2 TIA Design: Stage 1

The first stage of the TIA is the emitter-coupled differential input pair as pictured in Figure 3.16. A differential amplifier was chosen as the first stage because of its high common mode rejection and low noise operation. Since the majority of noise in an amplifier is introduced through the first stage, the differential pair is the best solution. Three major areas will be investigated for this stage – DC transfer characteristics, low frequency gain, and high frequency response [27].

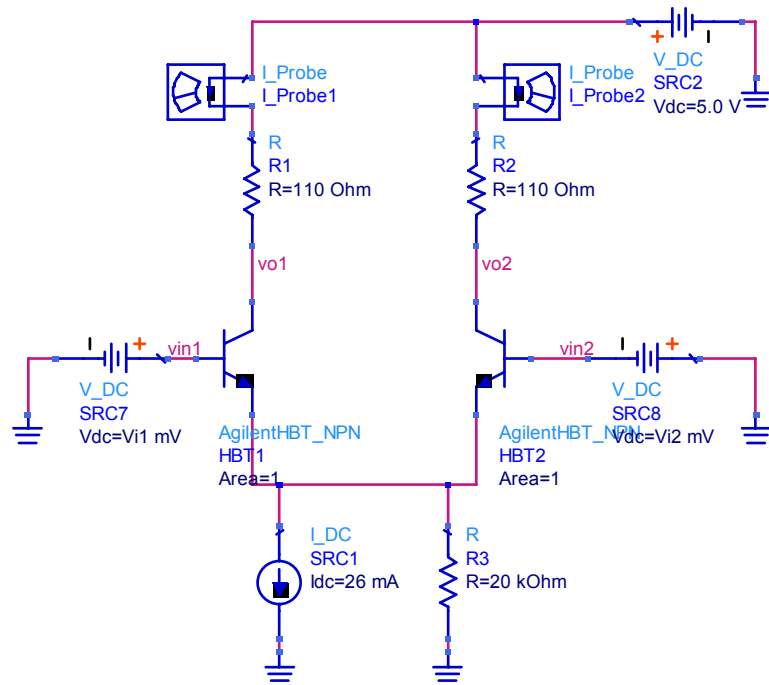


Figure 3.16: Emitter-coupled differential input pair with adjusted DHBT model

Understanding the DC transfer characteristics includes finding the range of input voltages over which the circuit behaves linearly, and determining the differential output voltage as a function of differential input voltage. To find the linear operation, three assumptions were made. First, the amplifier was biased with an ideal current source in parallel with a resistance. The current source was set to 26 mA to satisfy the bias conditions previously mentioned, while the resistance was set to 20 k Ω to simulate the output resistance of a real current mirror. Other assumptions are that the output resistance of the DHBTs is very large (true for bipolar transistors), and the base input resistance is very small. The linear region of operation is found by taking KVL around the input loop of the input stage.

$$V_{i1} - V_{BE1} + V_{BE2} - V_{i2} = 0 \quad (3.3)$$

V_{BE} can be expressed in terms of current by applying the Ebers-Moll equations.

$$V_{BE1} = V_T \ln\left(\frac{I_{C1}}{I_{S1}}\right) \quad (3.4)$$

$$V_{BE2} = V_T \ln\left(\frac{I_{C2}}{I_{S2}}\right) \quad (3.5)$$

where V_T is the thermal voltage and $I_{S1,2}$ are the scaling currents of the devices. Since transistors HBT1 and HBT2 are identical, $I_{S1} = I_{S2}$ and V_{id} is introduced as $V_{i1} - V_{i2}$. Using equations 3.3-3.5, a ratio of collector currents can be determined as:

$$\frac{I_{C1}}{I_{C2}} = \exp\left(\frac{V_{id}}{V_T}\right) \quad (3.6)$$

Using KCL at the emitters will result in:

$$I_{Source} = -(I_{E1} + I_{E2}) = \frac{[I_{C1} + I_{C2}]}{\alpha} \quad (3.7)$$

where $\alpha = \frac{\beta}{1 + \beta}$ (β is the gain of the DHBT). Finally, one can substitute (3.6) into (3.7) to

find the circuit's current behavior as a function of input voltage:

$$I_{C1} = \frac{\alpha I_{Source}}{1 + e^{(-V_{id}/V_T)}} \quad (3.8)$$

$$I_{C2} = \frac{\alpha I_{Source}}{1 + e^{(V_{id}/V_T)}} \quad (3.9)$$

When the differential voltage equals zero, $I_{C1} = I_{C2} = 0.5\alpha I_{Source}$. When the differential voltage is large (greater than $3V_T$), one of the transistors turns off and the entire source current flows through the opposite transistor. To check this relation, the circuit in Figure 3.16 was simulated for a range of differential input voltages. The results are presented in Figure 3.17 indicating that equations 3.8 and 3.9 have been validated. Furthermore, Figure 3.17

illustrates the linear region of operation around $V_{id} = 0$. The circuit behaves linearly to within about $\pm 1.5 \cdot V_T$. The value of current at zero voltage is the bias current of the DHBT (13 mA).

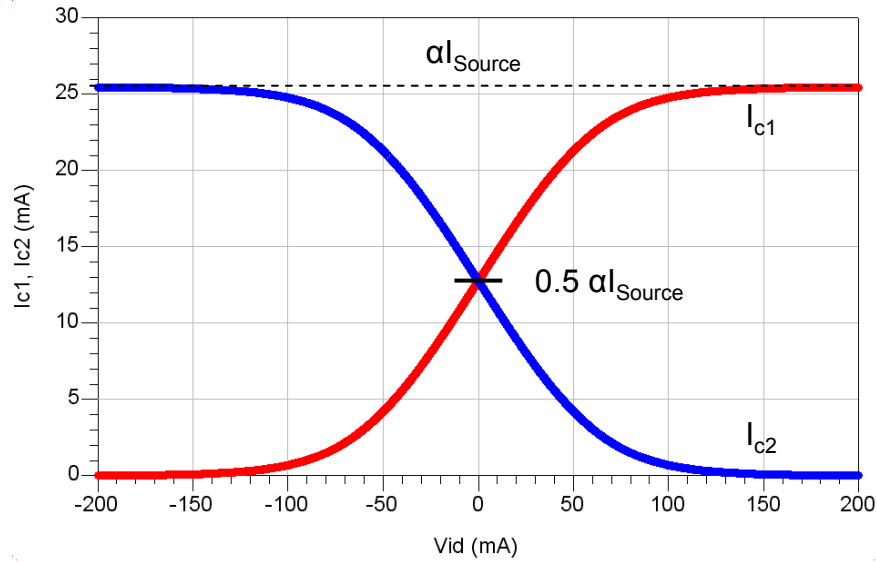


Figure 3.17: Emitter-coupled differential input pair with adjusted DHBT model simulations

For the output voltages, V_{o1} and V_{o2} , again applying KVL at the output of at the circuit in the diagram of Figure 3.16, one obtains:

$$V_{o1} = V_{cc} - I_{c1}R_C \quad (3.10)$$

$$V_{o2} = V_{cc} - I_{c2}R_C \quad (3.11)$$

Substituting equations 3.8-3.9 into 3.10-3.11 and solving for V_{od} gives the following relation.

$$V_{od} = V_{o1} - V_{o2} = \alpha_F I_{Source} R \tanh\left(\frac{-V_{id}}{2V_T}\right) \quad (3.12)$$

where R is the load resistance of the circuit (110 Ω). Equation 3.12 shows that if the differential input voltage is zero, there will be no output voltage, which infers that for direct coupling of amplifier stages, no coupling capacitors are needed. If coupling capacitors were needed, the frequency response of the amplifier would be degraded. The circuit in Figure 3.16 was simulated to validate equation 3.12 and the results are presented in Figure 3.18.

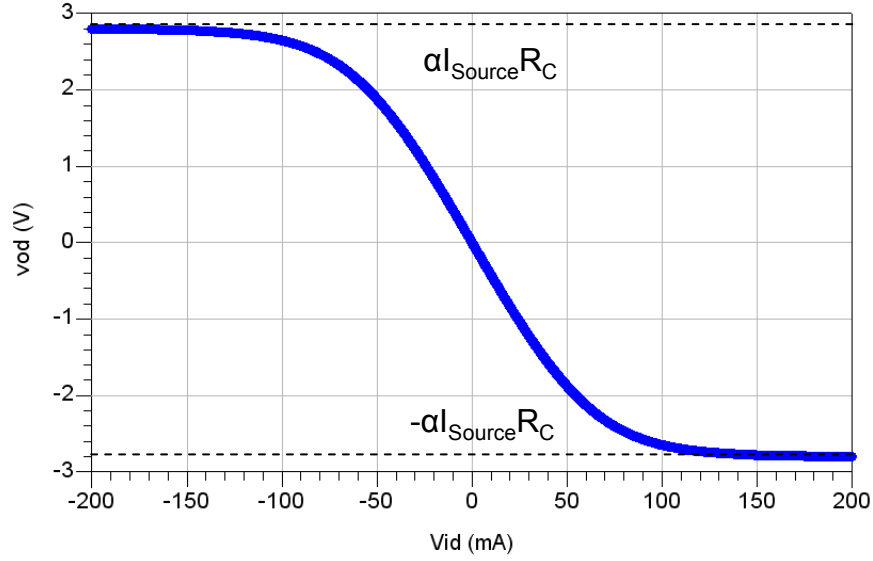


Figure 3.18: Emitter-coupled differential input pair with adjusted DHBT model simulations

The small signal gain of the first stage will be discussed with focus on operation in the linear region of Figure 3.18. Both low and high frequency gain are presented for understanding amplifier parameter design.

Using half circuit analysis, the low frequency small signal differential gain, A_{dm} , of the balanced emitter-coupled differential input pair is found [27].

$$A_{dm} = \left. \frac{v_{od}}{v_{id}} \right|_{v_{ic}=0} = -g_m (R // r_o) = -\frac{I_C}{V_T} (R // r_o) \quad (3.13)$$

where V_{ic} is the common mode input voltage, g_m is the transconductance, R is the load resistance, and r_o is the output resistance of the DHBT. This equation shows that by increasing the bias current or load resistance, gain can be increased. Since bias currents have already been chosen, a large R should be used in the final design. The common mode gain is listed in equation 3.14. Here, R_{source} is the resistance of the current source.

$$A_{cm} = \left. \frac{v_{oc}}{v_{ic}} \right|_{v_{id}=0} = -\frac{g_m (R // r_o)}{1 + 2g_m R_{Source}} \quad (3.14)$$

The common mode rejection ratio (CMRR) indicates how well the amplifier cancels out noise common to both inputs; therefore, it is desirable to have a high CMRR. High CMRR is achieved by having high differential mode gain and low common mode gain.

$$CMRR = \left| \frac{A_{dm}}{A_{cm}} \right| = 1 + 2g_m R_{Source} \quad (3.15)$$

From Equation 3.15, a high CMMR translates to high bias current and high current source resistance [27].

The high frequency gain of the balanced emitter-coupled differential input pair is also detailed in [27] using half circuit analysis. Equation 3.16 is the differential mode gain term. Furthermore, equation 3.17 and 3.18 indicate the dominate pole and non-dominate pole of this stage, respectively. Here, R_S is the input source resistance, r_b and r_π are device resistances, all C values are device capacitances and $R_p = (R_S + r_b) // r_\pi$.

$$\frac{v_o}{v_i} = - \frac{\frac{g_m R R_p \left(1 - s \frac{C_\mu}{g_m} \right)}{R_S + r_b}}{1 + s(C_\mu R + C_\mu R_p + C_\pi R_p + g_m R R_p C_\mu) + s^2 R R_p C_\mu C_\pi} \quad (3.16)$$

$$p_1 = - \frac{1}{[(R_S + r_b) // r_\pi] \left[C_\pi + C_\mu \left(1 + g_m R_L + \frac{R}{R_p} \right) \right]} \quad (3.17)$$

$$p_2 = - \left(\frac{1}{R C_\mu} + \frac{1}{R_p C_\pi} + \frac{1}{R C_\pi} + \frac{g_m}{C_\pi} \right) \quad (3.18)$$

The last three equations indicate that the analysis becomes more complex at high frequencies. A simple observation is made in that to have a wide bandwidth (large p_1 , p_2), bias current and resistance should be minimized. This observation indicates that there is a direct tradeoff

between gain and bandwidth. This tradeoff will be further investigated when all three stages are integrated.

3.5.1.3 TIA Design: Stage 2

The second stage of the transimpedance amplifier is the emitter follower stage. In this stage, two emitter followers provide isolation between the input and output of the amplifier. This buffer comes at the cost of lowering bandwidth as the emitter follower stage adds in extra capacitances and resistances. Figure 3.19 depicts one of two emitter followers biased by an ideal current source. The emitter follower will be studied based upon its gain and high frequency response. The following discussions on this topic follow Gray, Hurst, and Meyer's discussion in [27].

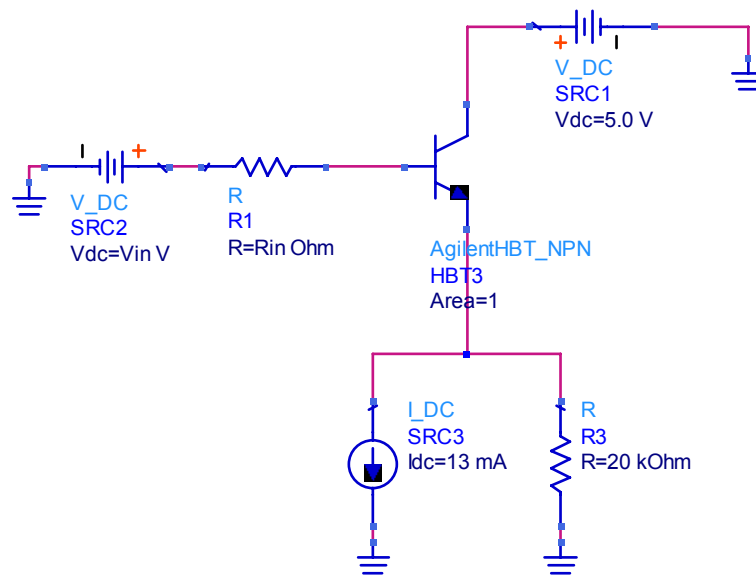


Figure 3.19: Emitter follower with adjusted DHBT model

The low frequency small signal gain of the emitter follower is listed below.

$$A_v = \frac{v_o}{v_i} = \frac{1}{1 + \frac{R_{in} + r_\pi}{(\beta + 1)(R_{Source} // r_o)}} \quad (3.19)$$

Here, R_{in} is the input resistance to the emitter follower which is determined by the first stage differential pair. This equation shows that the gain of an emitter follower is always less than one. If $(\beta + 1)(R_{Source} // r_o)$ is much greater than $R_{in} + r_\pi$, the gain then approaches one. This is the case for the TIA under study. The high frequency response is provided by the following equation.

$$A_v = \frac{v_o}{v_i} = \frac{g_m R_{Source} + \frac{R_{Source}}{r_\pi}}{1 + g_m R_{Source} + \frac{R'_S + R_{Source}}{r_\pi}} \left[\frac{1 - \frac{s}{z_1}}{1 - \frac{s}{p_1}} \right] \quad (3.20)$$

z_1 and p_1 are the zero and pole of the transfer function, respectively. They are provided in equations 3.21-3.22.

$$z_1 = -\frac{g_m + \frac{1}{r_\pi}}{C_\pi} \quad (3.21)$$

$$p_1 = -\frac{1}{C_\pi R_1} \quad (3.22)$$

where,

$$R_1 = r_\pi // \frac{R'_S + R_{Source}}{1 + g_m R_{Source}} \quad (3.23)$$

$$R'_S = R_{in} + r_b \quad (3.24)$$

The zero is usually on the order of the transition frequency of the DHBT. Therefore, it does not play a role in amplifier bandwidth. The pole, however, can decrease the bandwidth of the TIA. Thus, it is important that R_1 is designed to be as small as possible to ensure a high frequency response for this stage.

3.5.1.4 TIA Design: Stage 3

The final stage of the amplifier is a fully differential output stage and is comprised of another emitter-coupled differential pair. Its setup was shown in Figure 3.16. The main design goals of this stage were to ensure enough power was provided to the load with low signal distortion, to match the output impedance to a load impedance of $50\ \Omega$ (equivalent to having a low S_{22}), and to ensure this stage does not limit the frequency response of the entire amplifier.

The DC transfer characteristics, low frequency gain, and high frequency response can be determined as was already performed for the input stage. However, the design goals of the output stage were different than the ones for the input, so different considerations were taken into account. Rather than designing for low noise (as in the case of the input stage), the output stage is designed for high gain and good matching to $50\ \Omega$. Of course, bandwidth remains important for all stages. The load resistance, R_2 , of the output stage was set to $45\ \Omega$ and was determined by optimization while taking the design goals into consideration.

3.5.1.5 Current Mirrors

The current mirror used to bias the transimpedance amplifier is a simple circuit consisting of one diode connected DHBT linked to multiple current-sourcing DHBTs. The current mirror topology is depicted in Figure 3.20. Because stages 1 and 3 require twice the current of stage 2, the mirrors used for stages 1 and 3 consist of two transistors in parallel. Parallel transistors were used rather than a single one twice the size to allow for a lower device temperature operation.

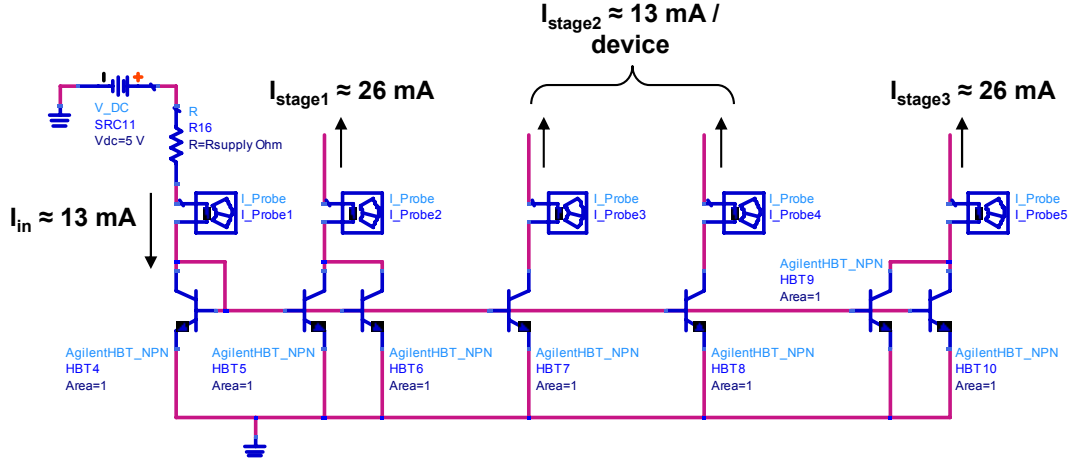


Figure 3.20: Current mirrors used to bias TIA

The output current at any one of the current mirrors is a function of the input current through the diode connected transistor, and this relation is given in equation 3.25 [27]. Here, V_A is the Early voltage of the transistor set by the adjusted DHBT model and I_{IN} and I_{OUT} are the input and output currents of the mirrors, respectively. Also, parameters marked by a ‘1’ indicate they belong to the diode connected transistor, while parameters marked by ‘2’ indicate that they belong to any one of the current sources in Figure 3.20. N is the scaling ratio which is set by the number of transistors ganged together in a particular mirror. Stage 1 and 3 mirrors have ratios of 2, while stage 2 has two mirrors each with a ratio of 1.

$$I_{OUT} = \frac{\frac{NI_{S2}}{I_{S1}} I_{IN} \left(1 + \frac{V_{CE2} - V_{CE1}}{V_A} \right)}{1 + \frac{NI_{S2} / I_{S1}}{\beta}} \quad (3.25)$$

If $V_{CE1} \approx V_{CE2}$ and β is large, this equation can be simplified into equation 3.26.

$$I_{OUT} \approx \frac{NI_{S2}}{I_{S1}} I_{IN} \quad (3.26)$$

Equation 3.26 shows that by choosing an input current and a certain number of parallel devices in a mirror, a specific output current can be achieved. The input current is set by equation 3.27.

$$I_{IN} = \frac{V_{CC} - V_{BE1}}{R_{Supply}} \quad (3.27)$$

As equation 3.27 shows, the input current directly depends on V_{CC} and R_{Supply} . This is just one possibility for biasing the transimpedance amplifier. If V_{CC} and R_{Supply} dependence is not desirable, one could choose to bias the amplifier with a base-emitter reference current source or a self-biased V_{BE} reference with start up circuit [27]. Both of these current sources improve the supply and resistance dependences.

Figure 3.20 indicates the estimated output currents provided by the mirrors for an input current of 13 mA. It should be noted that in practice, I_{IN} had to be increased to guarantee that 26 mA was provided to stages 1 and 3. The cause for this modification is that two devices in parallel do not give a perfect multiple of 2 as equation 3.26 assumed. In doing this, the current in stage 2 was also increased, although this increase was not enough to impair the performance of the TIA.

3.5.1.6 Open Loop Gain

Now that each stage's key design considerations have been highlighted, the open loop gain can be determined. Figure 3.21 provides the open loop simple block diagram for the detailed TIA of Figure 3.13.

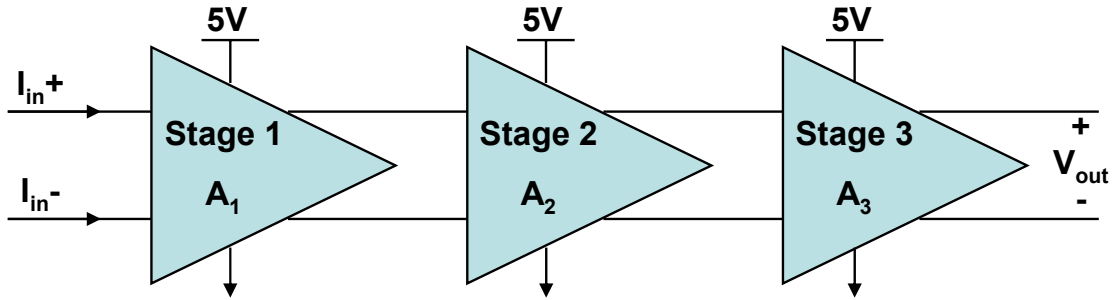


Figure 3.21: Open loop block diagram for 3 stage TIA with single power supply

The low frequency open loop gain of the transimpedance amplifier is the multiplication of the gain of each stage of the amplifier and is given as:

$$A_0 = A_1 A_2 A_3 \approx g_m^2 (R_1 // r_{o1}) (R_2 // r_{o2} // R_{eL}) \quad (3.28)$$

where R_{eL} is the external load resistance of the amplifier and it is assumed that the gain of the emitter follower stage is nearly 1. This relation shows that to increase the open loop gain of the amplifier, either current or resistance of stage 1 and 3 should be increased.

3.5.2 Optimization of the TIA Parameters

The next step in the receiver design is the optimization of the transimpedance amplifier with feedback. Figure 3.22 provides a simple block diagram for the detailed TIA schematic of Figure 3.13.

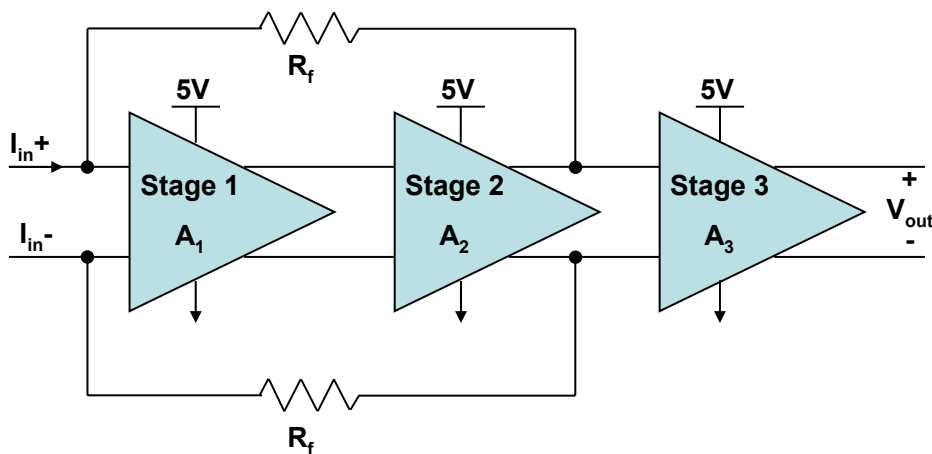


Figure 3.22: Block diagram of three stage transimpedance design with single power supply

Variables were used for certain component parameters throughout the detailed TIA schematic (Figure 3.13). This was done for ease of optimization. Table 3.12 lists the variables and a short description of each parameter.

Table 3.12: TIA parameter variables

Name	Description
Feedback	Feedback resistance
R1	Load resistance of input stage
R2	Load resistance of output stage
Cd1	Input coupling capacitance
Cd2	Output coupling capacitance
Ib	Common mode base current
Rsupply	Current supply resistance

As all three stages are integrated and feedback is added, the gain, frequency response, and noise analysis of the amplifier becomes quite complicated. Thus, in order to meet the receiver specifications listed in Table 3.1, the variable values were optimized in ADS based upon the intrinsic design tradeoffs of the amplifier. These tradeoffs include gain versus bandwidth, gain flatness versus bandwidth, gain versus noise, and bandwidth versus noise. Initially, only gain and bandwidth were considered. Noise analysis of the amplifier will be revisited in chapter 5.

Approximations can be made for the bandwidth and gain equations for the feedback TIA. The bandwidth of the TIA is limited by the time constant from the equivalent Miller feedback resistance and input capacitance of the TIA. Therefore, the 3-dB bandwidth can be estimated in terms of feedback resistance, R_f , by equation 3.29.

$$BW \approx \frac{A_1}{2\pi R_f (C_{PD} + C_{BE,Qin})} \quad (3.29)$$

where A_1 represents the low frequency open-loop voltage gain of the first stage given in equation 3.13. C_{PD} and $C_{BE,Qin}$ are the photodiode and TIA input capacitances, respectively.

The transimpedance of the TIA determines the gain of the amplifier and is estimated by equation 3.30.

$$TZ = \frac{V_{out}}{I_{in}} \approx Rf \left[\frac{R_{iL} // R_{eL}}{R_E} \right] \quad (3.30)$$

where R_{iL} is the internal load resistance, R_{eL} is the external load resistance, and R_E is the emitter degeneration resistance of the final stage. As equations 3.29 and 3.30 show, there is a direct tradeoff between gain and bandwidth in terms of feedback resistance. As feedback resistance increases, bandwidth decreases, while transimpedance or gain increases [36].

One of the most important tradeoffs of the TIA is gain versus bandwidth. This tradeoff was exploited in the optimization of variable values for the parameters in Table 3.12. By changing the variable values, different operating points were achieved with different gains and bandwidths. Figure 3.23 presents a plot of gain versus bandwidth for multiple operating points. In addition to this plot, a linear trend line has been fit to the data. This plot again emphasizes the fact that if either gain or bandwidth is increased, the other performance parameter must decrease at an approximately linear rate.

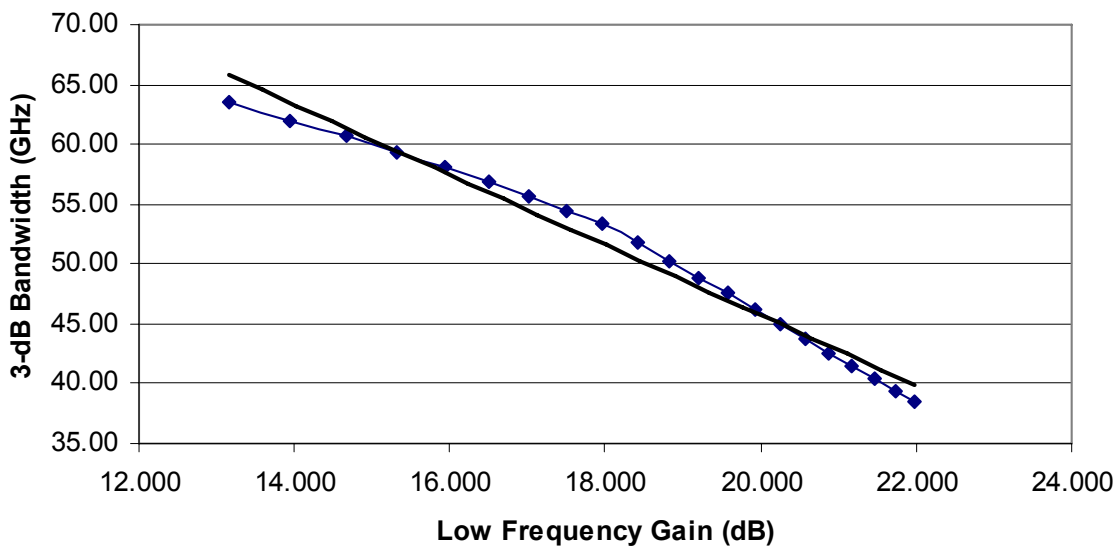


Figure 3.23: Gain versus bandwidth of the transimpedance amplifier

The most influential variable in the transimpedance differential amplifier is the feedback resistor. A 100 Ω resistor was selected because it allowed for good gain with a high bandwidth. Figure 3.24 provides plot of both gain and bandwidth versus feedback resistance. This figure shows that as feedback resistance is increased, bandwidth decreases, while gain increases.

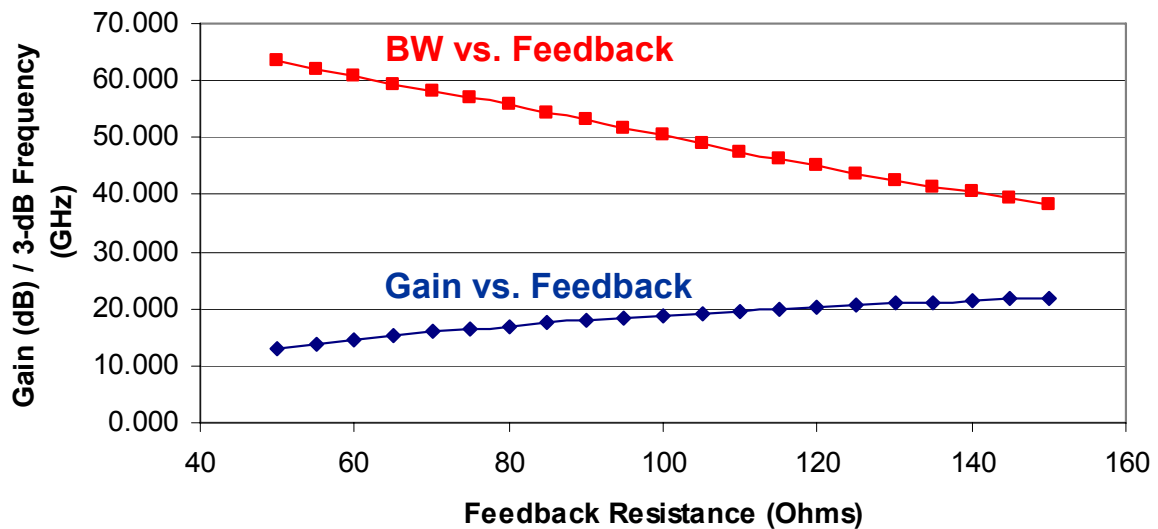


Figure 3.24: Gain / bandwidth versus feedback resistance

Although some of the lower feedback resistances provided very high bandwidth with good gain, the frequency response was not flat in many of these cases. Below, S21 has been plotted for a range of feedback values. 100 Ω feedback provides for a gain of 18.82 dB, a bandwidth of 50.31 GHz, and a totally flat gain response.

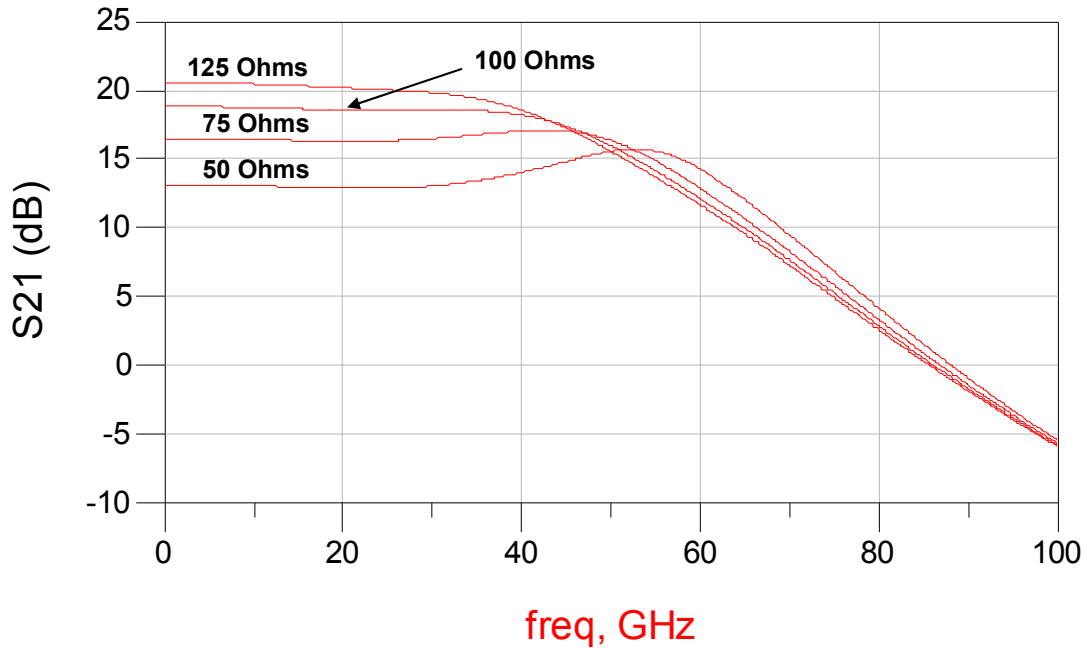


Figure 3.25: S21 for various feedback resistances (50, 75, 100, 125 Ω)

The values for the rest of the parameters in Table 3.12 were optimized in a similar fashion as feedback resistance. First, a value was chosen that provided the highest gain and largest bandwidth possible. The value was then modified until all of the amplifier specifications (Table 3.1) were met. One by one, the parameters were optimized until the final set of values was found that met all specifications at 50 GHz. The values for each parameter variable are listed below in Table 3.13.

Table 3.13: TIA parameter variables

Name	Description	Units	Optimized Value
Feedback	Feedback resistance	Ω	100
R1	Load resistance of input stage	Ω	110
R2	Load resistance of output stage	Ω	45
Cd1	Input coupling capacitance	μF	1
Cd2	Output coupling capacitance	μF	1
Ib	Common mode base current	mA	0.138
Rsupply	Current supply resistance	Ω	240

The results found for the TIA design are presented in chapter 4.

3.6 Photodiode Integration

After the TIA amplifier was analyzed, designed, and simulated, it was integrated with two balanced photodiodes. As mentioned earlier in chapter 2, integration can be either discrete (hybrid) or monolithic. In the discrete receiver, the photodiodes are external or off chip from the TIA. In the monolithic receiver, the photodiodes are fabricated on the same chip. Circuit simulations will be done for both types of integration and results will be presented in chapter 4. This section of the thesis presents both circuit schematics used in simulations and the values for design parameters.

3.6.1 Hybrid Optical Receiver

Figure 3.26 depicts the discretely integrated optical receiver. Here, two balanced photodiodes are attached to the differential TIA via bond wires as discussed in chapter 2.

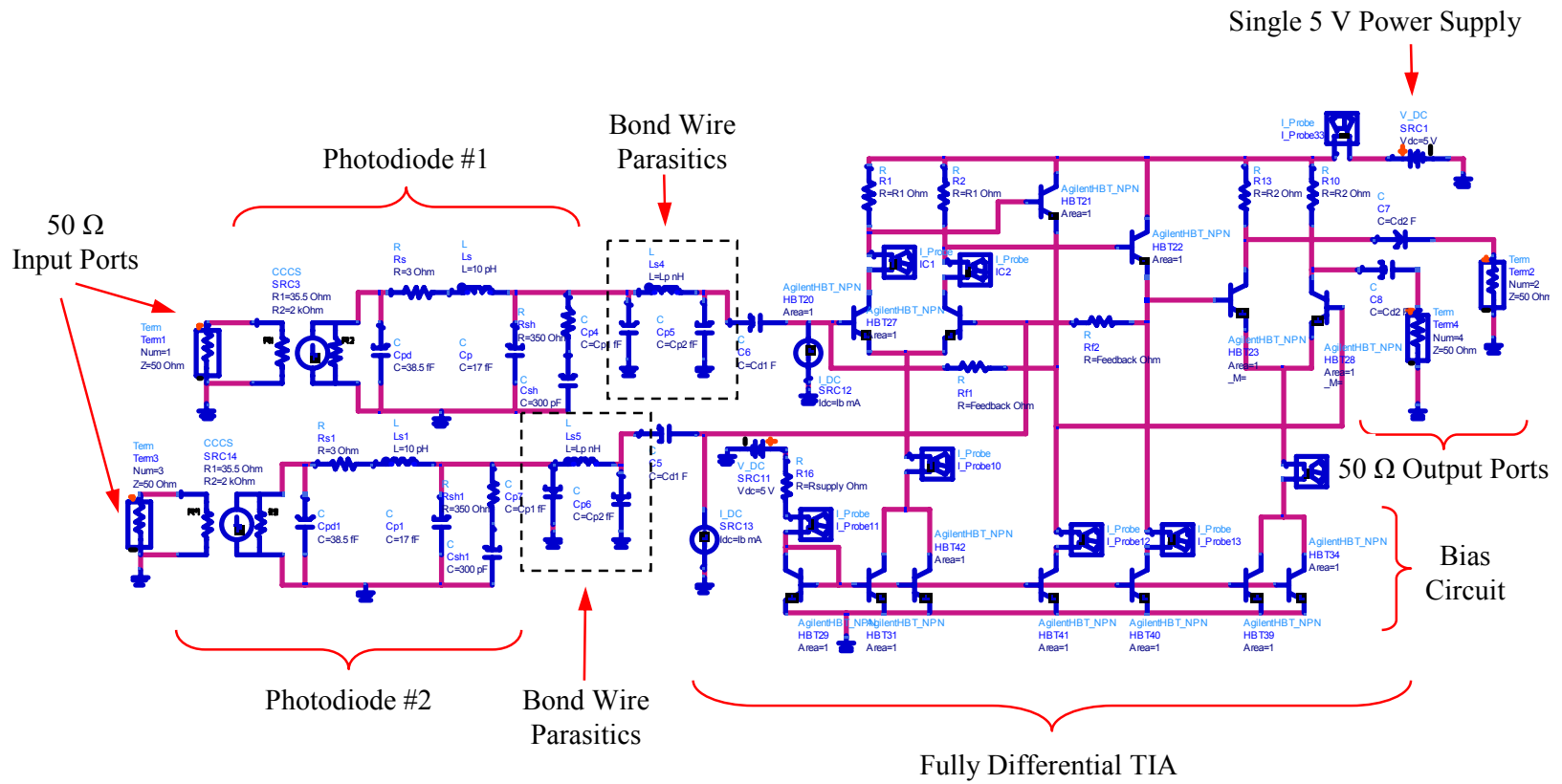


Figure 3.26: Discrete optical receiver with balanced photodiodes and differential TIA

As Figure 3.27 shows, the photodiodes have been implemented with identical models of the photodiode described in section 3.3 at the input of the differential TIA. Also, two capacitors and an inductor have been used to model the parasitics of the bond wire and pad capacitance.

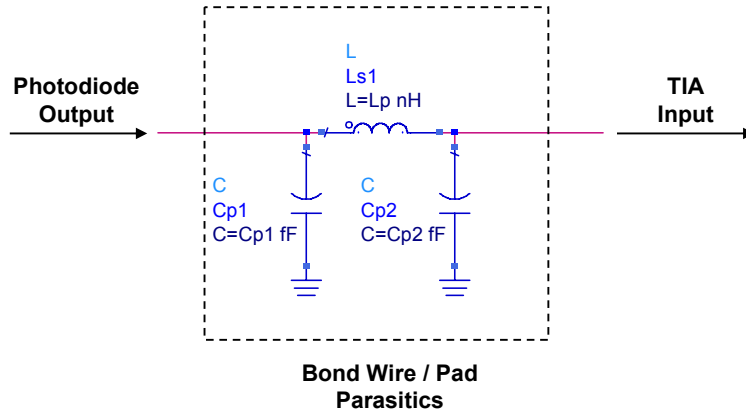


Figure 3.27: Parasitics model of bond wire and pad capacitance for the discrete receiver

Typical values of capacitance and inductance are listed in Table 3.14 to represent realistic bond wire and pad parasitics [54-55]. It should be noted that the bond wire inductance may cause unwanted gain peaking in the amplifier reducing the gain flatness of the receiver and degrading the overall receiver performance [26].

Table 3.14: Bond wire and pad parasitic values [54-55]

Name	Description	Units	Value
C_{p1}	Pad capacitance + bond wire capacitance	fF	10
C_{p2}	Pad capacitance + bond wire capacitance	fF	10
L_p	Bond wire inductance	nH	0.5

The values have been modified from those presented for the stand-alone TIA to accommodate the newly integrated photodiodes, and optimization was used to find values that approached the design specifications of Table 3.1. Table 3.15 lists these design values.

Table 3.15: Discrete optical receiver parameter variables

Name	Description	Units	Optimized Value
Feedback	Feedback resistance	Ω	330
R1	Load resistance of input stage	Ω	45
R2	Load resistance of output stage	Ω	45
Cd1	Input coupling capacitance	μF	1
Cd2	Output coupling capacitance	μF	1
Ib	Common mode base current	mA	0.138
Rsupply	Current supply resistance	Ω	240

3.6.2 Monolithic Optical Receiver

Figure 3.28 depicts the monolithically integrated optical receiver. Here, two balanced photodiodes are directly attached to the input differential TIA. The two photodiodes are identical as described in section 3.3. In the case of the monolithically integrated device, no parasitics are added between the photodiodes and the TIA as it is assumed that connecting parasitic values are smaller than the parasitics of the photodiodes and TIA.

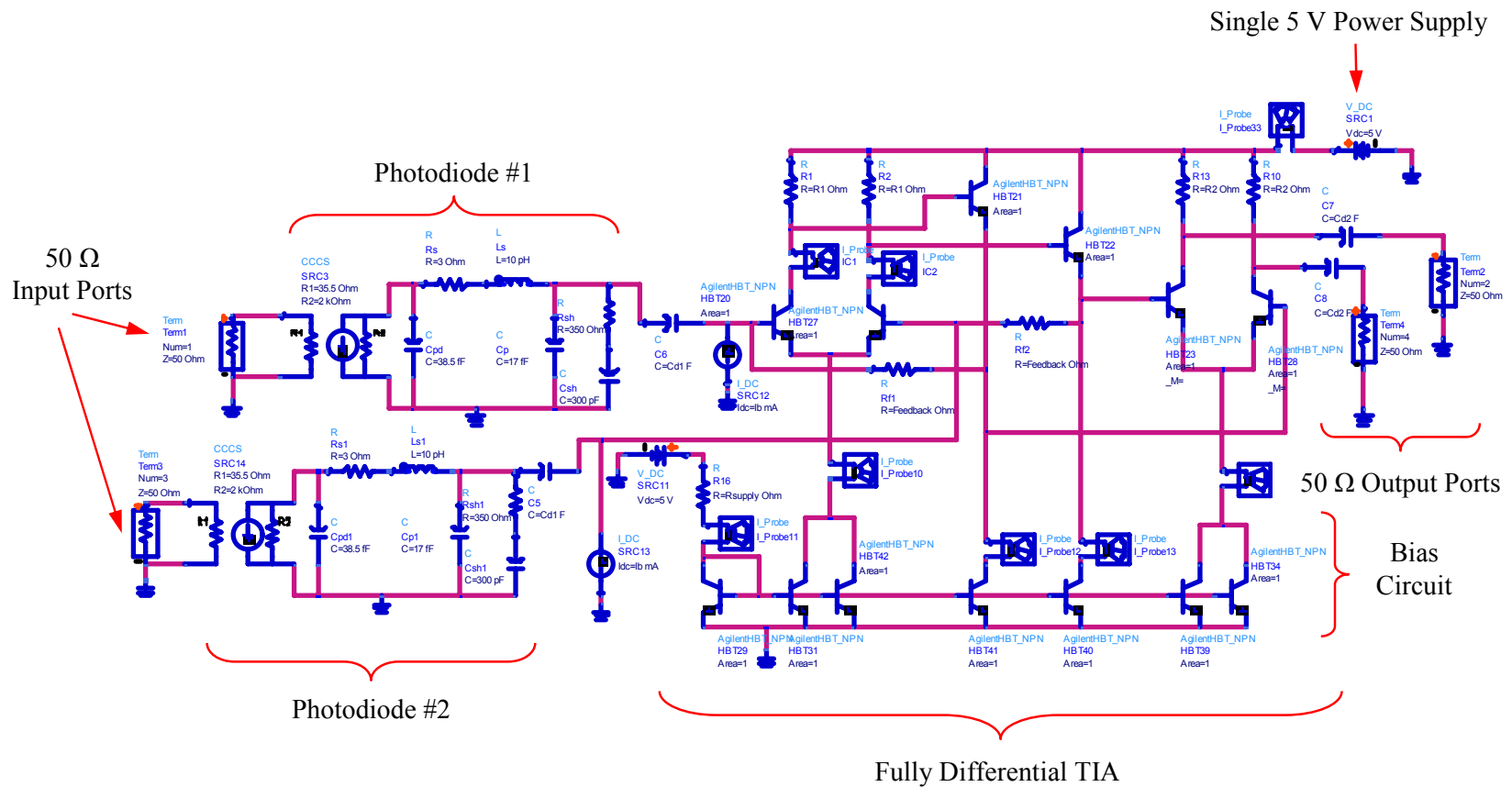


Figure 3.28: Monolithic optical receiver with balanced photodiodes and differential TIA

Now that the schematic has been presented for the monolithically integrated optical receiver, values are given to the design parameters of the device. These values have been modified from those presented for the stand-alone TIA to accommodate the newly integrated photodiodes. Again, optimization was used to find values that approached the design specifications of Table 3.1. Table 3.16 lists these design values. As this table shows, only feedback resistance and R_1 have been altered. Results for the monolithically integrated amplifier design will be presented in chapter 4 and will be compared to similar results for the discrete optical receiver previously discussed.

Table 3.16: Monolithic optical receiver parameter variables

Name	Description	Units	Optimized Value
Feedback	Feedback resistance	Ω	95
R1	Load resistance of input stage	Ω	45
R2	Load resistance of output stage	Ω	45
Cd1	Input coupling capacitance	μF	1
Cd2	Output coupling capacitance	μF	1
Ib	Common mode base current	mA	0.138
Rsupply	Current supply resistance	Ω	240

4. SIMULATION RESULTS AND ANALYSIS

4.1 Introduction

This chapter intends to provide the design simulation results of the optical receiver. It is divided in two sections: transimpedance amplifier and integrated optical receiver simulation results. The transimpedance amplifier simulations will be compared to published results when available, while for the monolithic receiver, the results will be analyzed against the discrete receiver ones. After designing and simulating the optical receiver, the following compliance table was created.

Table 4.1: Optical receiver specification and compliance table

Parameter	Specification	TIA Compliance	Monolithic Receiver Compliance
Low Frequency Gain (S21)	10.0 dB	18.8 dB	14.3 dB
3-dB Frequency	50.0 GHz	50.3 GHz	50.0 GHz
Unity Gain Frequency	80.0 GHz	86.1 GHz	75.6 GHz
S11 @ 50 GHz	-10.0 dB	-19.5 dB	-15.4 dB
S22 @ 50 GHz	-10.0 dB	-10.7 dB	-10.6 dB
S11 @ 100 GHz	-8.0 dB	-8.4 dB	-15.4 dB
S22 @ 100 GHz	-8.0 dB	-8.5 dB	-8.3 dB
Differential Transimpedance	50.0 dB- Ω	50.9 dB- Ω	46.9 dB- Ω
Clipped output eye amplitude	0.40 V	0.50 V	0.60 V
Input for clipped output eye	500 μ A	750 μ A	0.08 V
Dynamic Range	20.0 dB	28.8 dB	29.0 dB
Power Consumption	600 mW	492 mW	542 mW
Supply Voltage	5 V	5 V	5 V
Device Temperature	175 $^{\circ}$ C	144 $^{\circ}$ C	169 $^{\circ}$ C
3-dB Noise	100 pA/Hz ^(1/2)	See chapter 5	See chapter 5
Technology	InP DHBT / InGaAs PIN WGPD	InP DHBT	InP DHBT / InGaAs PIN WGPD
HBT f_t	230 GHz	289 GHz	289 GHz
HBT f_{max}	147 GHz	210 GHz	210 GHz
Photodiode 3 dB Frequency	70 GHz	--	--

The rest of this chapter details the simulations performed to create Table 4.1.

4.2 Transimpedance Amplifier Results

The parameter values of the transimpedance amplifier, presented in Table 4.2, were optimized so that the TIA met the previously defined design specifications. Simulations were executed to determine the DC operating points and the small and large signal performance. Results of these simulations are presented below.

Table 4.2: TIA parameter variables

Name	Description	Optimized Value
RF (Ω)	Feedback resistance	100
R1 (Ω)	Load resistance of input stage	110
R2 (Ω)	Load resistance of output stage	45
Cd1 (μF)	Input coupling capacitance	1
Cd2 (μF)	Output coupling capacitance	1
Ib (mA)	Common mode base current	0.138
Rsupply (Ω)	Current supply resistance	240

4.2.1 DC Simulations

DC simulations were performed on the TIA to determine bias conditions, power dissipation, and temperature operation. Since the TIA is differentially paired with identical loads, the DHBT pairs have equivalent biases so that the amplifier remains balanced. The conditions are listed below in Table 4.3. Results come directly from ADS simulations using the values listed in Table 4.2 for the schematic in Figure 3.13.

Table 4.3: Bias conditions of differential TIA amplifier stages (with single 5V power supply)

	Stage 1 DHBTs	Stage 2 DHBTs	Stage 3 DHBTs
I_C (mA)	12.67	16.05	12.70
I_B (μA)	167.9	227.5	179.8
V_{BE} (V)	1.37	1.38	1.37
V_{BC} (V)	-1.39	-1.42	-2.23
V_{CE} (V)	2.77	2.80	3.59

As Table 4.3 indicates, the collector current was almost 13 mA for stage 1 and 3 DHBTs, while collector current was 16 mA for stage 2 operation. As mentioned in chapter 3, stage 2

current is higher than other stages due to the design of the current mirrors. These bias conditions allowed for optimum operation, so no further modifications were made. Table 4.4 presents the DC conditions of the current mirrors used to bias the amplifier.

Table 4.4: Bias conditions of TIA bias circuit

	Diode connected DHBT	Stage 1 Mirror DHBTs	Stage 2 Mirror DHBTs	Stage 3 Mirror DHBTs
I_C (mA)	13.90	12.84	15.93	12.88
I_B (μA)	165.5	142.8	212.1	143.6
V_{BE} (V)	1.39	1.39	1.39	1.39
V_{BC} (V)	0.00	0.57	-0.82	0.55
V_{CE} (V)	1.39	0.81	2.20	0.84

Now that the bias conditions are known for the circuit, the total power dissipated can be calculated. Table 4.5 lists the power dissipation for the TIA amplifier by stage. Dissipated power was found for all DHBTs and resistors by using equations 4.1-4.2.

$$P_{\text{dissDHBT}} = V_{CE} I_{CE} \quad (4.1)$$

$$P_{\text{dissResistor}} = I_R^2 R \quad (4.2)$$

Table 4.5: Dissipated power for TIA

	Device Size	Power per device (mW)	No. of Devices	Power (mW)
Stage 1 DHBTs	20 μm ²	35.31	2	70.62
Stage 2 DHBTs	20 μm ²	45.25	2	90.49
Stage 3 DHBTs	20 μm ²	45.86	2	91.72
Stage 1 Resistors	110 Ω	18.30	2	36.59
Stage 3 Resistors	45 Ω	7.25	2	14.51
Feedback Resistors	100 Ω	0.003	2	0.01
Total				303.94

Table 4.5 shows a total power of 303.9 mW. Table 4.6 lists the dissipated power for the amplifier bias circuit.

Table 4.6: Dissipated power for TIA bias circuit

	Device Size	Power per device (W)	No. of Devices	Power (mW)
Diode connected DHBT	20 μm^2	19.48	1	19.48
Stage 1 Mirror	20 μm^2	10.63	2	21.26
Stage 2 Mirror	20 μm^2	35.36	2	70.72
Stage 3 Mirror	20 μm^2	10.93	2	21.86
Supply Resistor	240 Ω	54.44	1	54.44
Total				187.77

Table 4.6 shows a total power of 187.7 mW. Therefore, the total power of the differential transimpedance amplifier is 491.7 mW. Stage 1 (DHBTs and resistors) accounts for 22% of the total power, stage 2 accounts for 18%, and stage 3 accounts for 22%. The TIA bias circuit accounts for the remaining 38%. Figure 4.1 provides a visual of the power dissipation breakdown.

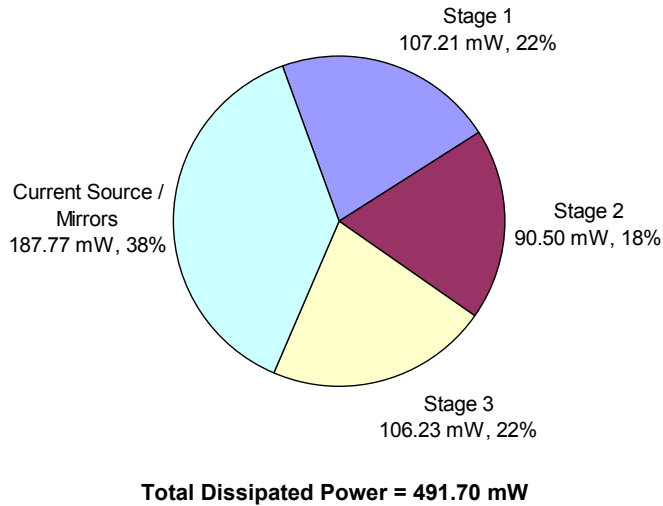


Figure 4.1: Dissipated power breakdown for differential TIA

The amplifier power consumption found in this simulation can be compared to results found in literature for a similar InP TIA with 30 GHz bandwidth [91]. In [91], the power consumption is measured to be 260 mW, as compared to the 300 mW value found in simulations. The higher power for the designed TIA is on account of the 12.5 dB greater gain and 20 GHz wider bandwidth than the measured TIA [91].

The final set of DC results found was the temperature operation of each DHBT in the amplifier. The detailed temperature operation was discussed in section 3.2 and the amplifier specification was set to below 175°C. The final temperature of the device is a function of the bias conditions and thermal resistance as follows:

$$T_F = T_I + R_{th}(I_C V_{CE}) \quad (4.3)$$

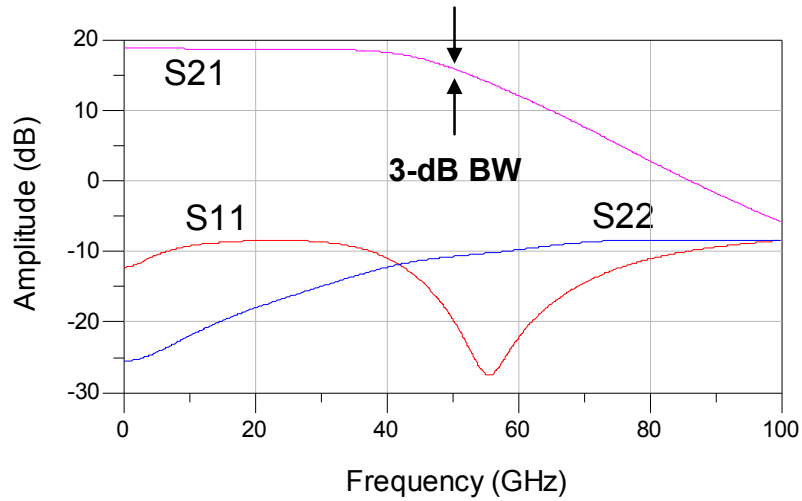
Table 4.7 lists the final temperature of all transistors in the amplifier demonstrating that the lowest temperature is 53.5°C and the highest is 144.2°C. Worthwhile for notice are stages 1 and 2 which indicate that, in the current mirrors, using devices in parallel to accommodate large current is a good means for lowering device temperature.

Table 4.7: Temperature operation of DHBTs in TIA

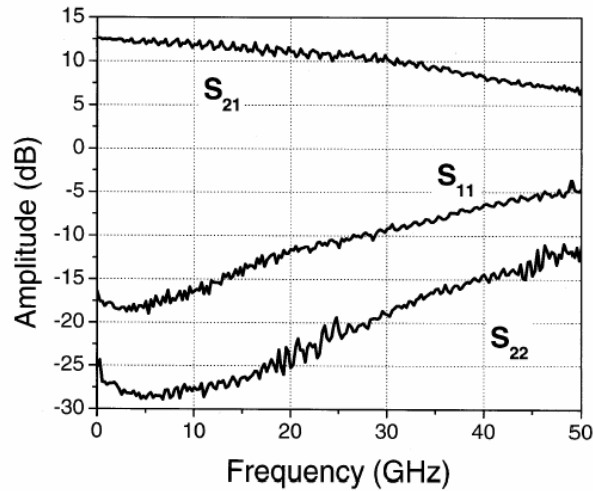
	Temperature (°C)
Stage 1 DHBTs	116.8
Stage 2 DHBTs	142.6
Stage 3 DHBTs	144.2
Diode connected DHBT	75.7
Stage 1 Mirror DHBTs	52.6
Stage 2 Mirror DHBTs	116.9
Stage 3 Mirror DHBTs	53.5

4.2.2 Small Signal Simulations

As defined in chapter 2, S21 defines the gain and bandwidth of the amplifier, while S11 and S22 are a measure of input and output reflections. When available, the small signal (S-parameter) simulations can be compared against published values of measurements for similar amplifiers. Figure 4.2 compares one single ended simulated result to a measured InP TIA [91]. Differential gain is naturally larger than single ended gain (approx. 6 dB larger). Therefore, the simulated results would display a fully differential gain (S21) of over 20 dB as compared to the measured gain of 12 dB [91].



(a) Simulated S-parameters (single ended): Supply voltage = 5V



(b) Measured S-parameters (fully differential)

Figure 4.2: S-parameters from (a) simulated InP design and (b) measured InP results found in “SiGe Differential Transimpedance Amplifier with 50-GHz Bandwidth” by Weiner [91]

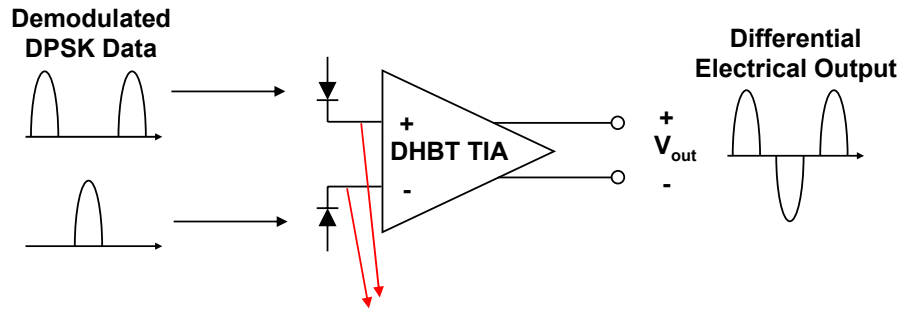
Table 4.8 summarizes the simulations against InP and SiGe TIAs published for two similar amplifiers [91].

Table 4.8: Differential TIA high frequency comparison of simulated results to Weiner's measured results [91]

Measurement	Simulated InP TIA	Measured InP TIA [91]	Measured SiGe TIA [91]
3-dB Bandwidth (GHz)	50.31	30.00	> 50.00
Unity Gain Freq (GHz)	86.10	--	--
Gain S21 (dB)	18.82	12.00	12.00
S11 (dB) @ 50 GHz	-19.50	< -5.00	< -10.00
S22 (dB) @ 50 GHz	-10.72	< -11.00	< -12.00
S11 (dB) @ 100 GHz	-8.42	--	--
S22 (dB) @ 100 GHz	-8.54	--	--
* Differential Transimpedance (dB-Ω)	50.90	48.00	49.00

4.2.3 Large Signal Simulations

The large-signal simulations were performed in the form of transient responses and eye diagrams for the frequency range of 10 to 50 GHz. Figure 4.3 depicts the input to the differential transimpedance amplifier used to produce the simulations in this section of the report. This input represents the output of two balanced photodiodes that are detecting a demodulated NRZ-DPSK signal as described in chapter 2. The two sources are pseudo-random bit sequence (PRBS) voltage sources with 127 bit (2^7-1) pattern length. The current controlled current sources (CCCSs) will convert the voltage input into a current, to simulate the photodiode output.



Models output of PDs detecting DPSK

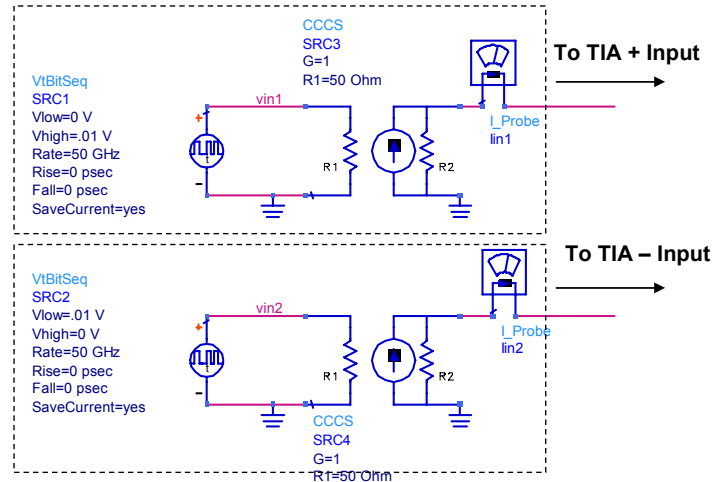


Figure 4.3: Transient analysis input to differential TIA

The large signal simulations of the amplifier with a transient stimulus are shown in Figure 4.4. The stimulus is a 50 GHz differential 200 μ A input data stream with a rise and fall time of 2 ns. The driving current simulates the output current of a photodiode detecting a demodulated DPSK signal. The differential output voltage is approximately 0.275 V_{pp} given by:

$$V_{diffout} = V_{out+} - V_{out-} \quad (4.4)$$

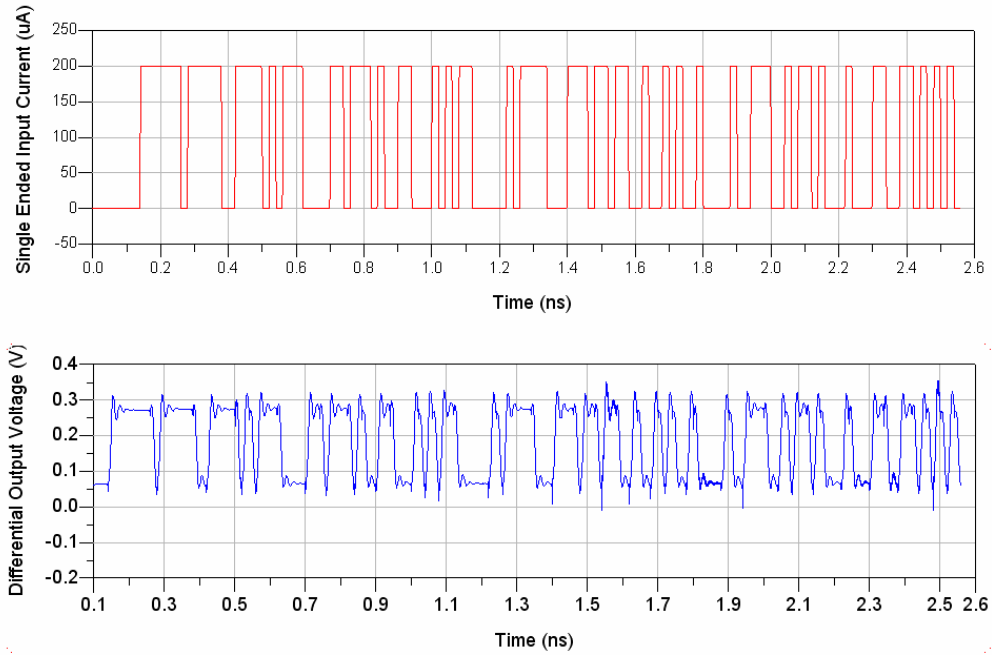
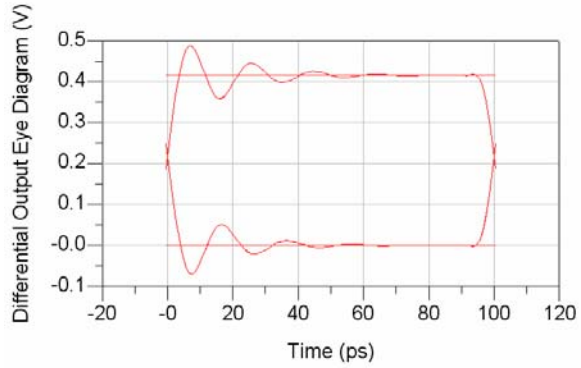


Figure 4.4: TIA transient input current and output voltage

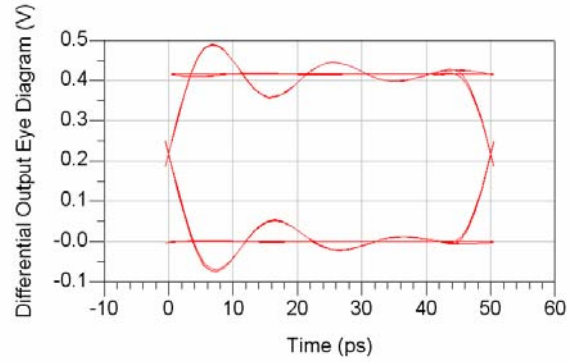
The transient response follows well with the given 50 GHz input for the entire data stream.

The eye diagrams were simulated at 10, 20, 30, and 40 GHz with the same differential data input data stream as above. Figure 4.5 (a) through (d) illustrates the output eye diagrams.

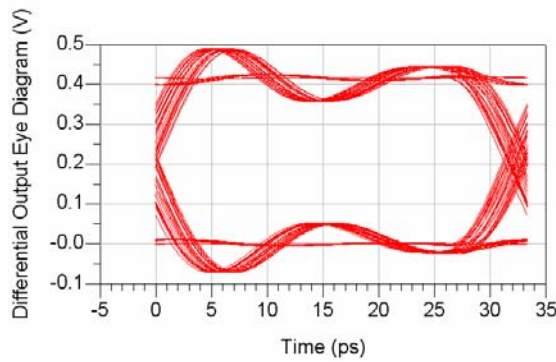
The single ended input current was 500 μ A for all cases.



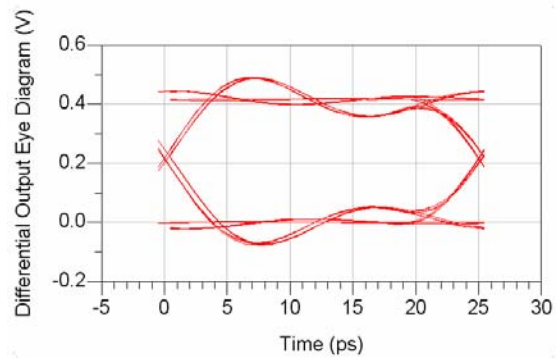
(a) 10 GHz operation



(b) 20 GHz operation



(c) 30 GHz operation

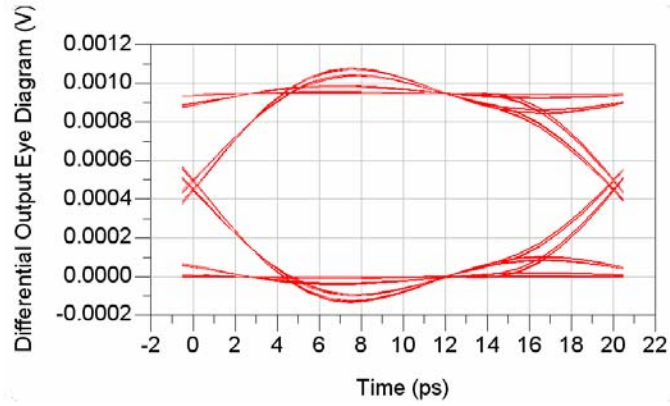


(d) 40 GHz operation

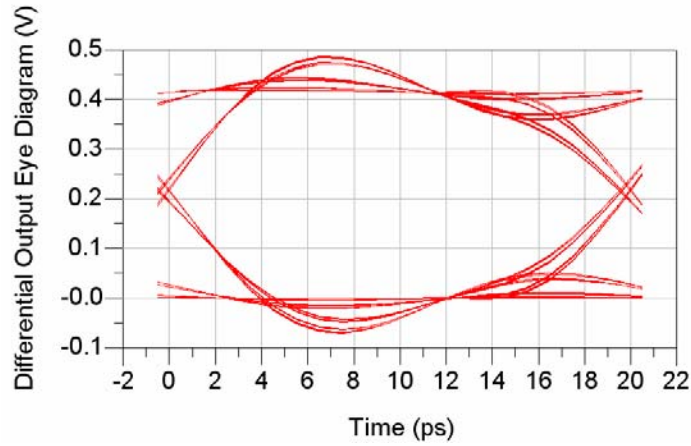
Figure 4.5: Differential output eye diagram driven with input current of 500 μA

The eye diagrams are open over the wide frequency range indicating that the amplifier is not bandwidth limited. The differential output amplitude remains at 0.4 V_{pp} for the 500 μA input.

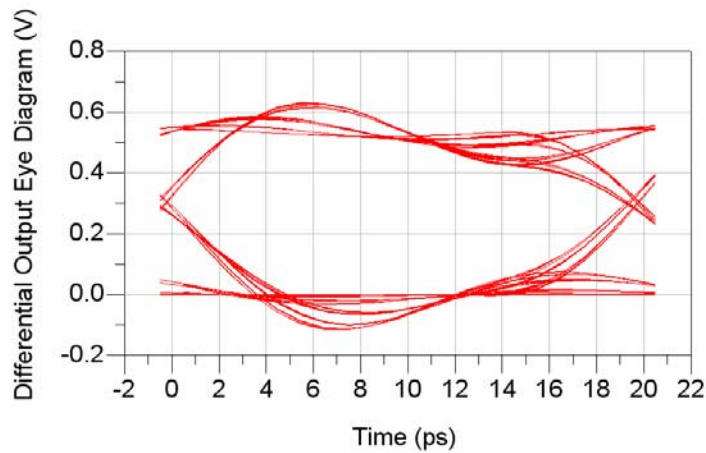
Figure 4.6 illustrates the output eye diagram for the differential TIA when driven with a 50 GHz differential input data stream. The current was varied between 1 μA , 500 μA , and 750 μA for the single ended input.



(a) 50 GHz – 1 μ A single ended input



(b) 50 GHz – 500 μ A single ended input



(c) 50 GHz – 750 μ A single ended input

Figure 4.6: Differential output eye diagram driven with various 50 GHz PRBS amplitudes

The output swing (vertical eye openings) for 1 μA , 500 μA , and 750 μA inputs are 0.09 V_{pp} , 0.4 V_{pp} , and 0.5 V_{pp} , respectively. However, the differential TIA output was pushed into clipping when the input was driven with 750 μA . At this point, the differential output amplitude is approximately 0.5 V_{pp} which is slightly lower than the measured results of 0.7 V_{pp} [91].

In chapter 2, dynamic range is defined as the difference between the smallest and largest optical powers that can be successfully amplified by the front-end amplifier. From the values of Figure 4.6 and assuming 0.37 A/W for the photodiode response (chapter 3):

$$OpticalPower_{\min} = \frac{I_{photo}}{R_{A/W}} = \frac{1\mu\text{A}}{0.37\text{ A/W}} = 0.0027\text{ mW} = -25.69\text{ dBm} \quad (4.5)$$

$$OpticalPower_{\max} = \frac{I_{photo}}{R_{A/W}} = \frac{750\mu\text{A}}{0.37\text{ A/W}} = 2.0270\text{ mW} = 3.07\text{ dBm} \quad (4.6)$$

The optical dynamic range of the TIA is given in equation 4.7. This wide dynamic range eliminates the need for a post amplifier in the optical receiver.

$$Dynamic\ Range = P_{\max} - P_{\min} = 28.76\text{ dB} \quad (4.7)$$

Figure 4.7 plots the differential output eye amplitude versus the input optical power for the transimpedance amplifier design. This plot further illustrates the wide dynamic range of the amplifier.

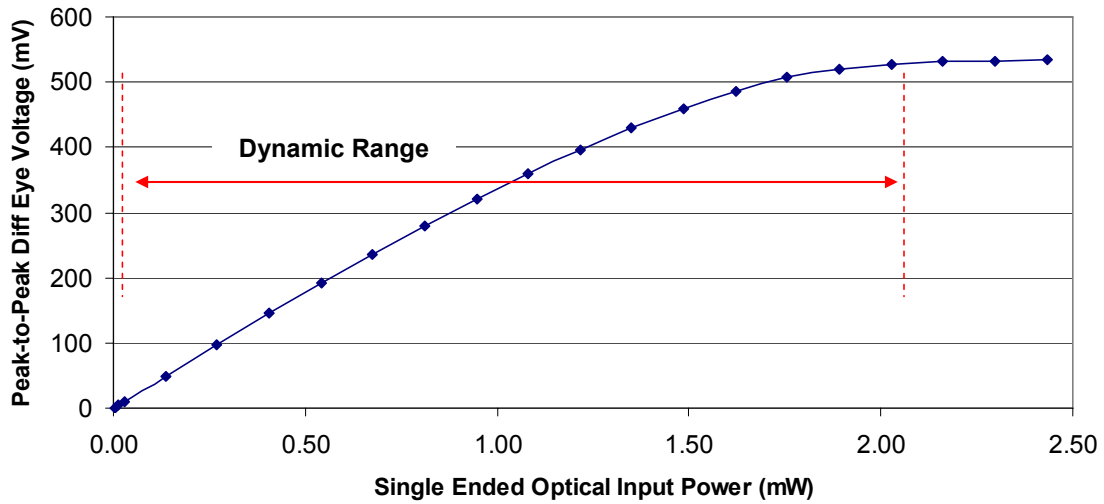


Figure 4.7: Differential output eye amplitude versus photocurrent

Finally, Figure 4.8 provides the measured eye diagrams presented by Weiner for comparison purposes. In 4.8 (a), the InP TIA was driven with a $0.05 V_{pp}$ input data stream at 40 Gb/s and achieved an output amplitude of $0.15 V_{pp}$. In 4.8 (b), the output is clipped at $0.70 V_{pp}$ for an input amplitude of $0.40 V_{pp}$. The horizontal scale is 10 ps per division [91].

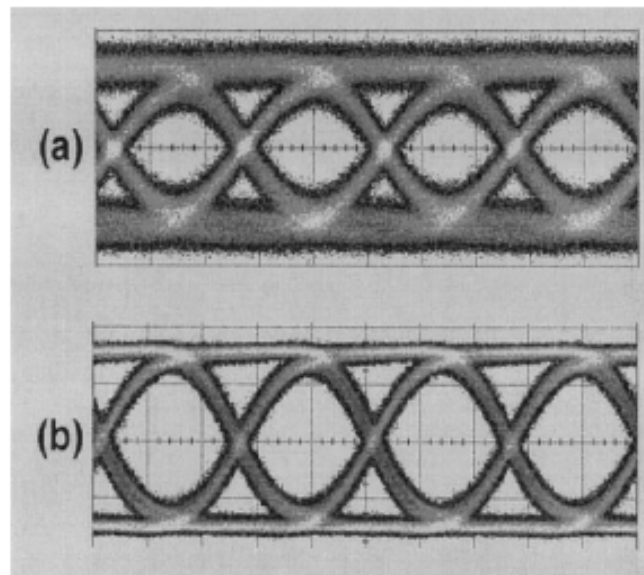


Figure 4.8: Measured InP TIA results [91]

In summary, the simulated differential TIA proved to have comparable large signal results to actual fabricated and measured devices [91]. Table 4.9 summarizes the results.

Table 4.9: Large signal simulations for differential TIA as compared to measured TIA published by Weiner [91]

Measurement	Simulated InP TIA	Measured InP TIA [91]
Feedback Resistance	100 Ω	160 Ω
Gain S21	18.82 dB	12.00 dB
3-dB Bandwidth	50.31 GHz	30.00 GHz
HBT f_t @ bias	289 GHz	170 GHz
HBT f_{max} @ bias	210 GHz	140 GHz
V_{supply}	5 V	4-5.2 V
Output eye amplitude with 0.05 V input	0.40 V	0.15 V
Clipped output eye amplitude	0.50 V	0.70 V
Input for clipped output eye	750 μ A	0.20 V
Dynamic Range	28.76 dB	--
Maximum data rate	50 Gb/s	42.7 Gb/s

4.3 Integrated Optical Receiver Results

This chapter presents and compares the simulation results for two receivers: the discrete (Figure 3.26) and the monolithically integrated receiver (Figure 3.28). As discussed in chapter 3, the parameter values of the optical receivers were optimized so that the receiver approached design specifications. Table 4.10 again presents the values of the major design parameters for both receivers. The single difference between the two is the value of feedback resistance used.

Table 4.10: Optical receiver parameter values

Name	Description	Discrete Receiver	Monolithic Receiver
RF (Ω)	Feedback resistance	330	95
R1 (Ω)	Load resistance of input stage	45	45
R2 (Ω)	Load resistance of output stage	45	45
Cd1 (μ F)	Input coupling capacitance	1	1
Cd2 (μ F)	Output coupling capacitance	1	1
Ib (mA)	Common mode base current	0.138	0.138
Rsupply (Ω)	Current supply resistance	240	240

Using these values, the two receivers were simulated to determine the DC, high frequency, and large signal performance. Results of these simulations and a comparison between the two receivers are presented below.

4.3.1 DC Simulations

DC simulations were performed on both receivers to determine bias conditions, power dissipation, and temperature operation. The first DC simulation allowed for the discovering of the bias conditions of the receivers. These conditions are listed below in Table 4.11 for the discrete receiver and 4.12 for the monolithic receiver. Results come directly from ADS simulations using the values listed in Table 4.9 for the schematics in Figures 3.26 and 3.28.

Table 4.11: Bias conditions of discrete receiver amplifier stages

	Stage 1 DHBTs	Stage 2 DHBTs	Stage 3 DHBTs
Ic (mA)	13.79	18.65	13.92
Ib (μA)	187.8	253.6	189.2
Vbe (V)	1.37	1.39	1.38
Vbc (V)	-1.46	-0.63	-1.40
Vce (V)	2.83	2.03	2.77

Table 4.12: Bias conditions of monolithic receiver amplifier stages

	Stage 1 DHBTs	Stage 2 DHBTs	Stage 3 DHBTs
Ic (mA)	13.88	18.63	13.91
Ib (μA)	188.5	253.4	189.1
Vbe (V)	1.37	1.39	1.37
Vbc (V)	-1.41	-0.64	-1.40
Vce (V)	2.79	2.03	2.78

As Table 4.11 and 4.12 indicate, there is little difference in biasing between the two receivers. This is expected because the only differences between the two designs are the feedback resistance value and the addition of the bond wire in the discrete receiver. It will be shown that the bond wire negatively affects receiver performance at high frequencies. It should also be noted that the bias currents are somewhat higher than the 13 mA as originally

intended. Because these bias conditions allowed for optimum receiver performance, no further modifications were made. Table 4.13 and 4.14 presents the DC conditions of the current mirrors used to bias the amplifier.

Table 4.13: Bias conditions of discrete receiver bias circuit

	Diode connected DHBT	Stage 1 Mirror DHBTs	Stage 2 Mirror DHBTs	Stage 3 Mirror DHBTs
Ic (mA)	13.66	13.98	18.52	14.11
Ib (μA)	162.2	169.2	280.0	172.1
Vbe (V)	1.38	1.38	1.38	1.38
Vbc (V)	0	-0.15	-1.59	-0.21
Vce (V)	1.38	1.54	2.97	1.60

Table 4.14: Bias conditions of monolithic receiver bias circuit

	Diode connected DHBT	Stage 1 Mirror DHBTs	Stage 2 Mirror DHBTs	Stage 3 Mirror DHBTs
Ic (mA)	13.66	14.06	18.50	14.10
Ib (μA)	162.1	171.0	279.3	171.9
Vbe (V)	1.38	1.38	1.38	1.38
Vbc (V)	0	-0.19	-1.59	-0.21
Vce (V)	1.38	1.58	2.97	1.59

Now that the bias conditions are known for each receiver, the total power dissipated can be calculated. Table 4.15 and 4.16 list the power dissipation for each receiver by stage. Dissipated power was found for all DHBTs and resistors by using equations 4.1-4.2.

Table 4.15: Dissipated power for discrete receiver

	Power per device (mW)	No. of Devices	Power (mW)
Stage 1 DHBTs	39.30	2	78.60
Stage 2 DHBTs	38.14	2	76.28
Stage 3 DHBTs	38.90	2	77.80
Stage 1 Resistors	8.88	2	17.76
Stage 3 Resistors	8.73	2	17.46
Feedback Resistors	0.0116	2	0.0232
Total			267.92

Table 4.16: Dissipated power for monolithic receiver

	Power per device (mW)	No. of Devices	Power (mW)
Stage 1 DHBTs	38.93	2	77.86
Stage 2 DHBTs	38.20	2	76.40
Stage 3 DHBTs	38.93	2	77.86
Stage 1 Resistors	8.98	2	17.96
Stage 3 Resistors	8.71	2	17.42
Feedback Resistors	0.0034	2	0.0067
Total			267.51

The total dissipated power for the discrete receiver was nearly identical to the total dissipated power for the monolithic receiver as is expected. Table 4.17 and 4.18 list the dissipated power for the receiver bias circuits.

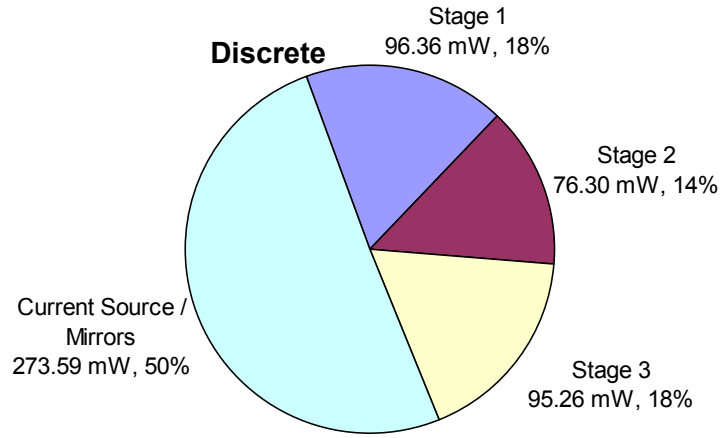
Table 4.17: Dissipated power for discrete receiver bias circuit

	Power per device (W)	No. of Devices	Power (mW)
Diode connected DHBT	19.13	1	19.13
Stage 1 Mirror	21.73	2	43.46
Stage 2 Mirror	55.47	2	110.94
Stage 3 Mirror	22.80	2	45.60
Supply Resistor	54.46	1	54.46
Total			273.53

Table 4.18: Dissipated power for monolithic receiver bias circuit

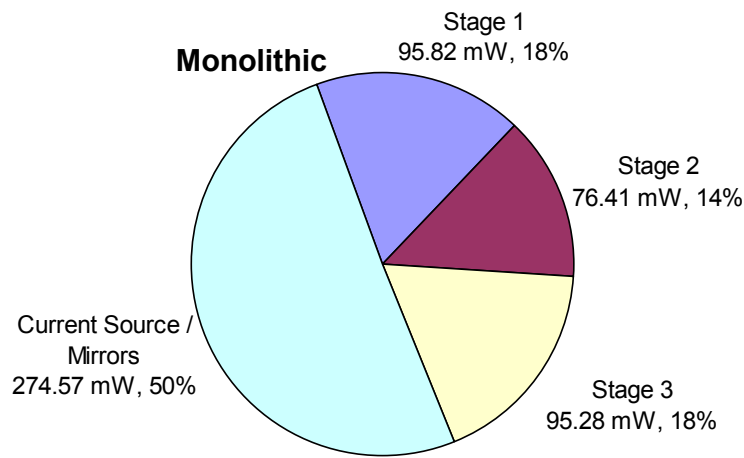
	Power per device (W)	No. of Devices	Power (mW)
Diode connected DHBT	19.13	1	19.13
Stage 1 Mirror	22.42	2	44.84
Stage 2 Mirror	55.34	2	110.68
Stage 3 Mirror	22.73	2	45.46
Supply Resistor	54.46	1	54.46
Total			274.57

Again, dissipated power values were nearly equivalent in both receiver bias circuits. The total power of the discrete receiver is 541.51 mW, while the total power of the monolithic receiver is 542.08 mW. Figure 4.9 provides a visual of the power dissipation breakdown in both receivers.



Total Dissipated Power = 541.51 mW

(a) Discrete receiver dissipated power breakdown



Total Dissipated Power = 542.08 mW

(b) Monolithic receiver dissipated power breakdown

Figure 4.9: Dissipated power breakdown for optical receivers

The final set of DC results found was the operating temperature of the DHBTs in each receiver. Temperature operation was discussed in section 3.2 and the specification of the amplifier was set to below 175°C. The final temperature of the device is a function of the bias conditions and thermal resistance as shown in equation 4.3. Table 4.19 and 4.20 list the

final temperature of all DHBTs in each receiver. As these tables show, all devices meet specifications with the worst case temperature being 169.2°C.

Table 4.19: Temperature operation of DHBTs in discrete receiver

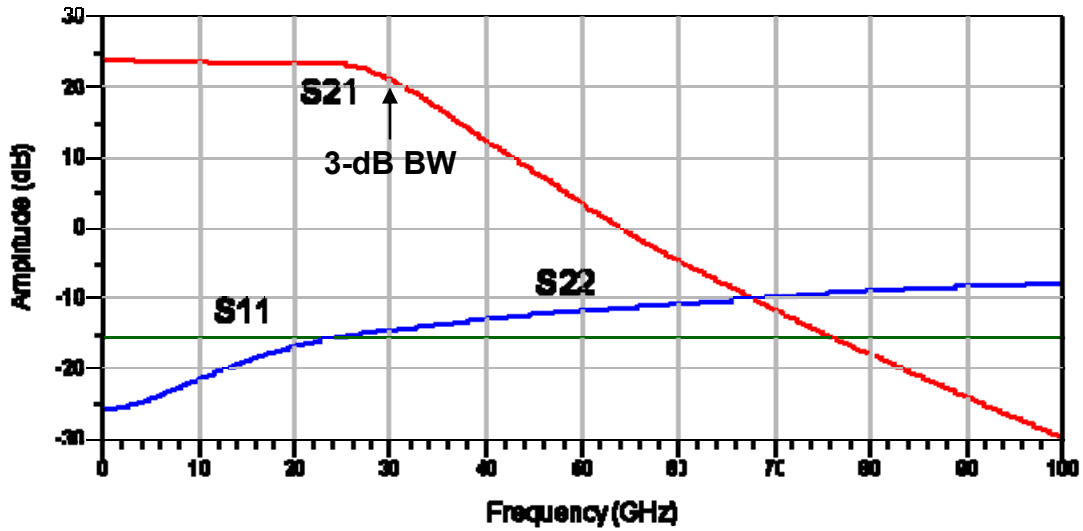
	Temperature (°C)
Stage 1 DHBTs	127.2
Stage 2 DHBTs	124.2
Stage 3 DHBTs	126.1
Diode connected DHBT	74.8
Stage 1 Mirror DHBTs	81.5
Stage 2 Mirror DHBTs	169.2
Stage 3 Mirror DHBTs	84.3

Table 4.20: Temperature operation of DHBTs in monolithic receiver

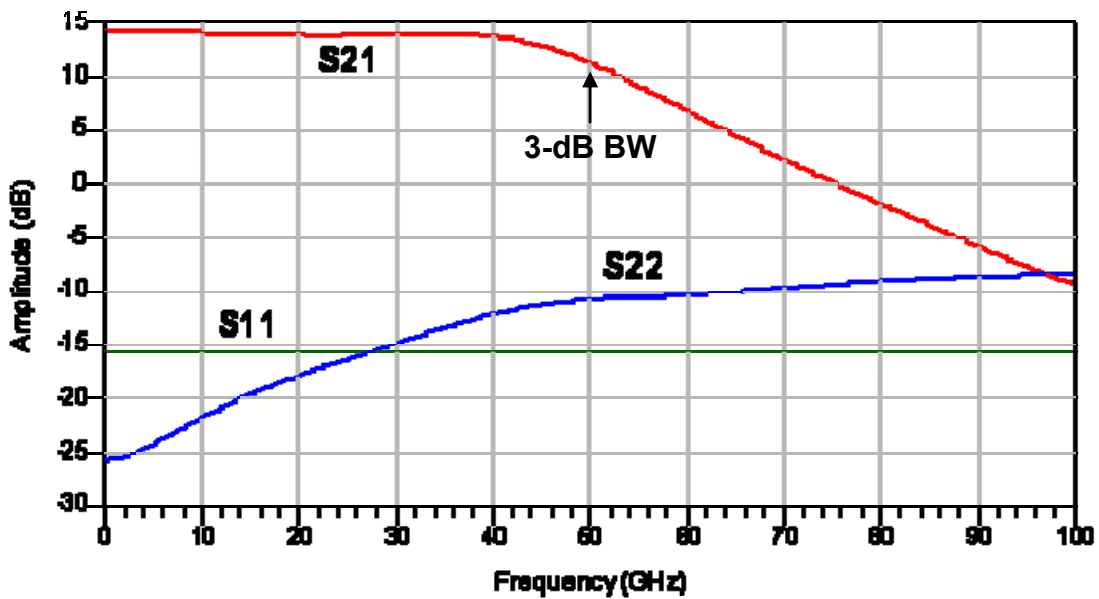
	Temperature (°C)
Stage 1 DHBTs	126.2
Stage 2 DHBTs	124.2
Stage 3 DHBTs	126.2
Diode connected DHBT	74.8
Stage 1 Mirror DHBTs	83.3
Stage 2 Mirror DHBTs	168.9
Stage 3 Mirror DHBTs	84.1

4.3.2 Small Signal Simulations

The next major simulation set comes from the S-parameters of the optical receivers. This high frequency analysis shows how the bond wire of a discrete receiver negatively impacts receiver performance. S-parameters of both receivers are compared in Figure 4.10. In both cases, the simulated S21 is the single ended gain.



(a) Discrete receiver design



(b) Monolithic receiver design

Figure 4.10: S-Parameters from (a) discrete receiver design (b) monolithic receiver design:
Supply voltage = 5V

Figure 4.10 shows that the bandwidth of the monolithic receiver is on the order of 20 GHz greater than that of the discrete receiver. Bond wire and pad capacitance parasitics are the cause for decrease in bandwidth in the discrete case. The discrete receiver has higher gain

than the monolithic receiver mainly due to the increase of feedback resistance in the design which was used to reduce the gain peaking caused by the inductance of the bond wires [26]. To further compare the two, Table 4.21 was created. As the results show, the monolithic integrated receiver has sufficient gain with a larger bandwidth than the discrete receiver.

Table 4.21: High frequency comparison of monolithic receiver versus discrete receiver

Measurement	Monolithic Receiver	Discrete Receiver	% Difference
Gain S21 (dB)	14.26	24.04	40.7 %
3-dB Bandwidth (GHz)	50.01	30.31	39.4 %
Unity Gain Freq (GHz)	75.60	54.10	29.4 %
S11 (dB) @ 50 GHz	-15.42	-15.41	0.1 %
S22 (dB) @ 50 GHz	-10.61	-11.55	8.1 %
S11 (dB) @ 100 GHz	-15.41	-15.41	0.0 %
S22 (dB) @ 100 GHz	-8.31	-7.95	4.3 %
* Differential Transimpedance (dB-Ω)	46.88	56.66	20.1 %

4.3.3 Large Signal Simulations

The large signal simulations are presented in the form of transient responses and eye diagrams for the frequency range of 10 to 50 GHz (for schematics in Figures 3.26 and 3.28). Figure 4.11 depicts the input of the discrete receiver, while Figure 4.12 illustrates the input of the monolithic receiver.

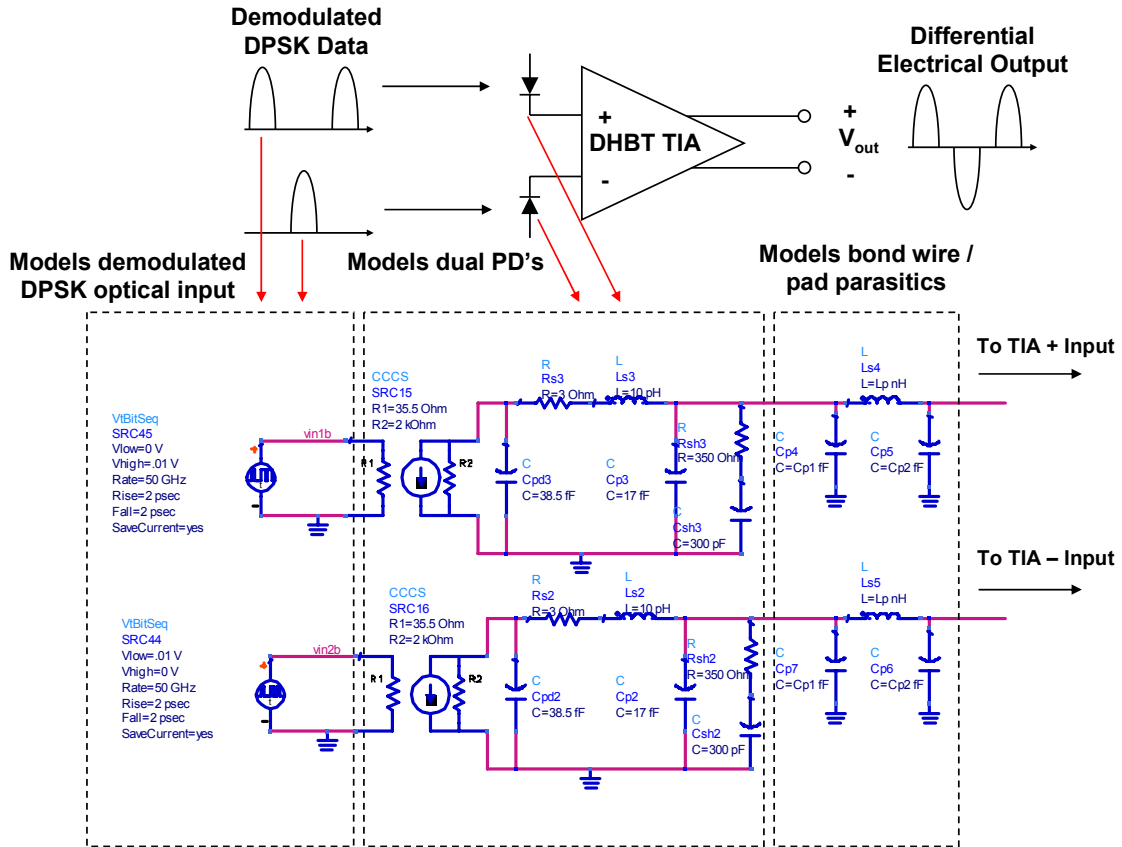


Figure 4.11: Transient analysis input for discrete integrated receiver

In Figure 4.11, the input to the TIA is split up into three blocks. The first block represents optical demodulated NRZ-DPSK signal as described in chapter 2. The second block of Figure 4.11 models the two off-chip balanced photodiodes. Finally, the third block models the parasitics of the bond wire and pad capacitances connecting the photodiodes to the TIA.

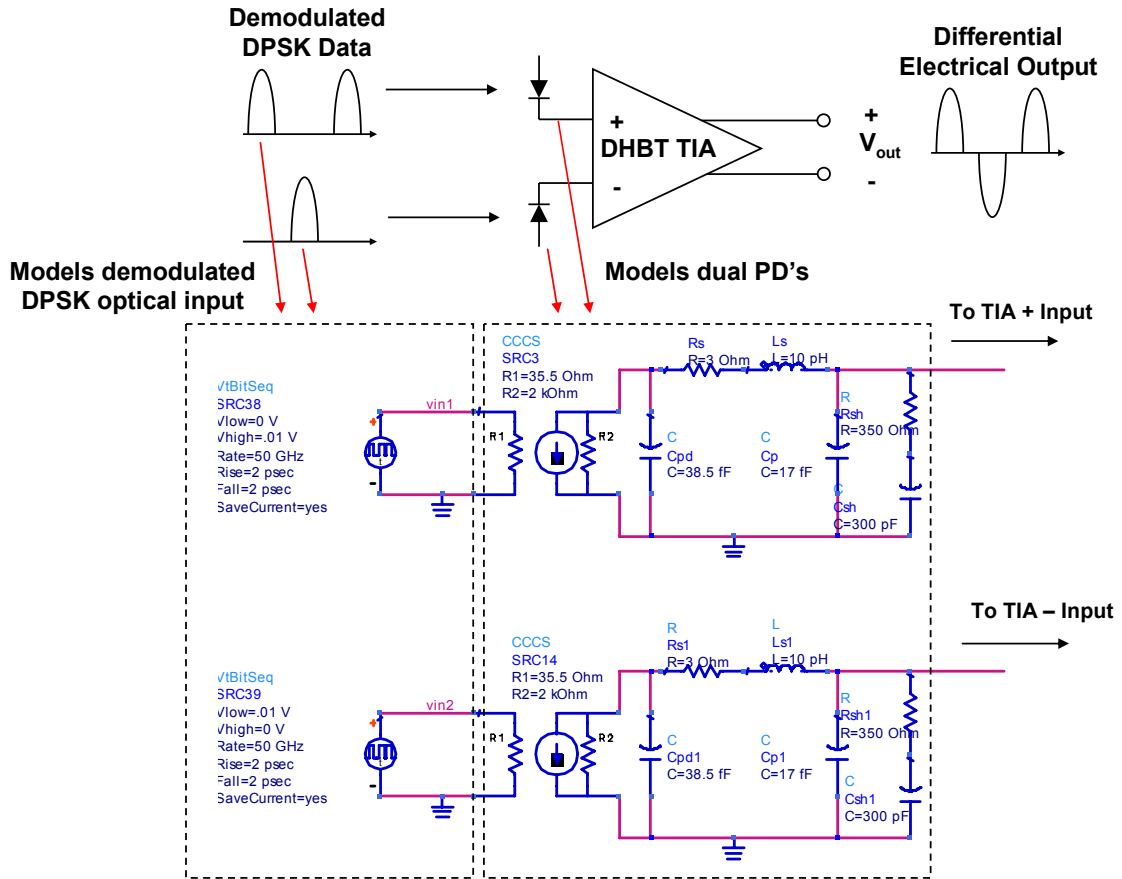


Figure 4.12: Transient analysis input for monolithically integrated receiver

In Figure 4.12, the input is identical to the discrete receiver input without the bond wire parasitics. Again, the first block models the optical demodulated NRZ-DPSK signal and the second block models the dual balanced photodiodes.

Figure 4.13 and 4.14 illustrate the single ended input voltage and differential output voltage of the receiver when driven with a 50 GHz differential input (PRBS) data stream. The driving voltage simulates the demodulated DPSK optical input into the photodiodes. The differential output voltage of the discrete receiver is approximately $0.6 V_{pp}$, while the differential output voltage of the monolithic receiver is approximately $0.2 V_{pp}$.

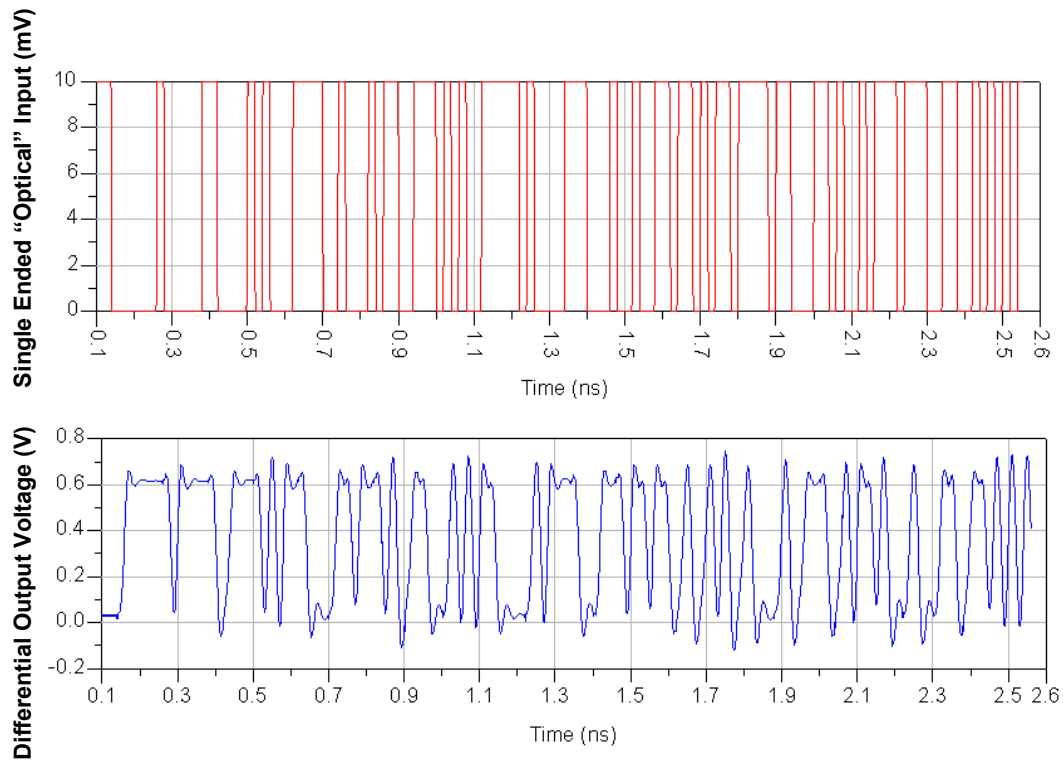


Figure 4.13: Discrete receiver transient input and output voltage at 50 GHz

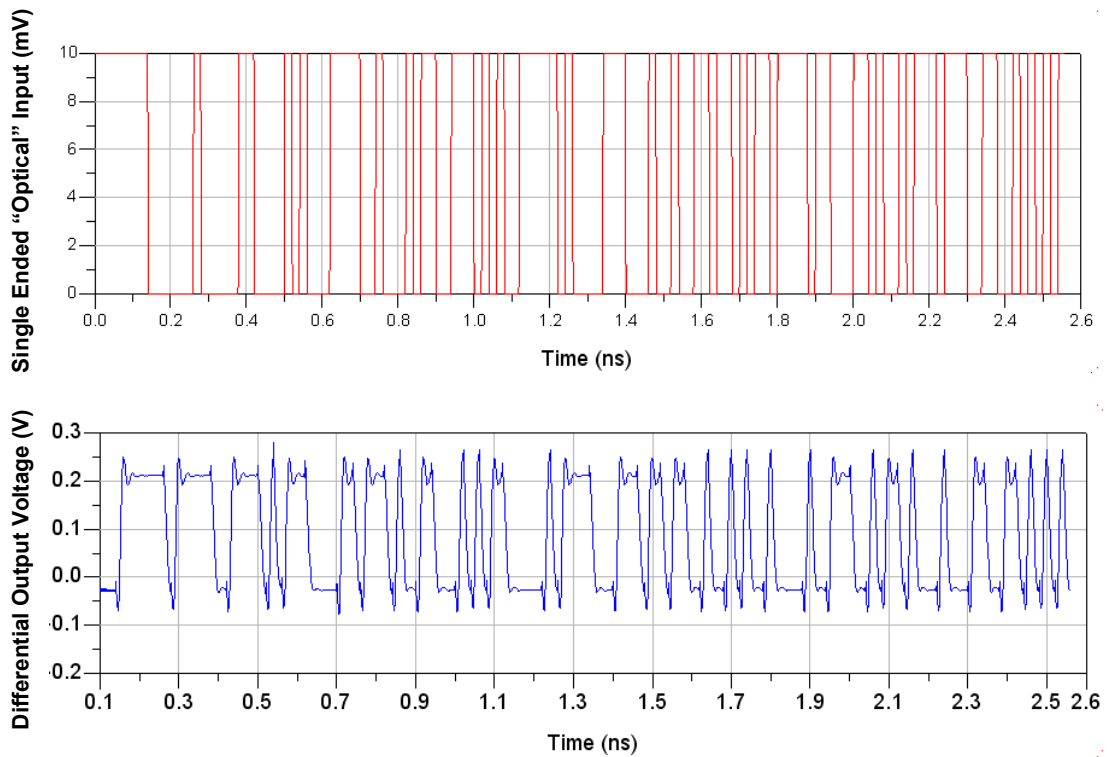
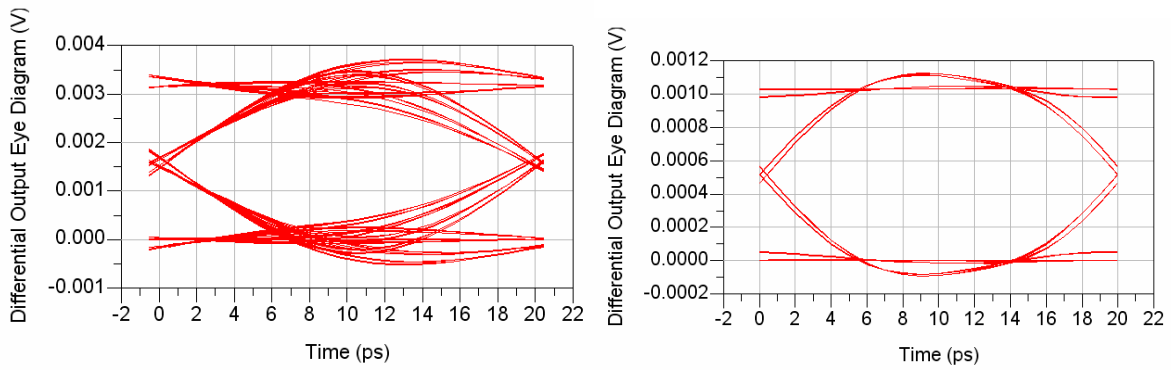


Figure 4.14: Monolithic receiver transient input and output voltage at 50 GHz

Two major differences can be noticed from Figure 4.14: the discrete receiver has a larger output voltage because of the higher gain (larger feedback resistance). However, the monolithic receiver has a cleaner output response due to its wider bandwidth.

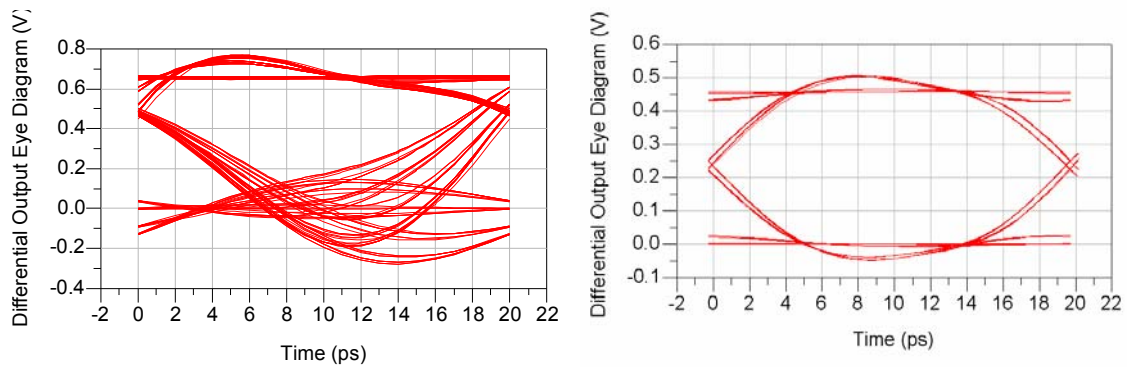
The effect of the bandwidth response can be seen on the eye diagrams. Figure 4.14 illustrates the output eye diagrams for both receivers when driven with the 50 GHz differential input data stream. With input voltages varying from 0.1 mV to 80 mV for the single ended case, Figure 4.15 illustrates the eye diagrams for both receivers: discrete (left) and monolithic (right).



Discrete Receiver

Monolithic Receiver

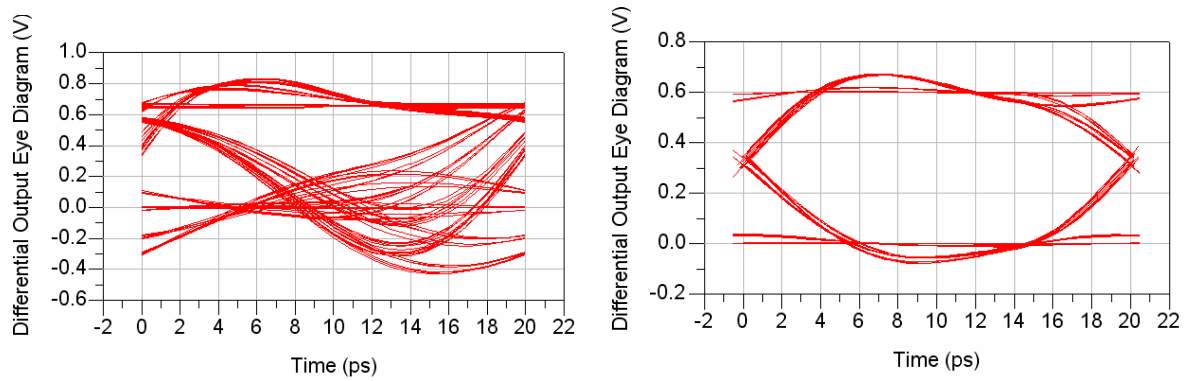
(a) 50 GHz – 0.1 mV single ended input



Discrete Receiver

Monolithic Receiver

(b) 50 GHz – 50 mV single ended input



Discrete Receiver

Monolithic Receiver

(c) 50 GHz – 80 mV single ended input

Figure 4.15: Differential output eye diagrams driven with various 50 GHz PRBS amplitudes

In all three cases of Figure 4.15, the eye diagrams are open for the monolithic receiver while the discrete suffers from inter-symbol interference. The superior performance is due to the larger bandwidth and less parasitics of the monolithically integrated receiver.

The output swings (vertical eye openings) of the monolithic receiver for the 0.1 mV, 50 mV, and 80 mV inputs are $0.001 V_{pp}$, $0.45 V_{pp}$, and $0.60 V_{pp}$, respectively. The receiver reached saturation when the input was 80 mV.

Optical dynamic range can be calculated for the monolithically integrated receiver. Figure 4.14 shows the smallest optical input value to be 0.1 mV while the largest is 80 mV. The smallest and largest optical input powers are calculated below.

$$OpticalPower_{\min} = \frac{(V_{\min} / 50)mA}{0.37 A/W} = 0.0054mW = -22.67 dBm \quad (4.8)$$

$$OpticalPower_{\max} = \frac{(V_{\max} / 50)}{0.37 A/W} = 4.3243mW = 6.36 dBm \quad (4.9)$$

Therefore, the dynamic range of the monolithic receiver is 29.03 dB. The simulated dynamic range can be compared to 10 dBm found in literature for a similar optical receiver with 40 GHz bandwidth [76]. Figure 4.16 plots the differential output eye amplitude versus the input optical power for the monolithic integrated receiver. This plot further illustrates the wide dynamic range of the receiver.

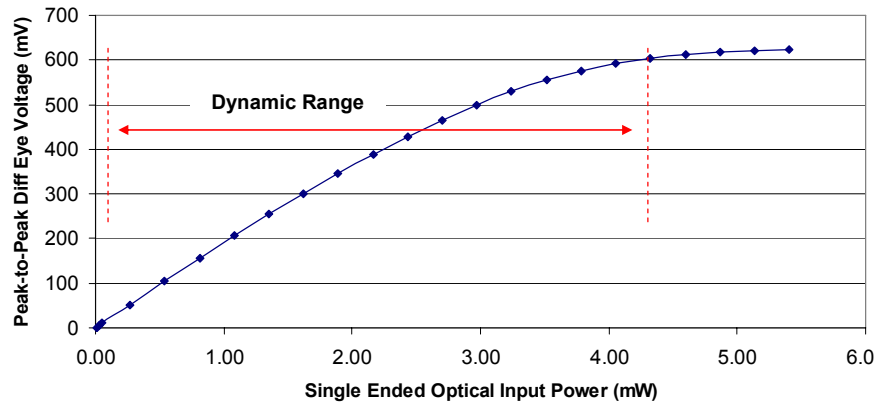


Figure 4.16: Differential output eye amplitude versus photocurrent

Lastly, Figure 4.17 illustrates the output eye diagram for the monolithically integrated receiver when driven with 10, 20, 30, and 40 GHz differential (PRBS) input data streams.

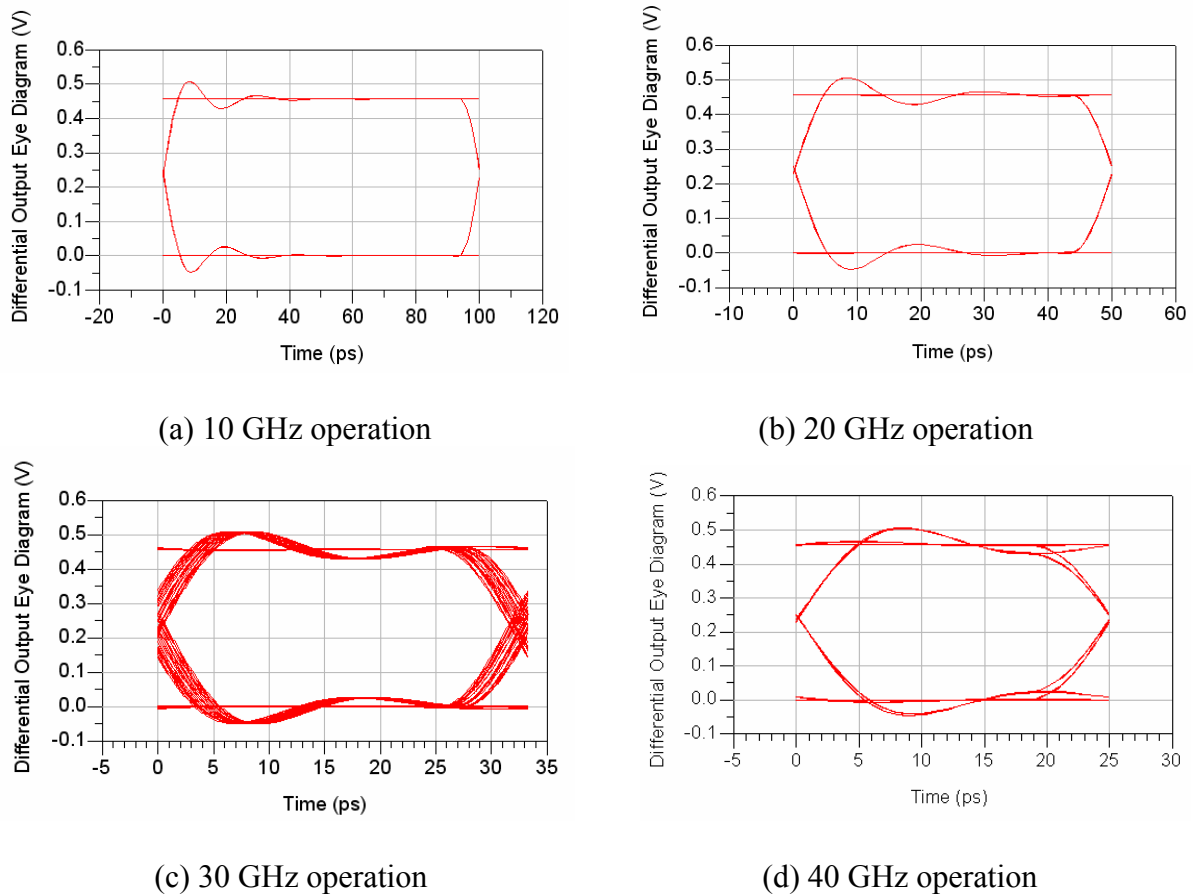


Figure 4.17: Differential output eye diagram of monolithic receiver when driven with optical input voltage of 50 mV

Figure 4.17 shows that the eye diagram remains open over a wide range of frequencies. The differential output amplitude remains at approximately $0.45 V_{pp}$ for all cases.

In summary, although the discrete receiver performed with transient responses equivalent to 50 GHz waveforms, the eye diagrams were not properly open at 50 GHz. On the other hand, the monolithic integrated receiver had a superior performance in the transient response, and open eye diagrams for wide input conditions at 50 GHz. Table 4.22 summarizes the simulation results.

Table 4.22: Large signal simulations for monolithically integrated receiver as compared to discrete receiver

Measurement	Monolithically Integrated Receiver	Discrete Receiver
Feedback Resistance	95 Ω	330 Ω
Gain S21	14.26 dB	24.04 dB
3-dB Bandwidth	50.01 GHz	30.31 GHz
Output eye amplitude with 0.05 V input	0.45 V	Closed
Clipped output eye amplitude	0.60 V	Closed
Input for clipped output eye	0.08 V	Closed
Dynamic Range	29 dB	--
Maximum data rate	50 Gb/s	30 Gb/s

5. NOISE ANALYSIS AND RESULTS

5.1 Noise Analysis

The noise analysis for the monolithic receiver is divided into three sections: photodiode noise, transistor noise, and transimpedance amplifier noise. The simulations were performed for the monolithic optical receiver schematic shown on Figure 3.28 with the design parameters contained in Table 4.9.

5.1.1 Photodiode Noise

The total output current of a photodiode is the sum of the photocurrent produced by the conversion of light into electrical energy and the noise currents of the photodiode. The three major sources of noise current include thermal noise, shot noise, and amplified spontaneous emission (ASE). Thermal noise is due to random electron motion caused by thermal effects in the photodiode, while shot noise is due to the random distribution of electrons generated by photo detection. Thermal noise directly adds to the photocurrent of the photodiode, while shot noise is a representation of photocurrent variance. Amplified spontaneous emission (ASE) is created by optical amplifiers found within a fiber optic communication system, is external to the optical receiver, and will not be considered in noise simulations [72].

Both types of photodiode noise – thermal and shot – are represented by a Gaussian random process. The thermal noise current is given by:

$$\overline{i_{thermal}} = \sqrt{\frac{4k_B T}{R}} \quad (5.1)$$

where k_B is the Boltzmann constant, T is the operating temperature (in Kelvin), and R is the device resistance. The units of $I_{thermal}$ are pA/\sqrt{Hz} . The thermal noise current is shown to have a variance of:

$$\sigma_{thermal}^2 = \overline{i_{thermal}^2} BW = \frac{4k_B T}{R} BW \quad (5.2)$$

where bandwidth is the electrical bandwidth of the photodiode. Shot noise current is expressed by:

$$\overline{i_{shot}} = \sqrt{2eI_{photo}} \quad (5.3)$$

where e is the electron charge and I_{photo} is the produced photocurrent. Again, the units of I_{shot} are pA/\sqrt{Hz} . Shot noise current has a variance of:

$$\sigma_{shot}^2 = \overline{i_{shot}^2} BW = 2eI_{photo} BW \quad (5.4)$$

Although the shot noise contributes to the overall noise in a photodiode, thermal noise tends to dominate in practical detectors [72]. Figure 5.1 illustrates the main noise sources incorporated into the small signal photodiode model. Here, the thermal noise current has been converted into its Thevenin equivalent voltage – $\overline{v_{thermal}^2} = 4k_b TRBW$. Note that only the series photodiode resistance has a noise source, as this contribution dominates the noise.

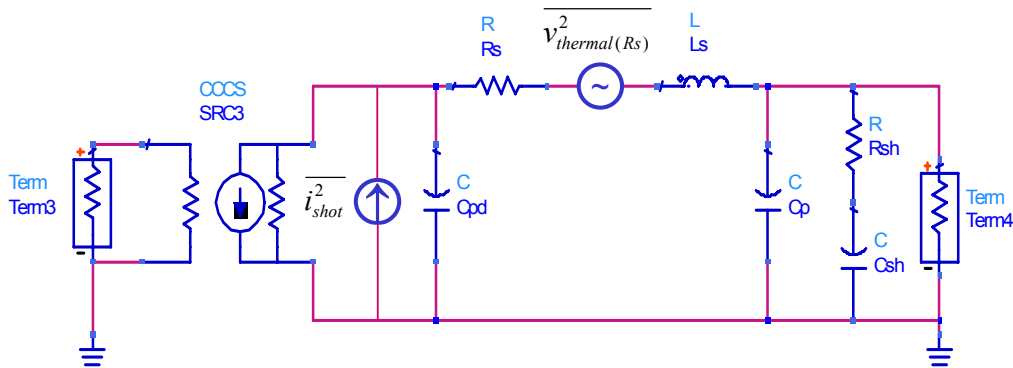


Figure 5.1: Photodiode small signal model with included noise sources

The total output current of a photodiode is the sum of the photocurrent and noise currents. This is depicted in equation 5.5.

$$I_{total} = I_{photo} + \overline{i_{shot}} + \overline{i_{thermal}} = I_{photo} + 2eI_{photo}BW + \frac{4k_B T}{R}BW \quad (5.5)$$

This output current, I_{total} , is a Gaussian random process with mean I_{photo} and variance:

$$\sigma^2 = \sigma_{shot}^2 + \sigma_{thermal}^2 \quad (5.6)$$

Equation 5.6 explains the noise limitations of the photodiode. Because shot noise and thermal noise are both proportional to bandwidth, the overall noise of the photodiode is also proportional to bandwidth. This proportionality comes with the realization of the noise / bandwidth tradeoff in the photodiode. As the bandwidth of the device increases, the noise also does. This is one of the fundamental limitations of the photodiode [72].

5.1.2 Transistor Noise

The major sources of noise in a transistor (HBT) include shot, thermal, flicker (1/f noise), and burst noises. These noise sources add to the transistor small signal model in Figure 3.3. Shot noise can be represented by adding a current source between corresponding nodes (parallel) in the HBT, while thermal noise can be represented by adding a voltage source in series with the corresponding resistance [27]. Noise sources are added to the small signal model as shown in Figure 5.2.

were presented in Figure 5.2. Although all resistances in the HBT model are sources of thermal noise (r_{bi} , r_{ci} , r_e , r_{bx} , and r_{cx}), the base resistance thermal noise (r_{bi} and r_{bx}) dominates [27]. Thermal noise sources are given below in equations 5.9-5.13. These noise voltages are placed in series with their corresponding resistances in the small signal model.

$$\overline{v_{rbi}^2} = 4k_B T(r_{bi})BW \quad (5.9)$$

$$\overline{v_{rci}^2} = 4k_B T(r_{ci})BW \quad (5.10)$$

$$\overline{v_{re}^2} = 4k_B T(r_e)BW \quad (5.11)$$

$$\overline{v_{rbx}^2} = 4k_B T(r_{bx})BW \quad (5.12)$$

$$\overline{v_{rcx}^2} = 4k_B T(r_{cx})BW \quad (5.13)$$

Other noise sources include flicker (1/f noise) and burst noise. Flicker noise is caused by the random capturing and releasing of carriers in traps associated with crystal defects (also impurities). Burst noise is better known as popcorn noise. The origins of popcorn noise are not well understood, but can be experimentally measured. Both flicker noise and burst noise are represented by current sources between the base and emitter nodes in parallel with the base shot noise current source. Therefore, these noise sources add together to give a total noise current of equation 5.14 in the base emitter region. In equation 5.14, the first term is the shot noise, the second term is the flicker noise, and the third term is the burst noise of the transistor.

$$\overline{i_b^2} = 2qI_B BW + K_F \frac{I_B^{A_F}}{f} BW + K_B \frac{I_B^{A_B}}{1 + \left(\frac{f}{f_B}\right)^2} BW \quad (5.14)$$

Here, K_F , K_B , A_F , and A_B are constants that are dependent upon the device characteristics. f_c is the frequency at which burst noise starts to take effect. These constants are only found

through experimental verifications [27]. Equation 5.14 shows again that as the bandwidth of the transistor increases, so does the noise.

At high frequencies, flicker noise and burst noise quickly diminish in the HBT. However, thermal and shot noises dominate. At lower frequencies, flicker noise dramatically increases and dominates over all other noise types [27]. This can be seen in Figure 5.3 where the total input noise has been plotted against frequency for the altered HBT model as defined in chapter 3. Here, K_F , K_B , A_F , and A_B were set to 1.0.

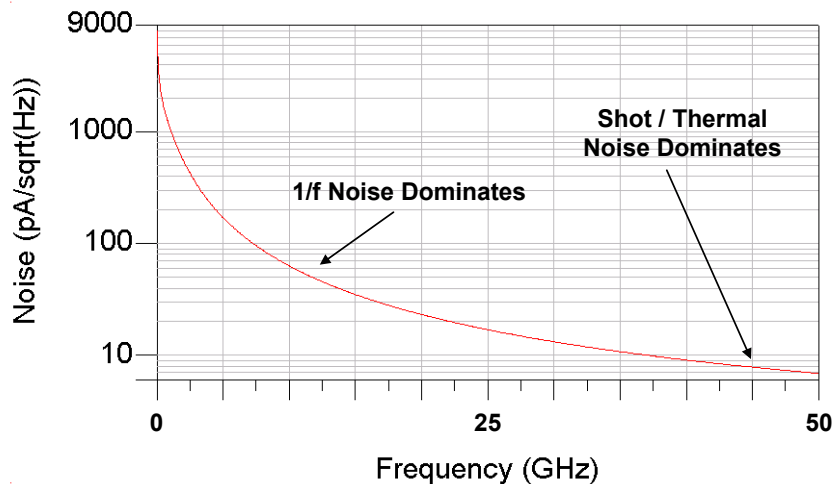


Figure 5.3: Noise versus frequency for a single HBT. $V_{CE} = 1.2$ V, $I_C = 13$ mA

5.1.3 Transimpedance Amplifier Noise

Now that the noise sources of the photodiode and the HBT have been identified, the total noise of the TIA should be determined. Two common figures of merit include input referred noise and noise figure. Because noise calculations become quite convoluted for the entire TIA design, the input referred noise and noise figure of the receiver will be found through simulations in section 5.2. This section of the report gives approximate expressions for both figures so some qualitative conclusions can be made about designing for optimum noise performance.

Input referred noise is defined as the minimum input current needed to give a specified bit-error-rate value. This value is quite important; in that reducing the input referred noise leads to relaxed system specifications. Knowing that the noise of the first stage of the TIA dominates the total noise performance, the single-ended input referred current noise is approximated in equation 5.15 [36].

$$\frac{d}{df} \overline{i_{in}^2} = 2qI_{C,Q_m} \left[\frac{1}{\beta} + \frac{1}{(g_{m,Q_m} R_f)^2} + \left(\frac{2\pi f (C_{PD} + C_{in})}{g_{m,Q_m}} \right)^2 \right] \quad (5.15)$$

where Q_{in} represents the input transistor of one side of the TIA. C_{PD} and C_{in} are the photodiode and TIA input capacitances, respectively. Two very important qualitative arguments can be made from equation 5.15. First, as TIA frequency operation increases, noise also increases. Secondly, as feedback resistance increases, noise decreases (by R_F^2) until the $1/R_F^2$ term becomes small. These arguments should be taken into account for TIA design considerations. TIA input referred current noise is plotted against feedback resistance for the monolithic optical receiver of Figure 3.34 below. The simulation was performed by varying feedback resistance at 50 GHz operation with all other parameter values (in Table 3.16) held constant.

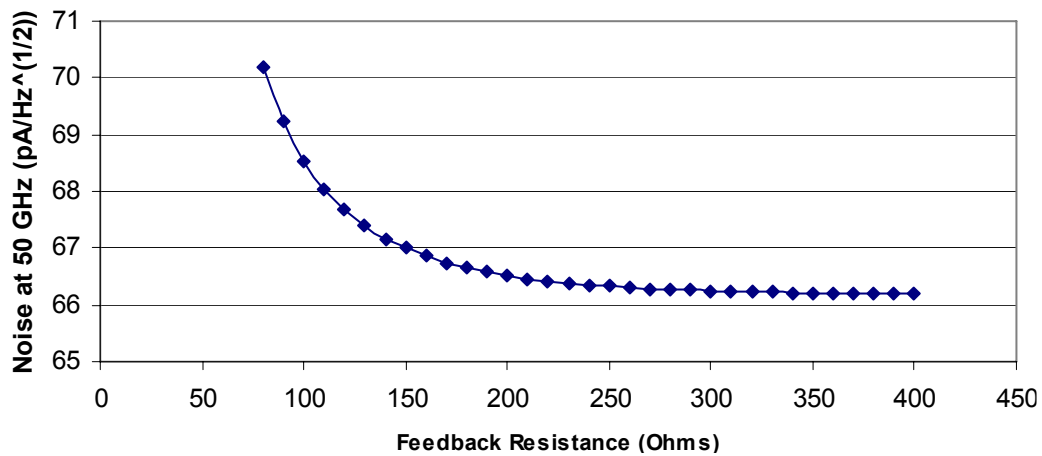


Figure 5.4: Input referred noise versus feedback resistance. $V_{bias} = 5V$

As recalled from chapter 3, as the feedback resistance increases, the gain increases and the bandwidth becomes narrower (refer to Figure 3.24). In addition to the gain bandwidth product tradeoff, a noise bandwidth tradeoff also exists. The major design tradeoffs are listed in equations 5.16 and 5.17. As the feedback resistance increases, the gain increases but the bandwidth will decrease linearly, while the noise decreases not linearly but by R_F^2 (with all other parameters fixed) until the $1/R_F^2$ term becomes small [36].

$$\uparrow R_F \Rightarrow \uparrow \text{Gain}, \downarrow \text{BW}, \downarrow \text{Noise} \quad (5.16)$$

$$\downarrow R_F \Rightarrow \downarrow \text{Gain}, \uparrow \text{BW}, \uparrow \text{Noise} \quad (5.17)$$

In addition to the input referred noise, another figure of merit for the optical receiver is the noise figure (NF). It is the relation of the signal to noise ratio (SNR) of the input to the signal to noise ratio (SNR) of the output:

$$NF = \frac{SNR_{in}}{SNR_{out}} = NF_{\min} + \frac{4r_n |\Gamma_{src} - \Gamma_{opt}|^2}{(1 - |\Gamma_{src}|^2) |1 + \Gamma_{opt}|} \quad (5.18)$$

where NF_{\min} is the minimum NF possible, r_n is the noise resistance of the amplifier, Γ_{src} is the source impedance, and Γ_{opt} is the optimum impedance for minimum noise when matched to a 50 Ω termination. When an amplifier is well matched to a load, $\Gamma_{src} \approx \Gamma_{opt}$ and the actual NF is equal to the minimum NF. In a cascade amplifier, such as in the present case of the TIA under study, the first stage NF dominates [71]. This can be shown:

$$NF_{cascade} = NF_1 + \frac{1}{Gain_1} (NF_2 - 1) + \dots \quad (5.19)$$

The simulation results for input referred noise and noise figure of the monolithic optical receiver will be presented in section 5.2.

5.2 Noise Results

The simulation results for the noise analysis of the monolithic optical receiver were performed with the schematic of Figure 3.28 at a temperature of 290 K (IEEE definition of noise figure measurement). It should also be noted that flicker and burst noise were ignored for the simulations in this section, as flicker and burst noise require experimental testing to determine noise coefficients. This is a reasonable approximation, considering that the optical receiver operates at very high frequencies. The noise simulation results can be split up into three sections: 3-dB noise versus bandwidth, 3-dB noise versus bias, and noise figure results.

5.2.1 3-dB Noise versus Bandwidth

There exists a tradeoff between noise and bandwidth in the monolithic optical receiver and to simulate this tradeoff, the receiver's design parameters were modified and optimized to obtain specifically 10, 20, 30, 40, and 50 GHz bandwidths. Table 5.1 lists the parameter values corresponding to the lowest noise operation at each particular bandwidth.

Table 5.1: Monolithic optical receiver parameter values for minimum noise

Name	50 GHz	40 Ghz	30 Ghz	20 Ghz	10 GHz
Electrical BW (GHz)	47.34	39.41	30.37	20.72	9.40
Gain (dB)	11.44	14.27	17.88	19.79	23.20
Input referred noise (pA/ $\sqrt{\text{Hz}}$)	64.93	49.56	34.48	25.36	16.96
Feedback (Ω)	95	135	235	340	740
R1 (Ω)	45	50	75	75	85
R2 (Ω)	45	55	60	60	60
Rsupply (Ω)	480	580	760	870	1170
Bias Current per device (mA)	7.39	6.15	4.81	4.205	3.05

Figure 5.5 plots the input referred noise in pA/ $\sqrt{\text{Hz}}$ against bandwidth for the five different cases presented in Table 5.1. The input noise was measured at the 3-dB frequency for each case.

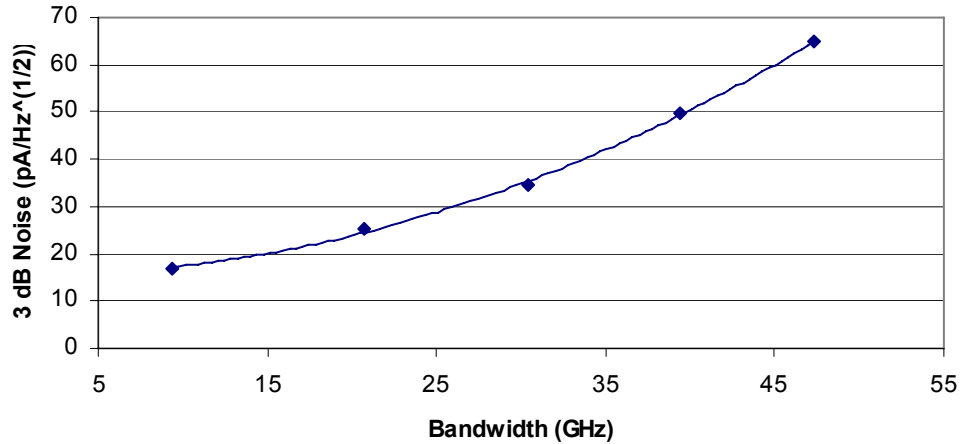


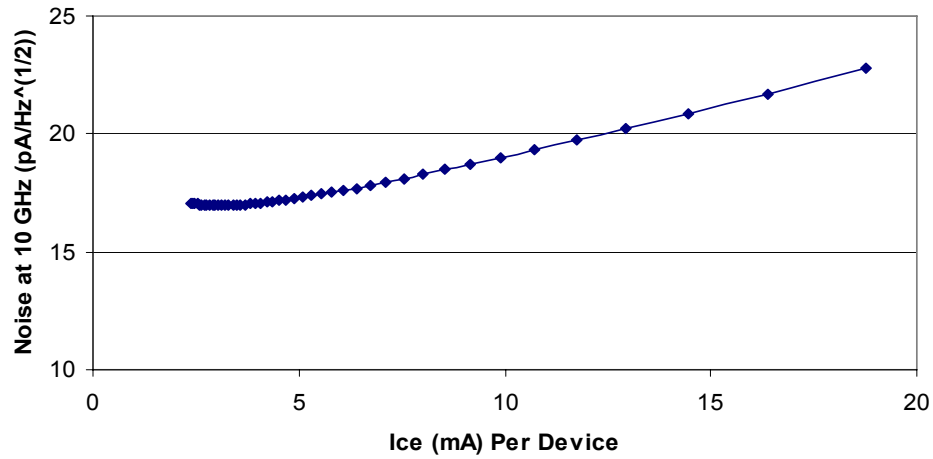
Figure 5.5: Minimum input referred noise versus electrical bandwidth for the monolithic optical receiver

Figure 5.5 shows the tradeoff between electrical bandwidth and noise. The noise values found in these simulations are comparable to those found in literature for a similar TIA circuit with a 47 GHz bandwidth [92]. The input referred current noise for an InP HBT differential TIA is measured to be $25 \text{ pA}/\sqrt{\text{Hz}}$ for 10 GHz operation and $40 \text{ pA}/\sqrt{\text{Hz}}$ for 40 GHz operation in [92]. This is quite comparable to the $25 \text{ pA}/\sqrt{\text{Hz}}$ (10 GHz) and $50 \text{ pA}/\sqrt{\text{Hz}}$ (40 GHz) found in simulations again proving that the monolithic optical receiver is a quality design.

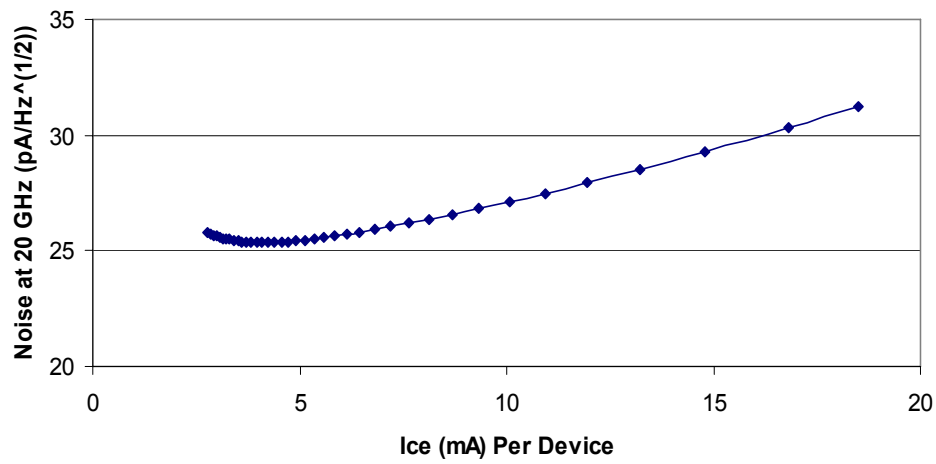
5.2.2 3-dB Noise versus bias

In order to achieve the minimum noise for a particular frequency, as was done in the section 5.2.1, the bias current of the TIA had to be optimized. To do this, plots were made of input referred noise versus DC bias current for 10, 20, 30, 40 and 50 GHz bandwidth designs presented in Table 5.1. Input referred noise of the monolithic receiver was measured while varying HBT bias current and holding all other parameters constant (in Table 5.1). Results of these simulations are presented below in Figure 5.6.

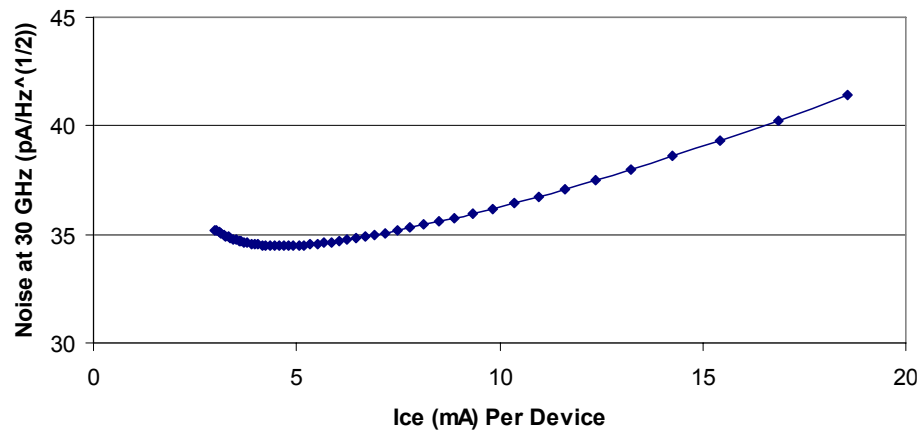
Figure 5.6: Input referred noise versus bias current



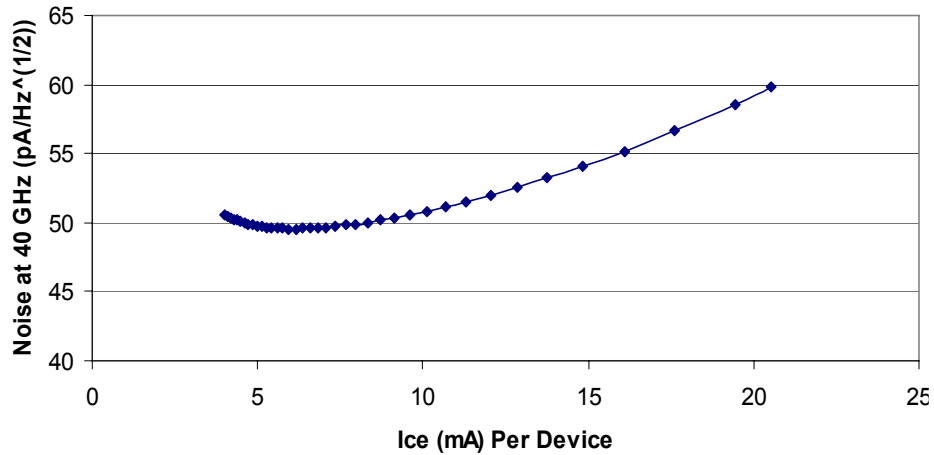
(a) Monolithic optical receiver electrical BW = 10 GHz



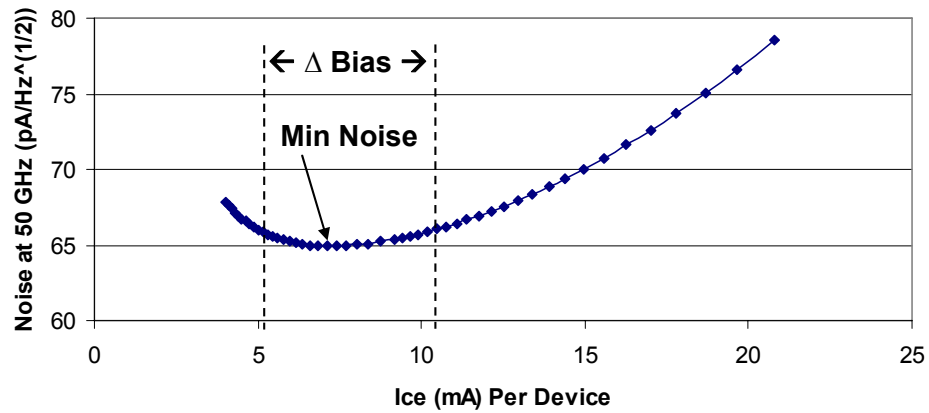
(b) Monolithic optical receiver electrical BW = 20 GHz



(c) Monolithic optical receiver electrical BW = 30 GHz



(d) Monolithic optical receiver electrical BW = 40 GHz



(e) Monolithic optical receiver electrical BW = 50 GHz

As Figure 5.6 shows, there is a distinct noise minimum for each operation frequency which spans over a small range of bias current. The bias current for each noise minimum is listed in Table 5.2 along with the corresponding Δ bias current. Δ bias current is defined as range of bias that keeps the amplifier to within $\pm 1 \text{ pA} / \sqrt{\text{Hz}}$ of the noise minimum. While values were visually illustrated in Figure 5.6e for the 50 GHz case, results for all cases are presented below.

Table 5.2: Bias current / Δ bias needed to stay within $\pm 1 \text{ pA} / \sqrt{\text{Hz}}$ of the noise minimum

Bandwidth (GHz)	Minimum Noise (pA / $\sqrt{\text{Hz}}$)	Bias Current for Minimum Noise (mA)	Δ bias to stay within $\pm 1 \text{ pA} / \sqrt{\text{Hz}}$ (mA)
47.34	64.933	7.39	5.04
39.41	49.59	6.15	5.05
30.37	34.48	4.67	5.15
20.72	25.36	4.10	5.35
9.40	16.96	3.05	5.65

Table 5.2 shows that as long as the bias current stays within approximately $\pm 2.5 \text{ mA}$ of the noise minimum, very low noise can be achieved. Beyond the $\pm 2.5 \text{ mA}$, noise starts to steadily increase.

In addition to plotting 3-dB noise versus bandwidth and bias current, 3-dB noise can also be plotted versus frequency for the 50 GHz monolithic optical receiver design presented in chapter 3 and 4. This plot is different than the noise versus bandwidth plot in that all variables were held constant (from Table 3.16) as frequency was swept and noise was measured.

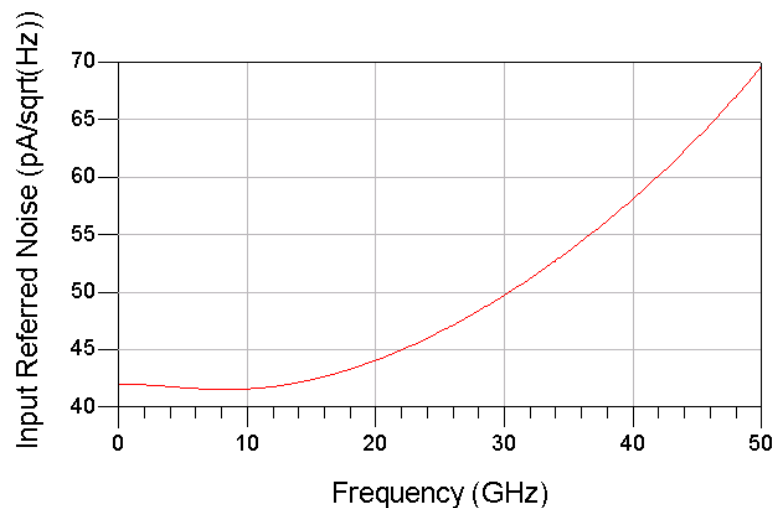


Figure 5.7: Input referred noise versus frequency for 50 GHz monolithic optical receiver design (schematic in Figure 3.28, parameters in Table 3.16)

Figure 5.7 shows that the input referred noise decreases with frequency operation for a receiver with a constant bandwidth. Therefore, receiver performance improves for lower bit rate systems using the same optical receiver.

5.2.3 Noise Figure

The final set of noise simulations includes the noise figure plots for the monolithic optical receiver. Figure 5.8 presents the plots for the noise figure (NF) and minimum NF versus frequency for the 50 GHz monolithic optical receiver design (schematic in Figure 3.28, parameters in Table 3.16).

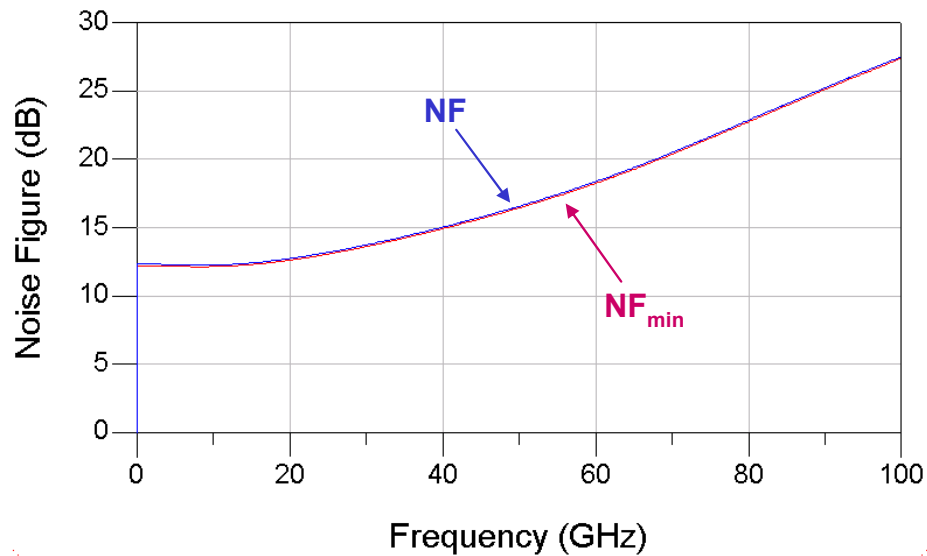


Figure 5.8: Noise figure versus frequency for 50 GHz monolithic optical receiver design (schematic in Figure 3.28, parameters in Table 3.16)

This plot shows that the noise figure is approximately equal to the minimum noise figure for all frequencies. Based on equation 5.18, it can be concluded that $\Gamma_{src} \approx \Gamma_{opt}$ and the amplifier is well matched to the 50 Ω terminations.

The noise figure at the 3-dB frequency was determined for the five different receiver bandwidth cases presented in Table 5.1. This allows for a noise figure versus bandwidth

comparison. Results are presented below in Table 5.3. Again, all design parameters were set as detailed in Table 5.1.

Table 5.3: NF results of monolithic optical receiver optimized for different electrical BWs

Name	50 GHz	40 GHz	30 GHz	20 GHz	10 GHz
Electrical BW (GHz)	47.34	39.41	30.37	20.72	9.40
Gain (dB)	11.44	14.27	17.88	19.79	23.20
Noise Figure (dB)	15.61	13.77	11.14	9.07	6.55

The results of Table 5.3 have been plotted in below in Figure 5.9. This plot further emphasizes the tradeoff between electrical bandwidth and noise.

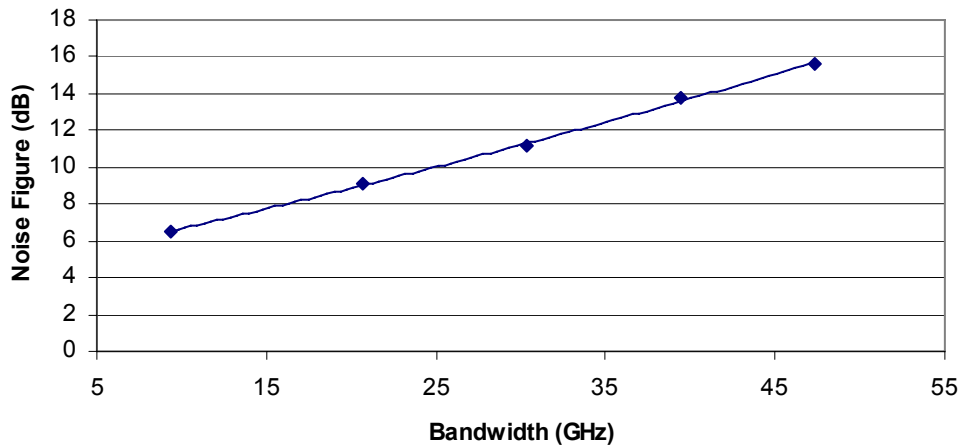


Figure 5.9: NF versus electrical bandwidth for the monolithic optical receiver

6. CONCLUSIONS AND FUTURE WORK

This thesis focused on the design, analysis, and simulation of a 1.55 μm monolithic optical receiver consisting of two balanced waveguide photodiodes integrated with a differential transimpedance amplifier, based on InP double heterojunction bipolar technology for a 50 GHz differential phase shift keying system. The goals of the design included: high amplifier gain and wide bandwidth, 50 Ω impedance matching, smooth transient response, open eye diagrams at 50 Gb/s, a large optical dynamic range, low power dissipation with a single 5V supply, low device operating temperature, and low noise operation.

A small signal equivalent model based upon the Gummel-Poon BJT model was developed for the InP / InGaAs double-heterojunction bipolar transistor (DHBT) for use in circuit simulations [108-109]. The DHBT model was determined by fitting to measured S-parameters for a 180 nm collector base-metal-overlaid structure (BMOSA) with 20 μm^2 hexagonal emitter [59]. In addition, a thermal model was incorporated to estimate the device operating temperatures [109]. Results showed the DHBT model S-parameters agree with the measured ones over a wide frequency range. However, the large signal model was limited in accuracy because no large signal measured data was published in [59]. The maximum transition frequency and frequency of oscillation of the model used in simulation were 289 and 210 GHz, respectively.

A small signal equivalent model was developed for the InGaAs PIN waveguide photodiode (PIN-WGPD) based upon data from [60]. The PIN-WGPD model parameters were found by fitting the photodiode gain profile to measured results for a 300 nm thick evanescently waveguide coupled PIN-PD with a total area of 5x20 μm^2 [88]. The fitted results agreed well with the measured ones over the entire frequency range of 0–50 GHz. The

bandwidth of the model used in the simulation was 70 GHz and a responsivity value of 0.37 A/W was assumed [88].

After the model parameters were found for both the transistor and photodiode, a fully differential 3-stage transimpedance amplifier was designed and optimized. Bias conditions and design variables were defined based on the gain, bandwidth, and noise tradeoffs of the amplifier within the amplifier specifications (Table 4.1). After optimizations, the transimpedance amplifier exhibited a gain of 18.8 dB, bandwidth of 50.3 GHz, transimpedance of 50.9 dB- Ω , and input and output reflection of better than -10 dB. Large signal simulations showed the eye diagram to be open at 50 Gb/s with a large optical dynamic range of 28.8 dB. DC simulations indicated that all devices operated at a temperature of less than 144°C while the power dissipation was less than 305 mW. The simulation results were compared to measured ones found for similar amplifiers [91].

Finally, it was shown that the monolithic optical receiver outperformed the hybrid one in terms of bandwidth and transient performance. After being optimized, the hybrid receiver exhibited a gain of 24.0 dB and a bandwidth of 30.3 GHz, while the monolithic receiver showed a gain of 14.3 dB and bandwidth of 50.0 GHz. Both receivers had input and output reflections better than -10 dB at 50 GHz. However, eye diagram simulations showed that only the monolithic receiver could perform at 50 Gb/s in DPSK format with a optical dynamic range of 29.0 dB. Noise analysis on the monolithic optical receiver showed the receiver to have an input referred current noise of less than $65 \text{ pA} / \sqrt{\text{Hz}}$ at a 50 GHz bandwidth. These results are comparable to those found in literature [92].

Future work of this project includes investigating the use of other devices and material systems for the fabrication of the optical receivers. Possible options include

BiCMOS SiGe transistors. The choice of devices and materials would be based upon the availability of an outside foundry to fabricate the devices.

Other possibilities for future work include using a light wave simulator to simulate the optical properties of the receiver. In addition, programs such as SUPREM can be used for semiconductor doping profiles and PISCES for electrical simulations of the processed devices.

7. LIST OF REFERENCES

- [1] Agrawal, G. “Nonlinear Fiber Optics”. Third Edition. Academic Press. 2001.
- [2] Akatsu, Y., Miyagawa, Y., Miyamoto, Y., Kobayashi, Y., Akahori, Y. “A 10 Gb/s High Sensitivity, Monolithically Integrated p-i-n-HEMT Optical Receiver”. IEEE Photonics Technology Letters, Vol. 5, Issue 2. pp. 163-165. Feb, 1993.
- [3] Amann, M.C., Buus, J. “Tunable Laser Diodes”. Artech House. 1998.
- [4] Bondurant, R.S., Atia, W.A. “Demonstration of Return-to-zero Signaling in Both OOK and DPSK Formats to Improve Receiver Sensitivity in an Optically Preamplified Receiver”. IEEE Lasers and Electro-Optics Society 1999 12th Annual Meeting, Vol. 1. pp. 226-227. Nov, 1999.
- [5] Bousselet, P., Simonneau, C., Bayart, D., Salet, P., Lucas-Leclin, G., Roger, G., Georges, P., Auzanneau, S.C., Michel, N., Calligaro, M., Parillaud, O., Lecomte, M., Krakowski, M. “EDFAs with Improved Gain-flatness Owing to a New Pump Design”. 2005 Optical Fiber Communication Conference, Technical Digest, Vol. 4. March, 2005.
- [6] Bowers, J. E., Burrus, Jr., C. A. “Ultrawide-Band Long-Wavelength P-I-N Photodetectors”. Journal of Lightwave Technology, Vol. LT-5, No. 10. pp 1339-1350. Oct, 1987.
- [7] Boyd, R. W. “Nonlinear Optics”. Second Edition. Academic Press. 2002.
- [8] Buchali, F., Bulow, H. “Adaptive PMD Compensation by Electrical and Optical Techniques”. Journal of Lightwave Technology, Vol. 22, Issue 4. pp. 1116 – 1126. April, 2004.
- [9] Cai, J.X., Davidson, C.R., Foursa, D.G., Liu, L., Cai, Y., Bakhshi, B., Mohs, G., Patterson, W.W., Corbett, P.C., Lucero, A.J., Anderson, W., Li, H., Nissov, M., Pilipetskii, A.N., Bergano, N.S. “Experimental Comparison of the RZ-DPSK and NRZ-DPSK Modulation Formats”. Optical Fiber Communication Conference, 2005, Vol. 4. March, 2005.
- [10] Caruth, D., Shen, S.C., Chan, D., Feng, M., Schutt-Aine, J. “A 40 Gb/s Integrated Differential PIN+TIA with DC Offset Control Using InP SHBT Technology”. 2002 24th Annual Gallium Arsenide Integrated Circuit (GaAs IC) Symposium. pp. 59-62. Oct, 2002.
- [11] Chung, H.S., Lee, M.S., Lee, D., Park, N., DiGiovanni, D.J. “Low Noise, High Efficiency L-band EDFA with 980 nm Pumping”. Electronics Letters, Vol. 35, Issue 13. pp. 1099-1100. June, 1999.
- [12] Ciaramella, E., Contestabile, G., D'Errico, A. “A Novel Scheme to Detect Optical DPSK Signals”. IEEE Photonics Technology Letters, Vol. 16, Issue 9. pp. 2138 – 2140. Sept, 2004.

- [13] Clesca, B., Ronarc'h, D., Bayart, D., Sorel, Y., Hamon, L., Guibert, M., Beylat, J.L., Kerdiles, J.F., Semenkoff, M. "Gain Flatness Comparison Between Erbium-doped Fluoride and Silica Fiber Amplifiers with Wavelength-multiplexed Signals". IEEE Photonics Technology, Vol. 6, Issue 4. pp. 509-512. April, 1994.
- [14] Coldren, L.A., Fish, G.A., Akulova, Y., Barton, J.S., Johansson, L., Coldren, C.W. "Tunable Semiconductor Lasers: A Tutorial". Journal of Lightwave Technology, Vol. 22, Issue 1. pp. 193-202. Jan, 2004.
- [15] Curtice, W.R., Hietala, V.M, Gebara, E., Laskar, J. "The Thermal Gain Effect in GaAs-Based HBTs". International Microwave Symposium Digest. Pp. 639-641. June, 2003.
- [16] Dally, W. J., Poulton, J. W. "Digital Systems Engineering". Cambridge University Press. 1998.
- [17] Das, M.B., Chen, J., John, E. "Designing Optoelectronic Integrated Circuit (OEIC) Receivers for High Sensitivity and Maximally Flat Frequency Response". Journal of Lightwave Technology, Vol. 13, Issue 9. pp. 1876-1884. Sept, 1995.
- [18] Debregeas-Sillard, H., Vuong, A., Delorme, F., David, J., Allard, V., Bodere, A., LeGouezigou, O., Gaborit, F., Rotte, J., Goiz, M., Voiriot, V., Jacquet, J. "DBR Module with 20 mW constant coupled output power, over 16 nm (40 x 50 GHz spaced channels)". IEEE Photonics Technology Letters., Vol. 12. pp. 4-6. Jan, 2001.
- [19] Delorme, F., Alibert, G., Boulet, P., Grosmaire, S., Slempek, S., Ougazzaden, A. "High Reliability of High-Power and Widely Tunable 1.55- μ m Distributed Bragg Reflector Lasers for WDM Applications". IEEE Journal of Selected Topics in Quantum Electronics, Vol. 3, No. 2. pp. 607-614. April, 1997.
- [20] Delorme, F., "Widely Tunable 1.55- μ m Lasers for Wavelength-Division-Multiplexed Optical Fiber Communications". IEEE Journal of Quantum Electronics, Vol. 34, No. 9, pp.1706-1716. Sept, 1998.
- [21] Droge, E., Bottcher, E.H., Kollakowski, S., Strittmatter, A., Bimberg, D., Reimann, O., Steingruber, R. "78 GHz Distributed InGaAs MSM Photodetector". Electronics Letters, Vol. 34, Issue 23. pp. 2241-2243. Nov, 1998.
- [22] Fukuyama, H., Sano, K., Murata, K., Kitabayashi, H., Yamane, Y., Enoki, T., Sugahara, H. "Photoreceiver Module Using an InP HEMT Transimpedance Amplifier for Over 40 gb/s". IEEE Journal of Solid-State Circuits, Vol. 39, Issue 10. pp. 1690-1696. Oct, 2004.
- [23] Gnauck, A.H., Chandrasekhar, S., Leuthold, J., Stulz, L. "Demonstration of 42.7-Gb/s DPSK Receiver with 45 Photons/bit Sensitivity". IEEE Photonics Technology Letters, Vol. 15, Issue 1. pp. 99-101. Jan, 2003.

- [24] Gnauck, A.H., Winzer, P.J. "Optical phase-shift-keyed Transmission". IEEE Journal of Lightwave Technology, Vol. 23, Issue 1. pp. 115-130. Jan, 2005.
- [25] Godfrey, L. A. "Designing for the Fastest Response Ever". Optical Spectra. Oct, 1979.
- [26] Govindarajan, M., Forrest, S.R. "Design Considerations for Wide-band p-i-n/HBT Monolithic Transimpedance Optical Receivers". Journal of Lightwave Technology, Vol. 11, Issue 2. pp. 367-378. Feb, 1993.
- [27] Gray, P.R., Hurst, P.J., Lewis, S.H., Meyer, R.G. "Analysis and Design of Analog Integrated Circuits". John Wiley and Sons Inc. 2001.
- [28] Griffith, Z., Rodwell, M. J.W. "InGaAs/InP DHBTs With 120-nm Collector Having Simultaneously High f_t , f_{max} 450 GHz". IEEE Electron Device Letters, Vol. 26, No. 8. August, 2005.
- [29] Harrison, I., Dahlstrom, M., Krishnan, S., Griffith, Z., Kim, Y.M., Rodwell, M.J.W. "Thermal Limitations of InP HBTs in 80- and 160-Gb ICs". IEEE Transactions on Electron Devices, Vol. 51, Issue 4. pp. 529-534. April, 2004.
- [30] Haruna, T., Kakup, M., Ishikawa, S., Mouri, T., Ueno, M., Murata, T., Morinaga, K. "Gain-flatness Improvement Over C-band Employing Silica-based Borate / Alumina-codoped EDFA". Optical Fiber Communication Conference, 2005, Vol. 4. March, 2005.
- [31] Heather, S., Edwards, M., Woodfin, A. "Standard Single-Mode Fiber Upgrades to Full-Spectrum and G.652.D" Corning Optical Fiber WP3718, ISO 9001. 2004.
- [32] Iizuka, K. "Elements of Photonics in Free Space and Special Media". Wiley and Sons. 2002.
- [33] Imoto, N., Kawana, A., Machida, S., Tsuchiya, H. "Characteristics of Dispersion Free Single-mode Fiber in the 1.5 μm Wavelength Region". IEEE Journal of Quantum Electronics, Vol. 16, Issue 10. pp. 1052-1058. Oct, 1980.
- [34] Itzler, M.A. Suzanne, K.K.L. McCoy, S. Codd, N. "High-performance, Manufacturable Avalanche Photodiodes for 10 Gb/s Optical Receivers". 2000 Optical Fiber Communication Conference, Vol. 4. pp. 126-128. March, 2000.
- [35] Jiang, Q., Liu, X., Wang, Q., Feng, X. "Dynamic gain control in the serial structure C+L wide-band EDFA". IEEE Photonics Technology Letters, Vol. 16, Issue 1. pp. 87-89. Jan, 2004.
- [36] Kaminow, I., Li, T. "Optical Fiber Telecommunications: IVA Components". Academic Press. 2003.

- [37] Kamitsuna, H., Matsuoka, Y., Yamahata, S., Shigekawa, N. "Ultrahigh-speed InP/InGaAs DHPTs for OEMMICs". IEEE Transactions on Microwave Theory and Techniques, Vol. 49, Issue 10, Part 2. pp. 1921-1925. Oct, 2001.
- [38] Kasper, B. L. "Optical Fiber Telecommunications IV". Academic Press. 2002.
- [39] Kato, K. "Ultrawide-Band/High-Frequency Photodetectors". IEEE Transactions on Microwave Theory and Techniques, Vol. 47, No. 7. pp 1265-1281. July, 1999.
- [40] Keck, D. "Fundamentals of Optical Waveguide Fibers". IEEE Communications Magazine, Vol. 23, Issue 5. pp. 17-22. May, 1985.
- [41] Keiser, G. "Optical Fiber Communications". Third Edition. McGraw-Hill Companies, Inc. 2000.
- [42] Kim, H., Gnauck, A.H. "Experimental Investigation of the Performance Limitation of DPSK Systems Due to Nonlinear Phase Noise". IEEE Photonics Technology Letters, Vol. 15, Issue 2. pp. 320-322. Feb, 2003.
- [43] Kim, H. "Cross-phase-modulation-induced Nonlinear Phase Noise in WDM Direct-detection DPSK Systems". Journal of Lightwave Technology, Vol. 21, No. 8. pp. 1770-1774. Aug, 2003.
- [44] Kolbas, R. M. "ECE 723 Optical Properties of Semiconductors Lecture Notes". North Carolina State University. 1997.
- [45] Krishnamurthy, K., Vetury, R., Yet-zen Liu, Rodwell, M.J.W., Pallela, R. "40 Gbit/s Optical Receiver Module with High Conversion Gain and Sensitivity". Electronics Letters, Vol. 39, Issue 24. pp. 1738-1739. Nov, 2003.
- [46] Kudo, K., Yashiki, K., Yamaguchi, M. "1.55 Micrometer Wavelength-selectable Microarray DFB-LD's with Monolithically Integrated MMI Combiner, SOA, and EA-modulator". IEEE Photonics Technology Letters, Vol. 12, pp. 242-244. Mar, 2000.
- [47] Kuebart, W., Reemtsma, J.-H., Kaiser, D., Grosskopf, H., Besca, F., Luz, G., Korber, W., Gyuro, I. "High Sensitivity InP-based Monolithically Integrated pin-HEMT Receiver-OEIC's for 10 Gb/s". IEEE Transactions on Microwave Theory and Techniques, Vol. 43, Issue 9. pp. 2334-2341. Sept, 1995.
- [48] Lee, G.-H., Jiang, Z., Xiao, S., Weiner, A.M. "1700 ps/nm Tunable Dispersion Compensation for 10 Gbit/s RZ Lightwave Transmission". Electronics Letters, Vol. 42, Issue 13. pp. 768-769. June, 2006.
- [49] Liu, X, Gnauck, A. H., Wei, X., Hsieh, J.C., Ai, C., Chien, V. "Athermal Optical Demodulator for OC-768 DPSK and RZ-DPSK Signals". IEEE Photonics Technology Letters, Vol. 17, No. 12. pp. 2610-2612. Dec, 2005.

- [50] Long, S. I. "Basics of GaAs, InP, and SiGe RFICs RFIC Design Examples." 2001 IEEE GaAs IC Symposium. University of California, Santa Barbara, CA 93106. 2001.
- [51] Lunardi, L.M., Chandrasekhar, S., Gnauck, A.H., Burrus, C.A., Hamm, R.A., Sulhoff, J.W., Zyskind, J.L. "A 12-Gb/s High-performance, High-sensitivity Monolithic PIN/HBT Photoreceiver Module for Long-wavelength Transmission Systems". IEEE Photonics Technology Letters, Vol. 7, Issue 2. pp. 182-184. Feb, 1995.
- [52] Lunardi, L.M., Chandrasekhar, S., Gnauck, A.H., Burrus, C.A. "20-Gb/s Monolithic p-i-n/HBT Photoreceiver Module for 1.55- μ m Applications". IEEE Photonics Technology Letters, Vol. 7, Issue 10. pp. 1201-1203. Oct, 1995.
- [53] Madsen, C.K., Lenz, G., Bruce, A.J., Cappuzzo, M.A., Gomez, L.T., Scotti, R.E. "Integrated All-pass Filters for Tunable Dispersion and Dispersion Slope Compensation". IEEE Photonics Technology Letters, Vol. 11, Issue 12. pp. 1623-1625. Dec, 1999.
- [54] Madureira, M.A.M., Monteiro, P.M.P., Aguiar, R.L., Violas, M., Gloanec, M., Leclerc, E., Lefebvre, B., "Broad-band Optical Receiver for Multigigabit-per-second (40Gb/s) Optical Communication Systems. The 10th IEEE International Symposium on Electron Devices for Microwave and Optoelectronic Applications, 2002. pp. 271-276. Nov, 2002.
- [55] Madureira, M.A.M., Monteiro, P.M.P., Aguiar, R.L., Violas, M., Gloanec, M., Leclerc, E., Lefebvre, B. "High Gain GaAs 10Gbps Transimpedance Amplifier with Integrated Bondwire Effects". Proceedings of the 2003 International Circuits and Systems, 2003. Volume 2. pp. 173-176. May, 2003.
- [56] Marincic, A., Acimovic-Raspopovic, V. "Evolution of WDM optical networks". 2001 5th International Conference on Telecommunications in Modern Satellite, Cable and Broadcasting Service, Vol. 2. pp. 473-480. Sept, 2001.
- [57] Marom, D.M., Doerr, C.R., Cappuzzo, M.A., Evans Yifan Chen, Wong-Foy, A., Gomez, L.T., Chandrasekhar, S. "Compact Colorless Tunable Dispersion Compensator with 1000-ps/nm Tuning Range for 40-gb/s Data Rates". Journal of Lightwave Technology, Vol. 24, Issue 1. pp. 237-241. Jan, 2006.
- [58] Matsuda, H.; Miura, A.; Okamura, Y.; Irie, H.; Ito, K.; Toyonaka, T.; Takahashi, H.; Harada, T. "High Performance of 10-Gb/s APD/Preamplifier Optical-receiver Module with Compact Size". IEEE Photonics Technology Letters, Vol. 15, Issue 2. pp. 278-280. Feb, 2003.
- [59] Matsuoka, Y., Yamahata, S., Kurishima, K., Ito, H. "Ultrahigh-Speed InP/InGaAs Double-Heterostructure Bipolar Transistors and Analyses of Their Operation". Japan Applied Physics, Vol. 35, Part 1, No. 11. pp. 5646-5654. Nov, 1996.

- [60] Min, B., Yoon, H., Lee, W. J., Park, N. "Coupled Structure for Wide-band EDFA with Gain and Noise Figure Improvements from C to L-band ASE Injection". IEEE Photonics Technology Letters, Vol. 12, Issue 5. pp. 480-482. May, 2000.
- [61] Moribayashi, S., Ohhira, R., Oami, T., Noda, A., Baba, N., Takeuchi, T. "40-Gb/s Optical Receiver Achieving 13 dB Dynamic Range Without Optical Pre-amplifier". 2003 Optical Fiber Communications Conference, Vol. 1. pp. 110-111. March, 2003.
- [62] Moss, D., Lunardi, L., Lamont, M., Randall, G., Colbourne, P., Chandrasekhar, S., Buhl, L. "Tunable Dispersion Compensation at 10 Gb/s and 40 Gb/s using Multicavity All-pass Etalons". Optical Fiber Communications Conference, 2003, Vol. 1. pp. 162-163. March, 2003.
- [63] Nakata, T., Shiba, K., Takeuchi, T., Sasaki, T., Makita, K. "10 Gbit/s Asymmetric Waveguide APD with High Sensitivity of -30dBm". IEEE Electronics Letters, Vol. 42, Issue 20. pp. 1177-1178. Sept, 2006.
- [64] Noda, Y., Suzuki, M., Kushiroya, Y., Akiba, S. "High-speed Electroabsorption Modulator with Strip-Loaded GaInAsP Planar Waveguide". Journal of Lightwave Technology, Vol. 4, Issue 10. pp 1445-1453. Oct, 1986.
- [65] Ohashi, M., Shiraki, K., Tajima, K., "Optical Loss Property of Silica-Based Single-Mode Fibers" Journal of Lightwave Technology, Vol. 10, Issue 5. pp. 539-543. May, 1992.
- [66] Oohashi, H., Mawatari, H., Ichikawa, F., Kasaya, K., Ishii, H., Tohmori, Y. "Highly Reliable L-band Tunable DFB Laser Array". 31st European Conference on Optical Communication, 2005, Vol. 4. pp. 893-894. Sept, 2005.
- [67] Park, E.D., Croeze, T. J., Delfyett, Jr., P. J., Braun, A., Abeles, J. "Closed Loop Spectral Control of Multiwavelength 1550 Laser". Electronics Letters, Vol. 38, No. 7, pp. 26-28. Jan, 2002.
- [68] Petruzzi, P., Lowry, C., Sivanesan, P. "Dispersion Compensation Using Only Fiber Bragg Gratings". IEEE Journal of Selected Topics in Quantum Electronics, Vol. 5, Issue 5. pp. 1339-1344. Sept, 1999.
- [69] Pizzinat, A., Schiffrini, A., Alberti, F., Paoletti, A., Caccioli, D., Griggio, P., Minzioni, P., Matera, F. "Numerical and Experimental Comparison of Dispersion Compensation Techniques on Different Fibers". IEEE Photonics Technology Letters, Vol. 14, Issue 10. pp. 1415-1417. Oct, 2002.
- [70] Poturaj, K., Wojcik, J., Janoszczuk, B., Mergo, P., Makara, M., Spytek, W., Kowalski, A., Abramski, K.M., Pawlik, E.M. "Erbium Doped Fiber for L-band EDFA". 2000 2nd International Conference on Transparent Optical Networks. Pp 155-158. June, 2000.
- [71] Pozar, D. M. "Microwave Engineering". Third Edition. John Wiley & Sons, Inc. 2005.

- [72] Ramaswami, R., Sivarajan, K.N. "Optical Networks: A Practical Perspective". Second Edition. Academic Press. 2002.
- [73] Rasmussen, J.C. "PMD and Chromatic Dispersion Compensation for 40 Gbit/s Optical Networks". 2005 18th Annual Meeting of the IEEE Lasers and Electro-Optics Society. pp. 704 – 705. Oct, 2005.
- [74] Rochette, M., Guy, M., LaRochelle, S., Lauzon, J., Trepanier, F. "Gain Equalization of EDFA's with Bragg Gratings". IEEE Photonics Technology Letters, Vol. 11, Issue 5. pp. 536-538. May, 1999.
- [75] Saleh, B. E. A., Teich, M. C. "Fundamentals of Photonics". Wiley and Sons. 1991.
- [76] Schramm, C., Bach, H.-G., Beling, A., Jacumeit, G., Ferber, S., Ludwig, R., Ziegler, R., Mekonnen, G.G., Kunkel, R., Schmidt, D., Schlaak, W., Unterborsch, G. "High-bandwidth Balanced Photoreceiver Suitable for 40-gb/s RZ-DPSK Modulation Formats". IEEE Journal of Selected Topics in Quantum Electronics, Vol. 11, Issue 1. pp. 127-134. Feb, 2005.
- [77] Shimizu, N., Murata, K., Hirano, A., Miyamoto, Y., Kitabayashi, H., Umeda, Y., Akeyoshi, T., Furuta, T., Watanabe, N. "40 Gbit/s Monolithic Digital OEIC Composed of Unitravelling-carrier Photodiode and InP HEMTs". IEEE Electronics Letters, Vol. 36, Issue 14. pp. 1220-1221. July, 2000.
- [78] Shiu, K.-T., Agashe, S.S., Forrest, S.R. "A Simple Monolithically Integrated Optical Receiver Consisting of an Optical Pre-amplifier and a PIN Photodiode". IEEE Photonics Technology Letters, Vol. 18, Issue 8. pp. 956-958. April, 2006.
- [79] Sieniawski, D. "Low Cost 10 Gb/s Receiver Module". 1998 48th IEEE Electronic Components and Technology Conference. pp. 181-183. May, 1998.
- [80] Sinsky, J.H., Adamecki, A., Burrus, C.A., Chandrasekhar, S., Leuthold, J., Wohlgenuth, O. "A 40-Gb/s Integrated Balanced Optical Front End and RZ-DPSK Performance". IEEE Photonics Technology Letters, Vol. 15, Issue 8. pp. 1135-1137. Aug, 2003.
- [81] Sinsky, J., Adamecki, A., Gnauck, A., Burrus, C.A., Jr., Leuthold, J., Wohlgenuth, O., Chandrasekhar, S., Umbach, A. "RZ-DPSK Transmission Using a 42.7-Gb/s Integrated Balanced Optical Front End with Record Sensitivity". Journal of Lightwave Technology, Vol. 22, Issue 1. pp. 180-185. Jan, 2004.
- [82] Suhyun Kim, Youngchul Chung; Su Hwan Oh, Moon-Ho Park. "Design and Analysis of Widely Tunable Sampled Grating DFB Laser Diode Integrated with Sampled Grating Distributed Bragg Reflector". IEEE Photonics Technology Letters, Vol. 16, Issue 1. pp 15-17. Jan, 2004.

- [83] Suzuki, Y., Shimawaki, H., Amamiya, Y., Fukuchi, K., Nagano, N., Yano, H., Honjo, K. "An HBT Preamplifier for 40-Gb/s Optical Transmission Systems". 1996 18th Annual Gallium Arsenide Integrated Circuit (GaAs IC) Symposium. pp. 203-206. Nov, 1996.
- [84] Takahata, K., Muramoto, Y., Akatsu, Y., Akahori, Y., Kozen, A., Itaya, Y. "10-Gb/s Two-channel Monolithic Photoreceiver Array Using Waveguide p-i-n PD's and HEMTs". IEEE Photonics Technology Letters, Vol. 8, Issue 4. pp. 563-565. April, 1996.
- [85] Takahata, K., Muramoto, Y., Fukano, H., Kato, K., Kozen, A., Kimura, S., Imai, Y., Miyamoto, Y., Nakajima, O., Matsuoka, Y. "Ultrafast Monolithic Receiver OEIC Composed of Multimode Waveguide p-i-n Photodiode and HEMT Distributed Amplifier". IEEE Journal of Selected Topics in Quantum Electronics, Vol. 6, Issue 1. pp. 31-37. Feb, 2000.
- [86] Takeuchi, H., Wakamiya, M., "Ultra-fast Electroabsorption Modulator Integrated DFB Lasers". Indium Phosphide and Related Materials. pp. 428 – 431. May 2001.
- [87] Uh-Chan Ryu, Oh, K., Shin, W., Paek, U.C. "Inherent Enhancement of Gain Flatness and Achievement of Broad Gain Bandwidth in Erbium-doped Silica Fiber Amplifiers". IEEE Journal of Quantum Electronics, Vol. 38, Issue 2. pp. 149-161. Feb, 2002.
- [88] Unterborsch, G., Umbach, A., Trommer, D., Mekonnen, G.G. "70 GHz Long-Wavelength Photodetector". 11th International Conference on Integrated Optics and Optical Fibre Communications, Volume 2. pp 25-38. Sept, 1997.
- [89] Wang, G., Yoneda, Y., Hanawa, I., Aono, H., Araki, K., Takechi, M., Momma, Y., Odagawa, T., Fujii, T., Sato, K., Kobayashi, M. "Highly Reliable High Performance Waveguide-integrated InP/InGaAs PIN Photodiodes for 40 Gbit/s Fibre-optical Communication Application". Electronics Letters, Vol. 39, Issue 15. pp. 1147-1149. July, 2003.
- [90] Weber, C., Fischer, J.K., Bunge, C.-A., Petermann, K. "Electronic Precompensation of Intrachannel Nonlinearities at 40 gb/s". IEEE Photonics Technology Letters, Vol. 18, Issue 16. pp. 1759-1761. Aug, 2006.
- [91] Weiner, J.S., Leven, A., Houtsma, V., Baeyens, Y., Young-Kai Chen, Paschke, P., Yang Yang, Frackoviak, J., Wei-Jer Sung, Tate, A., Reyes, R., Kopf, R.F., Weimann, N.G. "SiGe Differential Transimpedance Amplifier with 50-GHz Bandwidth". IEEE Journal of Solid State Circuits, Vol. 38, Issue 9. pp. 1512-1517. Sept, 2003.
- [92] Weiner, J.S., Lee, J.S., Leven, A., Baeyens, Y., Houtsma, V., Georgiou, G., Yang Yang, Frackoviak, J., Tate, A., Reyes, R., Kopf, R.F., Wei-Jer Sung, Weimann, N.G., Young-Kai Chen. "An InGaAs-InP HBT Differential Transimpedance Amplifier with 47-GHz Bandwidth". IEEE Journal of Solid-State Circuits, Vol. 39, Issue 10. pp. 1720-1723. Oct, 2004.

- [93] Winzer, P., Essiambre, R.-J. "Advanced Optical Modulation Formats". Proceedings of the IEEE, Vol. 94, No. 5. pp. 952-985. May, 2006.
- [94] Wooten, E. L., Kissa, K. M., Yi-Yan, A., Murphy, E. J., Lafaw, D. A., Hallemeier, P. F., Maack, D., Attanasio, D. V., Fritz, D. J., McBrien, G. J., Bossi, D. E. "A Review of Lithium Niobate Modulators for Fiber-Optic Communication Systems". IEEE Journal of Selected Topics in Quantum Electronics, Vol. 6, No. 1. pp. 69-82. Jan, 2000.
- [95] Wu, C.Q., Sovero, E.A., Massey, B. "40-GHz Transimpedance Amplifier with Differential Outputs Using InP-InGaAs Heterojunction Bipolar Transistors". IEEE Journal of Solid State Circuits, Vol. 38, Issue 9. pp. 1518-1523. Sept, 2003.
- [96] Xu, C., Xiang Liu, Xing Wei "Differential Phase-shift Keying for High Spectral Efficiency Optical Transmissions". IEEE Journal of Selected Topics in Quantum Electronics, Vol. 10, Issue 2. pp. 281-293. March, 2004.
- [97] Yamanaka, T., Tsuzuki, K., Kikuchi, N., Yamada, E., Shibata, Y., Fukano, H., Nakajima, H., Akage, Y., Yasaka, H. "High-performance InP-based Optical Modulators". 2006 Optical Fiber Communication Conference and the 2006 National Fiber Optic Engineers Conference. March 2006.
- [98] Yamashita, K., Oikawa, Y., Yamamoto, T., Ohnishi, H., Mikawa, T., Hamano, H. "High-performance 10 Gb/s Optical Receiver Using Avalanche Photodiode and Heterojunction Bipolar Transistor ICs". Optical Fiber Communication Conference. pp. 16-17. 1997.
- [99] Yamashita, S., Nishihara, M. "L-band Erbium-doped Fiber Amplifier Incorporating an Inline Fiber Grating Laser" IEEE Journal of Selected Topics in Quantum Electronics, Vol. 7, Issue 1. pp. 44-48. Jan, 2001.
- [100] Yun, T.Y., Han, J.H., Park, M.S. "10 Gbit/s Optical Receiver of Lossless Tuned PIN-HEMT with High Performance". Electronics Letters, Vol. 31, Issue 19. pp. 1688-1689. Sept, 1995.
- [101] Zhihong Li, Chao Lu, Yixin Wang. "Performance Improvement for Constant Amplitude NRZ-DPSK Transmission Through Modulation-pulse-pre-shaping." Optical Fiber Communication Conference, 2005, Vol. 1. pp. 154-156. March, 2005.
- [102] Zou, X.Y., Hayee, M.I., Hwang, S.-M., Willner, A.E. "Limitations in 10 Gb/s WDM Optical-fiber Transmission when Using a Variety of Fiber Types to Manage Dispersion and Nonlinearities". Journal of Lightwave Technology, Vol. 14, Issue 6. pp. 1144-1152. June, 1996.
- [103] http://www.mrfiber.com/Wideband_EDFA.htm

[104] <http://www.lucent.com/products/solution/0,,CTID+2021-STID+10482-SOID+1577-LOCL+1,00.html>

[105]

http://www.usa.siemens.com/index.jsp?sdc_rh=null&sdc_flags=null&sdc_sectionid=0&sdc_secnavid=0&sdc_3dnvlstid=&sdc_countryid=194&sdc_mpid=0&sdc_unitid=999&sdc_conttpe=2&sdc_contentid=1220522&sdc_langid=1&sdc_pnid=&

[106] <http://www.nortelnetworks.com/products/library/collateral/56088.16-11-98.pdf>

[107] <http://www.discoverysemiconductors.com>

[108] <http://hbt.ucsd.edu>

[109] <https://edasupportweb.soco.agilent.com/docs/adsd2005A/manuals/cktcomp.html>
(Nonlinear Devices -- Agilent HBT Model)

[110] <http://www.sei.co.jp/optproducts/basic/02.html>

[111] <http://www.ofsoptics.com/labs/history.php>

[112] http://searchnetworking.techtarget.com/sDefinition/0%2C%2Csid7_gci213892%2C00.html

APPENDIX

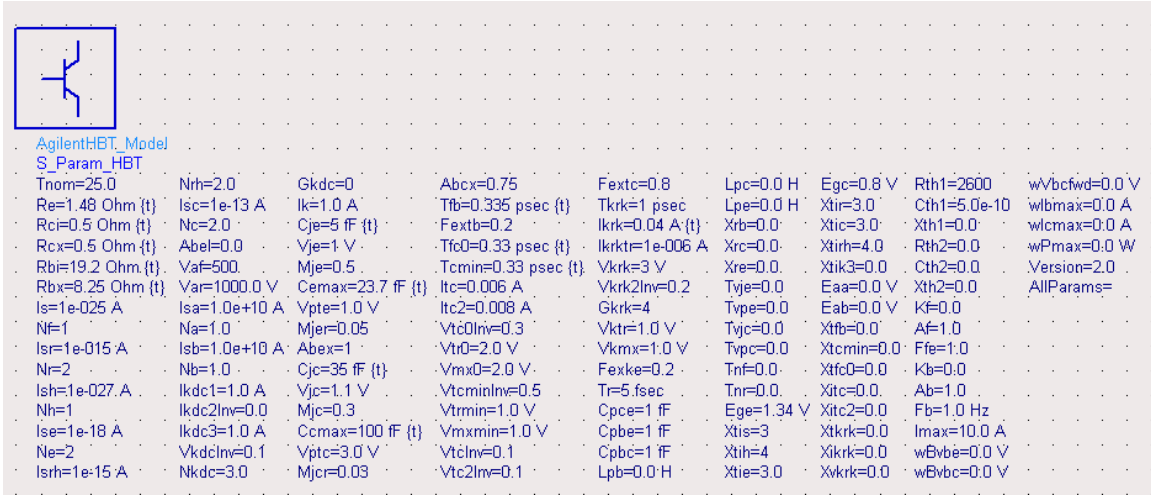


Figure A.1: Adjusted DHBT model